ENRICHMENT OF THE INTERGALACTIC MEDIUM

ENRICHMENT OF THE INTERGALACTIC MEDIUM

By
SIJING SHEN, M.SC

A Thesis
Submitted in Partial Fulfillment
of the Requirements
for the Degree of

Doctor of Philosophy

September 2010

McMaster University

DOCTOR OF PHILOSOPHY (2010) McMaster University
(Physics and Astronomy) Hamilton, Ontario

TITLE: Enrichment of The Intergalactic Medium
AUTHOR: Sijing Shen, M.Sc. (McMaster University)
SUPERVISOR: Professor James Wadsley
NUMBER OF PAGES: XIII, 169

Abstract

A study of metal enrichment of the intergalactic medium (IGM) using a series of smooth particle hydrodynamics (SPH) simulations is presented, employing models for metal cooling and the turbulent diffusion of metals and thermal energy. An adiabatic feedback mechanism was adopted where gas cooling was prevented on the timescale of supernova bubble expansion to generate galactic winds without explicit wind particles. The simulations produced a cosmic star formation history (SFH) that is broadly consistent with observations until z $\sim$ 0.5, and a steady universal neutral hydrogen fraction ($\Omega_{\rm HI}$) that compares reasonably well with observations. The evolution of the mass and metallicities in stars and various gas phases was investigated. At z=0, about 40% of the baryons are in the warm-hot intergalactic medium (WHIM), but most metals (80%-90%) are locked in stars. At higher redshifts the proportion of metals in the IGM is higher due to more efficient loss from galaxies. The results also indicate that IGM metals primarily reside in the WHIM throughout cosmic history, which differs from simulations with hydrodynamically decoupled explicit winds. The metallicity of the WHIM lies between 0.01 and 0.1 solar with a slight decrease at lower redshifts. The metallicity evolution of the gas inside galaxies is broadly consistent with observations, but the diffuse IGM is under-enriched at z $\sim$ 2.5. Metals enhance cooling which allows WHIM gas to cool onto galaxies and increases star formation. Metal diffusion allows winds to mix prior to escape, decreasing the IGM metal content in favour of gas within galactic halos and star forming gas. Diffusion significantly increases the amount of gas with low metallicities and improves the density-metallicity relation.

The galactic wind generation mechanism and the wind properties from our simulations were investigated. It was found that: 1. Galactic winds are most efficient for halos in the intermediate mass range $10^{10}M_\odot$ - 10^{11} $M_\odot$.

These winds dominate the metal ejection at all redshifts, although towards lower redshift the contributions from larger halos become relatively more important. At the low mass end gas is prevented from accreting onto halos and has very low metallicities. At the high mass end, the fraction of halo baryons escaped as winds declines along with the decline of stellar mass fraction in these halos. The decrease in wind ejection is likely because of the decreases in star formation activity, wind mass loading and wind escape efficiency as the halo mass increases. 2. The adiabatic feedback can generate winds with mass loading factors comparable to the ones used in explicit superwind models. The mass loading factor decreases towards lower redshift, implying that smaller halos have larger mass loading. 3. Metals located at lower density were generated at earlier epochs from small halos, suggesting that the wind traveling speed can affect the metal distribution in the IGM.

Acknowledgments

I would especially like to thank my supervisor, Dr. James Wadsley for his guidance, patience and all the insightful advice and discussions which have helped me at every stage of my research and thesis writing. Without him the accomplishment of this work would not have been possible. I would also like to thank my supervisory committee members, Dr. Hugh Couchman and Dr. Laura Parker for their helpful comments and suggestions. I am grateful to my collaborators and colleagues Dr. Greg Stinson, Dr. Sergey Mashchenko and Dr. Jeremy Bailin for all the fruitful discussions during the group meetings, and for their help in various ways during my research.

I owe my deepest gratitude to my husband and best friend, Dr. Nicolas Petitclerc, for his love, friendship and enormous support in both work and life, especially at the last stage of my thesis writing. A heartfelt thanks my parents, Minghua Shen and Minghua Yu, for their love and steadfast encouragement despite the distance. I would also like to thank the following friends who have made my life as a graduate student full of joy and memories, Dr. Kristin Woodley, Dr. Pamela Klaassen, Dr. Marie-Josée Colbert, Dr. Charles-Philippe Lajoie, Rachel Anderson, Dr. Brad Warren, Kiri Nichol, Robert Cockcroft, Patrick Rogers, Liqun Qiu and Sarah Nickerson.

I am grateful to the Natural Sciences and Engineering Research Council of Canada (NSERC) for the Alexander Graham Bell Canada Graduate Scholarship. I would also like to thank the Shared Hierarchical Academic Research Computing Network (SHARCnet) for granting me dedicated computing resources for my simulations.

Table of Contents

List of Figures

List of Tables

Glossary of Acronyms

AGN	Active Galactic Nuclei
CDM	Cold Dark Matter
CIE	Collisional Ionization Equilibrium
CMB	Cosmic Microwave Background
CR	Cosmic Ray
DLA	Damped Lyman-Alpha System
EOS	Equation of State
FFT	Fast Fourier Transform
FOF	Friends-of-Friends
ICM	Intracluster Medium
IGM	Intergalactic Medium
IMF	Initial Mass Function
ISM	Interstellar Medium
ΛCDM	Lambda Cold Dark Matter
PDF	Probability Density Function
QSO	Quasi-Stellar Object
SF	Star Formation
SFH	Star Formation History
SFR	Star Formation Rate
SN	Supernova
SN II	Type II Supernova
SN Ia	Type Ia Supernova
SPH	Smoothed Particle Hydrodynamics
WHIM	Warm-Hot Intergalactic Medium
UV	Ultraviolet

Chapter 1

Introduction

1.1 Large-scale Structure and Galaxy Formation in the ΛCDM Cosmology

One of the outstanding questions in contemporary cosmology is how our Universe, being largely homogeneous after the Big Bang, evolves to the inhomogeneous structure we observe today. There are galaxies and galaxy clusters – large, bound objects with dark matter, gas and sometimes stars (some galaxies does not have stars) arranged in complex structures. Galaxies have various types with different mass, luminosity, morphology and stellar contents (cf. Binney & Merrifield, 1998), but on large scales they are distributed in a correlated way (Stoughton et al., 2002) with "walls" and "voids" which form a "cosmic web". Between galaxies there is gaseous material which is typically not luminous and has low density. This is the intergalactic medium (IGM). The discovery and detection of the IGM have been mainly through absorption features (mostly the 121.6 nm Lyman α transition from neutral hydrogen) in background quasistellar object (QSO) spectra (Rauch, 1998, and references therein).

The most successful paradigm to explain the large-scale structure seen today is hierarchical structure formation in Λ Cold Dark Matter (ΛCDM) cosmology (White & Rees, 1978; Komatsu et al., 2009). In this picture, the Universe is flat and expanding according to Friedman's Equation (Peebles, 1993). The dynamics of expansion is determined by the mass density of dark energy Ω_Λ, matter Ω_m (including normal baryonic matter and dark matter) and radiation Ω_{rad}. Radiation decays rapidly with the expansion of the universe, $\Omega_{rad} \propto (1+z)^4$, where z is the redshift, and becomes a minor component at redshift $z \sim 3000$. Matter density decays with expansion as $\Omega_m \propto (1+z)^3$, and dark energy is a constant therefore becomes increasingly dominant as the Universe expands. The Universe today consists of $\sim 70\%$ dark energy, $\sim 25\%$ dark matter and only about 5% baryonic matter. Although the nature and origins of dark energy and dark matter are unknown, their mass contents can be accurately measured from the fluctuations in the Cosmic Microwave Background (CMB) – the information from the last scattering at recombination (z$\approx$ 1089). Cold dark matter refers to non-relativistic, collisionless particles that were decoupled early in the Universe and do not strongly interact with baryonic matter except gravitationally.

On the largest scales, the Universe is homogeneous and isotropic. This is an assumption of the Freidman model and also supported by the black-body spectrum of the CMB radiation. However, fluctuations are observed at smaller scales (e.g., $\delta T/T \sim 10^{-5}$ in the CMB) and these are the seeds of structures we see today. The power spectrum of the density fluctuations ($\delta = \delta\rho / < \rho >$

where $< \rho >$ is the mean density) can be calculated from observations of the anisotropies in the CMB and compared to theory (e.g., CMBFAST from Seljak & Zaldarriaga, 1996). The density fluctuations grow under gravity. The growth in density is initially linear, but beyond $\delta \sim 1$, it enters a non-linear regime and eventually results in collapse of dark matter into sheets and filamentary structures, and dark matter halos form at the intersection of these structures. In a CDM scenario, small scale perturbations in the primordial fluctuation spectrum have the largest amplitudes, thus structure formation starts from the formation of small proto-galaxies. These progenitors cluster and form bigger halos through mergers in an hierarchical process leading to larger objects. This is the so called hierarchical or bottom-up picture of structure formation (Peacock, 1999). Dark matter halos provide gravitational potential wells for gas, which will then accrete onto halos and potentially form stars.

Because dark matter dominates the matter budget and it only interacts through gravity, the formation of large scale structure and dark matter halos is relatively well understood, especially with the development of N-body simulations (e.g., Springel et al., 2005). However, this is not the case for baryonic matter, particularly at galactic scales. How gas accretes onto galaxy halos, how stars form within galactic disks, how feedback from stellar radiation, supernova explosions and active galactic nuclei (AGN) affects the formation and evolution of galaxies, how metals (elements that have atomic number larger than helium) enter the intergalactic/intracluster gas through feedback, remain as some of the big questions in understanding galaxy formation. The main difficulties toward a complete understanding are two-fold. First of all, the physical processes of star formation, supernova explosions, AGN and other forms of feedback are not fully understood; second, the range of spatial (and density) scales involved, from large-scale structure (Mpc) to star formation (pc), is so large that it is impossible to model it in a single simulation with current computing power. Thus various models have been developed to provide simple "recipes" to model the processes listed above (e.g., Navarro & White, 1993; Katz et al., 1996; Thacker & Couchman, 2000; Springel & Hernquist, 2003; Oppenheimer & Davé, 2006; Stinson et al., 2006; Dalla Vecchia & Schaye, 2008). It has been increasingly realized, through recent simulations and observations, that galaxies and their environment, the intergalactic medium, are closely related to each other and need to be studied together (Putman et al., 2009; Steidel et al., 2010). The enrichment of the IGM, i.e., how metals produced deep inside galaxies reach the far-away intergalactic medium, is an observable probe of the interaction between galaxies and the IGM. Therefore the study of enrichment is not only a interesting topic itself, but also helps to improve our understanding of the "gastrophysics" in galaxy formation.

1.2 The Intergalactic Medium and Its Metal Enrichment

The intergalactic medium (IGM) refers to the gaseous medium surrounding and between galaxies. It contains most of the baryons in the Universe and provides the fuel for galaxies to form stars in which metals are produced. In turn, supernovae and AGN feedback generate galactic winds which enrich the IGM with metals, while stars and active galactic nuclei (AGN) emit UV photons to ionize the IGM. This interplay between the IGM and galaxies, mediated by metal cooling in the presence of UV, regulates the formation of stars in the universe. The evolution and enrichment history of the IGM provides a record of this interplay.

Because it is not luminous, the discovery of the IGM was mainly through the Lyman α forest – the numerous absorption lines in QSO spectra produced by the Lyman α transition of neutral hydrogen in the IGM (Rauch, 1998, and references therein). The comparison between artificial spectra generated in hydrodynamical cosmological simulations and observed ones (Cen et al., 1994; Zhang et al., 1995; Hernquist et al., 1996; Wadsley & Bond, 1997) plays a important role in understanding the intergalactic nature of the Lyα forest. Spectral analysis provides information on the abundances of the absorbers at different column densities and the line width distribution (if not saturated). From these we can derive element abundances, the spatial distribution and temperature of the gas, and information about the radiation background. Besides hydrogen lines, observations also detect absorption lines due to metal ions (e.g., C III , C IV, Si III, S IV and O VI) in QSO spectra, which show that the intergalactic medium (IGM) far outside large galaxies ($\rho/\rho_{mean} < 10$) is enriched (e.g. Sargent et al., 1988; Songaila & Cowie, 1996; Davé et al., 1998; Ellison et al., 2000; Schaye et al., 2000; Pettini et al., 2003; Schaye et al., 2003; Aguirre et al., 2004; Simcoe et al., 2004). Figure 1.1 shows an example spectrum of the C IV ($\lambda\lambda1548, 1551$) doublet absorption lines (Sargent et al., 1988). There is evidence for enrichment extending back to $z > 5$ (Pettini et al., 2003; Simcoe, 2006; Ryan-Weber et al., 2006) and the carbon abundance [C/H] does not evolve much from z$\sim$5 to z$\sim$2 (Schaye et al., 2003; Songaila, 2005; Ryan-Weber et al., 2006).

The non-evolution of carbon abundance (derived from C IV) triggered a

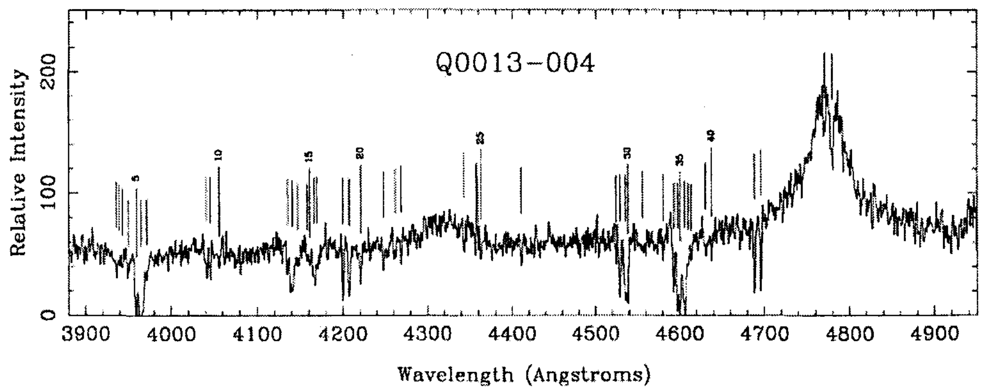

Figure 1.1 An example of QSO spectra with absorptions from the C IV ($\lambda\lambda 1548, 1551$) doublet, indicated by the numbers on the spectra. Figure adapted from Sargent et al. (1988).

debate on when the enrichment happens and from what type of galaxies metals are ejected. One opinion is that metallicity [Z/H] does not evolve with redshift, thus metals were sprinkled at $z \gtrsim 5$ by dwarf progenitor galaxies when the gravitational potential of these objects is shallower (Scannapieco et al., 2002; Porciani & Madau, 2005). On the other hand, observations of metal absorbers at lower redshift ($z < 3$)(e.g., Adelberger et al., 2005; Pieri et al., 2006) found there is a correlation between metal absorption and galaxies, indicating metal enrichment is still ongoing by feedback processes in galaxies. Oppenheimer & Davé (2006) and Aguirre & Schaye (2007) argue that the non-evolution of [C/H] can be caused by the decreasing ionization fractions of C IV towards lower redshift because the IGM increases its temperature as larger structures form, i.e. C IV cannot probe hot gas far above 10^5 K. Although not directly testing the early enrichment picture, Aguirre et al. (2005); Oppenheimer & Davé (2006); Wiersma et al. (2009) found that the observed metal enrichment can be reasonably reproduced by galactic wind throughout cosmic history. While final agreement has not been reached, the debate does emphasize that to understand the observed metal spectra, many factors such as the shape of the radiation background, the gas temperature and even the turbulent motion of gas (Oppenheimer & Davé, 2009) need to be considered. Nevertheless, a general consensus has been reached that galactic winds, although the launch mechanism is not fully understood, are the primary mechanism for distributing metals in the IGM.

Galactic winds are observed in nearby star forming galaxies such as M82 (e.g., Lynds & Sandage, 1963) (Figure 1.2) and galaxies that host AGN such as NGC 1068 (e.g., Cecil et al., 1990). Recently, observations of high redshift galaxies (e.g., Pettini et al., 2000, 2001, 2002; Adelberger et al., 2003; Swinbank et al., 2005; Steidel et al., 2010) found that at $z > 2$, almost all galaxies drive winds, especially Lyman Break Galaxies (LBGs). Galactic winds have complex structures, so a multi-wavelength approach (from radio to X-ray) is necessary. It is found that winds are extremely multiphase, consisting of hot wind fluids ($> 10^5$K, detectable by X-ray emission or coronal gas absorption such as O VI), a warm ionized phase ($10^4 - 10^5$K), cool, neutral gas and even molecular, star forming gas (Veilleux et al., 2005). The neutral and molecular gas is considered to be ISM that is entrained in the hot wind fluid. The kinematics of winds vary with phase temperature. Cool, neutral outflows generally have observed velocities of several hundred km/s (Walter et al., 2002), but the velocity of hot wind fluid could reach about 1000 km/s to several thousands km/s (Heckman et al., 2000; Strickland et al., 2004). Correlations have been observed between galactic winds and the star formation rates (SFR) in galaxies. The ratio between the mass loss in winds and the SFR (the mass loading factor) $\eta \equiv \dot{M}_w/\dot{M}_\star$ (where $\dot{M}_w$ is the mass loss in winds and $\dot{M}_\star$ is the SFR) ranges from 0.01 - 10 (Veilleux et al., 2005) but large uncertainties exist in this estimate

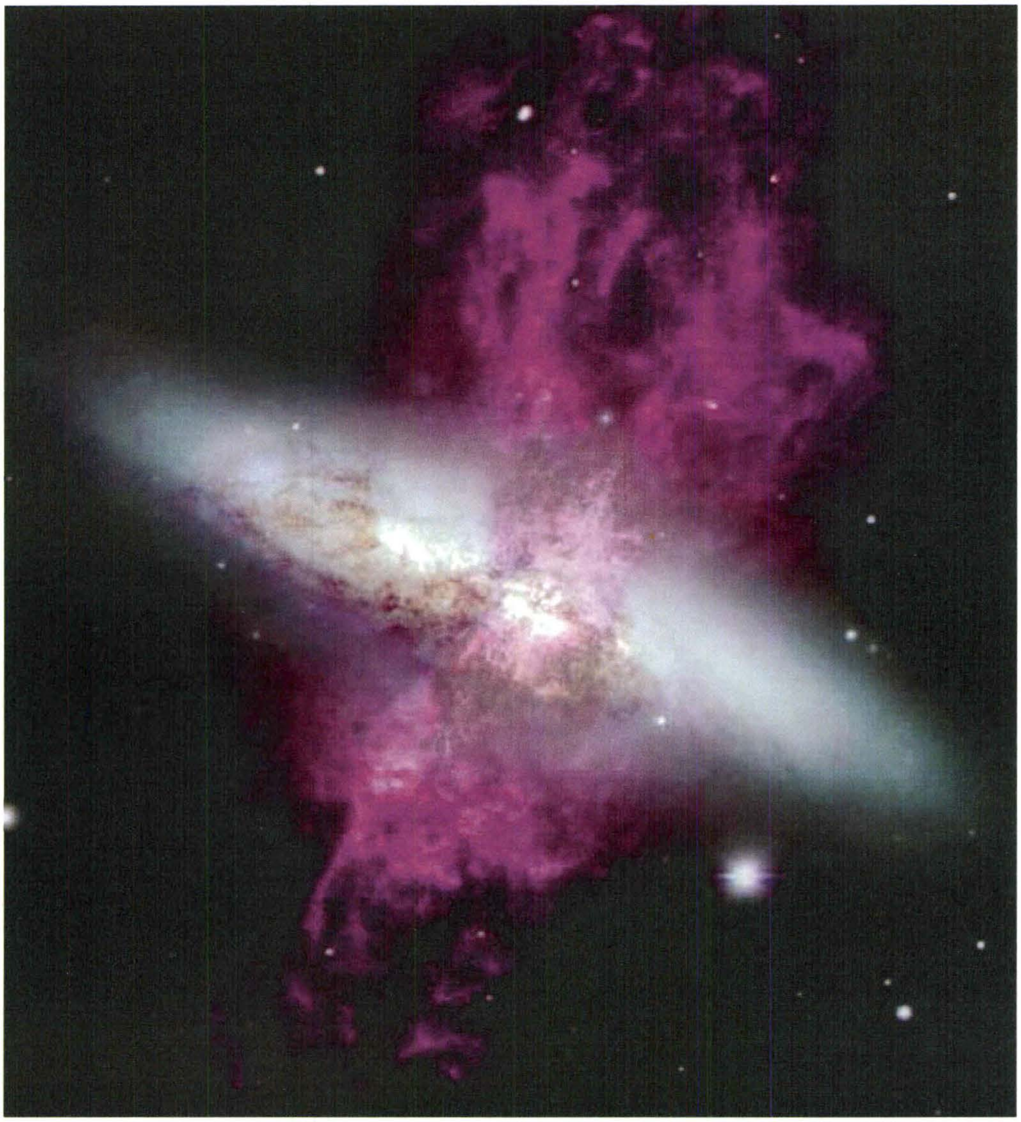

Figure 1.2 Biconical galactic winds detected in star forming galaxy M82, using Hα emission (magenta). The Hα image is superimposed on an optical HST image of M82. Image adapted from Veilleux et al. (2005) (courtesy Smith, Gallagher and Westmoquette).

due to uncertainties in measuring the mass of outflows.

Two mechanisms have been proposed for the launch of galactic winds. In the first mechanism, galactic-scale winds are launched as the ejecta of a large number of co-existing supernova (SN) explosions (Heckman et al., 1990). The overlap of many SN bubbles creates a "superbubble" that can push out of the ISM, entrain cool neutral gas and eventually escape the galaxy (Aguirre et al., 2001; Theuns et al., 2001). In this case the wind is "energy driven". In the second mechanism galactic winds can be driven by the momentum deposited by radiation pressure from starbursts or AGN (Murray et al., 2005). In this case, the wind is "momentum driven". Because momentum is deposited into the star forming gas directly, the winds in this scenario are cooler initially. In both cases, the velocity of wind $v_w \sim \sigma$, where σ is the velocity dispersion of the galaxy. But the loading factor is different in two scenarios, from energy conservation we have $\eta \propto 1/\sigma^2$ and from momentum conservation, one obtains $\eta \propto 1/\sigma$ (e.g., Choi & Nagamine, 2010).

1.3 Cosmological Simulations with Gastrophysics

As has been the case for the Lyα forest, cosmological hydrodynamical simulations of large scale structure formation are also an essential tool to study the enrichment of the IGM. Comparing gas properties (such as temperature and metallicity) from simulations to the ones derived from metal absorption lines in observed QSO spectra, or directly comparing metal absorption features in artificial spectra generated from simulations to observed ones, can improve our knowledge about how metals in the IGM are distributed and the correlation between metal absorbers and galaxies (e.g., Theuns et al., 2002; Aguirre et al., 2005; Oppenheimer & Davé, 2006; Cen & Chisari, 2010). There are two popular schemes for cosmological numerical hydrodynamics: Eulerian adaptive grid methods and Lagrangian particle methods (cf. Chapter 2 for a detailed description). In this work we use a Lagrangian scheme - Smoothed Particle Hydrodynamics (SPH), where there is no fixed grid and the continuous fluid properties are modeled by discrete particles weighted by a smoothing kernel. Because of its ability of following large density variations and conserving angular momentum, SPH is the most commonly adopted scheme for cosmological simulations. The advantage of using cosmological scale simulations is that the simulation volume contains a substantial sample of the universe so that we can compare the statistical properties of the metal absorbers. However, unlike the Lyα forest, studying enrichment of the IGM requires modeling the processes within galaxies such as star formation and supernova feedback, and the inability to resolve these processes is thus a limiting factor. Although this is a problem faced by all simulations, we will discuss this in the following sections in the context of SPH.

1.3.1 Star Formation and Feedback

Although detailed hydrodynamical simulations of the interstellar medium (ISM) in galaxies (e.g,, Mac Low & Ferrara, 1999; Strickland & Stevens, 2000; Williams & Dyson, 2002) have been able to generate galactic outflows and have explored various properties of winds and the gas dynamics in different phases, current cosmological simulations lack the resolution to launch winds from first principles. Hot, low density SN bubbles are unresolved in such simulations which initially led to an overcooling problem that produced unrealistically concentrated simulated galaxies (Navarro & Steinmetz, 1997). As a result, various "subgrid" stellar feedback and wind models have emerged. These models mainly serve two functions: to regulate star formation and the properties of the ISM and to redistribute gas (and newly formed metals) both within galaxies and into the environment around them. There are three main approaches, energetic feedback, kinetic feedback and modifications to the effective equation of state which behave similarly to an increased effective pressure.

Energetic feedback in its simplest form involves directly adding the stellar feedback as thermal energy on gas particles, but this suffers from over-cooling (Katz et al., 1996). Because of insufficient resolution, the hot, low density gas in an SN explosion cannot be resolved and the thermal energy deposited directly into (large) gas particles is soon radiated away before impacting the gas distribution. To avoid this problem, kinetic feedback (e.g., Navarro & White, 1993; Springel & Hernquist, 2003; Oppenheimer & Davé, 2006; Dalla Vecchia & Schaye, 2008) converts part of the SN energy into kinetic energy in the gas, thus avoiding the fast radiative cooling stage. The effectiveness of kinetic feedback is strongly dependent on the resolution and hydrodynamic method.

Springel & Hernquist (2003) argued that regulated star formation creates an effective pressure in the ISM and this was modelled directly in the GADGET code (Springel & Hernquist, 2003) as part of a recipe for regulated star formation. But even with this, the global SFR is still too high compared to observations. In this effective pressure approach, the gas particles are hybrid particles. Each particle contains a cold phase which represents the condensed clouds in the ISM and a hot phase that represents the ambient hot gas. These two phases are in pressure equilibrium. This leads to a strongly hydrodynamically-coupled, multiphase ISM that does not naturally produce galactic outflows. To combat this the authors added a "superwind" model where selected fluid elements in the star forming region are ejected at fixed speed (484 km/s) and are also hydrodynamically decoupled until they leave the dense star forming region. In this original superwind model, the mass loading factor is also a constant, $\eta = 2$. As to the implementation, star-forming gas particles are stochastically ejected out of the ISM according to the probability determined by local SFR and the mass loading factor. Oppenheimer & Davé (2006) modified the model in a manner referred to as the momentum-driven wind scenario so that the velocity of the wind and the mass loading factor were related to the velocity dispersion of the host galaxy. More recently, Choi & Nagamine (2010) combined the energy-driven wind and momentum-driven wind into a variable velocity outflow model. These superwind feedback prescriptions have been widely used to address problems such as the damped Lyman-α (DLA) absorbers (Nagamine et al., 2004a,b) and the enrichment of the IGM at high and low redshifts (Oppenheimer & Davé, 2006, 2009). According to these works, superwind feedback is essential to suppress overproduction of stars in galaxies and to reproduce the cosmic SFH at high redshift. It also increases the local fraction of the warm-hot intergalactic medium (WHIM) to a sufficient percentage (40% to 50%) to account for the "missing baryons" at $z = 0$. Although aspects of the model compare well with observations, some components do not. For example, the feedback may eject a large amount of cool gas from the galactic disks, which results in a low neutral hydrogen mass density $\Omega_{\rm HI}$ at $z < 2$ (Nagamine et al., 2004a). Also, the interaction between winds and the ISM is usually not modeled in these simulations. Dalla Vecchia & Schaye (2008) found that the ISM plays an important role in regulating the amount of wind that escapes and the morphology of the galaxies. In their model, winds are not hydrodynamically decoupled, which naturally allows for variable mass loading. Another potential problem of the Springel & Hernquist (2003) superwind model, as also pointed out by Dalla Vecchia & Schaye (2008), is that it ejects winds from all star-forming gas in galaxies stochastically, instead of from near the newly formed stars, thus the wind particles ejected may not be be enriched.

A refined version of energetic feedback is adiabatic feedback which treats the overcooling problem by inhibiting gas from cooling until the hot SN bubbles can be resolved (e.g., Thacker & Couchman, 2000; Kay et al., 2002; Sommer-Larsen et al., 2003; Stinson et al., 2006). The pressure of the hot gas accelerates the ISM to generate winds and enrich the IGM. Theuns et al. (2002) used the Kay et al. (2002) adiabatic feedback model that turned off cooling for 10 Myrs for the feedback gas in their cosmological simulations. They found enough metals were carried by strong winds to produce C IV absorption lines that agreed with observations. Aguirre et al. (2005) used the same simulation to compare the optical depth of C IV and C III absorption lines from simulations with observations.

In earlier implementations (Thacker & Couchman, 2000; Kay et al., 2002) the cooling turn-off time is arbitrarily chosen (usually $\sim$ 10 Myr) as an input parameter. Stinson et al. (2006) improved the model by utilizing the analytical blastwave solution (McKee & Ostriker, 1977) for supernova explosions, so that the cooling turn-off time is determined by how long the SN bubble expands, which is a function of injection energy and local density. In the very high resolution limit, this method approaches direct ISM modeling. This is the approach used in this work. In this approach winds are consequences of a feedback model, instead of a phenomenological prescription as in the superwind models. Though energetic feedback is often referred to as supernova feedback, it can be used to model several types of stellar feedback such as winds from young stars and locally deposited radiation energy. The essential quantity is the energy injection rate as a function of the mass in stars and the current age of the stellar population. However in the current work, energy injection from AGN is not included, and the radiation field within galaxies is not modeled. Thus we omit winds that were driven by AGN and the present study is a baseline model which allows room for feedback and winds from other mechanisms.

1.3.2 Radiative Cooling

In IGM enrichment, the role of metals is not just to be carried into the IGM passively. The properties of the enriched IGM are not only affected by winds but also by atomic cooling. Winds enrich galactic halos and the IGM so that metal cooling significantly increases the cooling rates and thus may affect how gas accretes onto galaxies and the star formation rate. Besides the impact on gas dynamics, the IGM temperature itself, together with the UV radiation, determines the ionization states of metal ions. To derive metal abundances from certain absorbers, the gas temperature needs to be accurately modeled (as seen in the C IV case in Section 1.2). Most cosmological simulations today include radiative cooling from primordial species, but cooling due to metals is not always modeled. Aguirre et al. (2005) found that their simulated metal enriched gas was too hot ($\sim 10^5 - 10^7$ K) and suggested that a lack of metal cooling was responsible for discrepancies between simulated and observed C IV absorption.

Oppenheimer & Davé (2006) found better agreement when they included the Sutherland & Dopita (1993) metal cooling model. The same model was used by Choi & Nagamine (2009), who investigated the effect of metal cooling on galaxy growth and found that it increases the local star forming efficiency and enhances accretion onto galaxies. However, the Sutherland & Dopita (1993) model assumes the metal ions are in collisional ionization equilibrium (CIE) where the abundances of metal ions are determined by collisional ionization and recombination. This is not a valid assumption when an ultraviolet (UV) radiation background is present, because photoionization from UV radiation significantly changes the number density of electrons and affects the ionization equilibrium reached (cf. Chapter 3). Since the IGM is surely subject to UV radiation, a more self-consistent model of metal cooling with UV is required. This is investigated in detail in the current work and also in Wiersma et al. (2009a).

1.3.3 Turbulent Mixing

Another important aspect of metal enrichment is the mixing of metals between the wind and the surrounding gas. The interstellar medium is highly turbulent and SN explosions are likely to be a major driver of the turbulence (Mac Low & Klessen, 2004). Oppenheimer & Davé (2009) found that turbulent motions also exists in the low redshift IGM, producing the observed line width distribution of OVI. In addition, large velocity shear (such as between a wind and a gaseous halo) naturally generates turbulence and mixing. Turbulent mixing redistributes metals and thermal energy between the wind fluid and the ambient gas. This changes the metallicity, temperature and future evolution of the gas. While metal mixing is expected in strong outflows, it is still unclear how mixing impacts the IGM. For example, observations by Schaye et al. (2007) inferred a population of compact ($\sim$ 100 pc), transient C IV absorbers that are highly enriched, suggesting poor chemical mixing at small scales. These absorbers were interpreted as an enriched clumpy medium embedded within hot galactic wind fluids. If velocity shear is the major mechanism for turbulent mixing between winds and the surroundings, then this poor mixing could be explained if the clouds are carried by hot winds at the same speed. However to investigate this in detail, one must resolve wind structures, which is beyond current cosmological simulations. In this work we will focus on subgrid turbulent mixing models in the cosmological context. In SPH simulations (which represent the majority of work in this area), the fluid is modeled by discrete particles. This implies that newly injected metals are locked into specific particles. For example, it was found that the distribution of metals from SPH simulations is too inhomogeneous compared with observations (Aguirre et al., 2005). To assess the potential importance of mixing, Wiersma et al. (2009) used SPH-smoothed metallicities and compared them with conventional particle metallicities, and found smoothing is able to generate significantly more material with low metallicities. This approach cannot capture the spread of metals over time with its impact on cooling and the thermal history of the gas. Directly modeling the turbulent ISM within a cosmological simulation is far beyond current capabilities. We employed a variant of the Smagorinsky (1963) subgrid turbulent diffusion model, in which unresolved turbulent mixing is treated as a shear-dependent diffusion term. Metal cooling was calculated based on the diffused metals so that its non-local effects could be investigated.

1.4 This Work and Organization of Chapters

In this work, we present an analysis of a series of SPH cosmological simulations that incorporated adiabatic stellar feedback, detailed metal cooling and turbulent mixing to study the evolution and enrichment of the IGM. The feedback model was kept simple, following the adiabatic stellar feedback approach of Stinson et al. (2006). This model has been calibrated via numerous galaxy formation studies (e.g., Governato et al., 2007). No additional wind prescriptions were used. With this approach, outflows arise from stellar feedback within the ISM and there is no distinction between the feedback that regulates star formation and that which drives galactic outflows. Thus this work establishes a baseline for the effectiveness of moderate stellar feedback coupled with key physical process absent from other work to reproduce the properties of the IGM. These results may be compared with explicit wind models. A further goal of this work is to separately quantify the impact of metal cooling and turbulent mixing on the star formation history (SFH), the global properties and the evolution of the IGM and its enrichment.

This thesis is organized as follows. Chapter 2 briefly describes the N-body and SPH code, GASOLINE (Wadsley et al., 2004) and the subgrid models for star formation, adiabatic supernova feedback, turbulent metal mixing and the generation of cosmological initial conditions. Chapter 3 investigates in detail how radiative cooling rates (primordial and metal) are affected by photoionization, and introduces a self-consistent metal cooling model under an evolving UV background. The impact of non-equilibrium effects on primordial cooling and the impact of cosmic rays are also discussed. Chapter 4 presents the major results from the simulations. In this chapter, we first examine the cosmic star formation history, global H I density and Ly-α decrement in order to calibrate our feedback and demonstrate the overall consistency of our models. Then we focus on the evolution of the baryonic mass, metal fractions and metallicities in stars and different gas phases. We compare those results to the observed metal fractions and metallicities at different epochs, and with simulations using different subgrid feedback models from Oppenheimer & Davé (2006), Davé & Oppenheimer (2007) and Wiersma et al. (2009). We then analyze in detail the distribution of mass and metallicity in the density-temperature phase diagram at z = 0 and the density-metallicity relationship. In each section of this Chapter, where relevant, we have included detailed analysis of the effects of metal cooling and diffusion, and comparisons with observations. In Chapter 5 we first characterize our wind generation mechanism as a function of galaxy mass to obtain a better understanding of how different phases of the IGM get enriched. Then we investigate when and where the wind material at z = 0 came from as a function of current density and temperature of the wind gas. We present a method to qualitatively characterize the mass-loading factor of the wind generated by the adiabatic feedback and compare the mass-loading with the assumed ratios used in explicit superwind models. The contents of Chapter 4 and part of Chapter 5 have been published as Shen et al. (2010). Finally in Chapter 6, we summarize and discuss the broader implications of the results and some prospects for future work.

Bibliography

Adelberger, K. L., Steidel, C. C., Shapley, A. E., & Pettini, M. 2003, ApJ, 584, 45

Adelberger, K. L., Shapley, A. E., Steidel, C. C., Pettini, M., Erb, D. K., & Reddy, N. A. 2005, ApJ, 629, 636

Aguirre, A., Hernquist, L., Schaye, J., Katz, N., Weinberg, D. H., & Gardner, J. 2001, ApJ, 561, 521

Aguirre, A., Schaye, J., Kim, T.-S., Theuns, T., Rauch, M., & Sargent, W. L. W. 2004, ApJ, 602, 38

Aguirre, A., Schaye, J., Hernquist, L., Kay, S., Springel, V., & Theuns, T. 2005, ApJL, 620, L13

Aguirre, A., & Schaye, J. 2007, EAS Publications Series, 24, 165

Binney, J. & Merrifield, M. *Galactic Astronomy*, Princeton University Press, 1998

Cecil, G., Bland, J., & Tully, R. B. 1990, ApJ, 355, 70

Cen, R., Miralda-Escudé, J., Ostriker, J. P., & Rauch, M. 1994, ApJ, 437, L9

Cen, R., & Chisari, N. E. 2010, arXiv:1005.1451

Choi, J.-H., & Nagamine, K. 2009, MNRAS, 393, 1595

Choi, J.-H., & Nagamine, K. 2010, arXiv:1001.3525

Cole, S., et al. 2005, MNRAS, 362, 505

Dalla Vecchia, C., & Schaye, J. 2008, MNRAS, 387, 1431

Davé, R., Hellsten, U., Hernquist, L., Katz, N., & Weinberg, D. H. 1998, ApJ, 509, 661

Davé, R., & Oppenheimer, B. D. 2007, MNRAS, 374, 427

Ellison, S. L., Songaila, A., Schaye, J., & Pettini, M. 2000, AJ, 120, 1175

Governato, F., Willman, B., Mayer, L., Brooks, A., Stinson, G., Valenzuela, O., Wadsley, J., & Quinn, T. 2007, MNRAS, 374, 1479

Heckman, T. M., Armus, L., & Miley, G. K. 1990, ApJS, 74, 833

Heckman, T. M., Lehnert, M. D., Strickland, D. K., & Armus, L. 2000, ApJS, 129, 493

Heckman, T. M. 2001, Gas and Galaxy Evolution, 240, 345

Hernquist, L., Katz, N., Weinberg, D. H., & Miralda-Escudé, J. 1996, ApJ, 457, L51

Katz, N., Weinberg, D. H., & Hernquist, L. 1996, ApJS, 105, 19

Kay, S. T., Pearce, F. R., Frenk, C. S., & Jenkins, A. 2002, MNRAS, 330, 113

Komatsu, E., et al. 2009, ApJS, 180, 330

Lynds, C. R., & Sandage, A. R. 1963, ApJ, 137, 1005

Mac Low, M.-M., & Ferrara, A. 1999, ApJ, 513, 142

Mac Low, M.-M., & Klessen, R. S. 2004, Reviews of Modern Physics, 76, 125

McKee, C. F., & Ostriker, J. P. 1977, ApJ, 218, 148

Murray, N., Quataert, E., & Thompson, T. A. 2005, ApJ, 618, 569

Nagamine, K., Springel, V., & Hernquist, L. 2004, MNRAS, 348, 421

Nagamine, K., Springel, V., & Hernquist, L. 2004, MNRAS, 348, 435

Navarro, J. F., & White, S. D. M. 1993, MNRAS, 265, 271

Navarro, J. F., & Steinmetz, M. 1997, ApJ, 478, 13

Oppenheimer, B. D., & Davé, R. 2006, MNRAS, 373, 1265

Oppenheimer, B. D., & Davé, R. 2009, MNRAS, 395, 1875

Peacock, J. A., *Cosmological Physics*, Cambridge University Press, 1999

Peebles, P. J. E., *Principles of Physical Cosmology*, Princeton University Press, 1993

Pettini, M., Steidel, C. C., Adelberger, K. L., Dickinson, M., & Giavalisco, M. 2000, ApJ, 528, 96

Pettini, M., Shapley, A. E., Steidel, C. C., Cuby, J.-G., Dickinson, M., Moorwood, A. F. M., Adelberger, K. L., & Giavalisco, M. 2001, ApJ, 554, 981

Pettini, M., Rix, S. A., Steidel, C. C., Adelberger, K. L., Hunt, M. P., & Shapley, A. E. 2002, ApJ, 569, 742

Pettini, M., Madau, P., Bolte, M., Prochaska, J. X., Ellison, S. L., & Fan, X. 2003, ApJ, 594, 695

Pieri, M. M., Schaye, J., & Aguirre, A. 2006, ApJ, 638, 45

Porciani, C., & Madau, P. 2005, ApJ, 625, L43

Putman, M. E., et al. 2009, astro2010: The Astronomy and Astrophysics Decadal Survey, 2010, 241

Ryan-Weber, E. V., Pettini, M., & Madau, P. 2006, MNRAS, 371, L78

Scannapieco, E., Ferrara, A., & Madau, P. 2002, ApJ, 574, 590

Schaye, J., Rauch, M., Sargent, W. L. W., & Kim, T.-S. 2000, ApJL, 541, L1

Sargent, W. L. W., Boksenberg, A., & Steidel, C. C. 1988, ApJS, 68, 539

Schaye, J., Aguirre, A., Kim, T.-S., Theuns, T., Rauch, M., & Sargent, W. L. W. 2003, ApJ, 596, 768

Schaye, J., Carswell, R. F., & Kim, T.-S. 2007, MNRAS, 379, 1169

Seljak, U., & Zaldarriaga, M. 1996, ApJ, 469, 437

Shen, S., Wadsley, J., & Stinson, G. 2010, MNRAS, 1043

Simcoe, R. A., Sargent, W. L. W., & Rauch, M. 2004, ApJ, 606, 92

Simcoe, R. A. 2006, AJ, 653, 977

Smagorinky, J., 1963, Monthly Weather Rev., 91, 3, 99

Sommer-Larsen, J., Götz, M., & Portinari, L. 2003, ApJ, 596, 47

Songaila, A., & Cowie, L. L. 1996, AJ, 112, 335

Songaila, A. 2005, AJ, 130, 1996

Springel, V., & Hernquist, L. 2003, MNRAS, 339, 312

Springel, V., et al. 2005, Nature, 435, 629

Steidel, C. C., Erb, D. K., Shapley, A. E., Pettini, M., Reddy, N., Bogosavljević, M., Rudie, G. C., & Rakic, O. 2010, ApJ, 717, 289

Stinson, G., Seth, A., Katz, N., Wadsley, J., Governato, F., & Quinn, T. 2006, MNRAS, 373, 1074

Stoughton, C., et al. 2002, AJ, 123, 485

Strickland, D. K., & Stevens, I. R. 2000, MNRAS, 314, 511

Strickland, D. K., Heckman, T. M., Colbert, E. J. M., Hoopes, C. G., & Weaver, K. A. 2004, ApJ, 606, 829

Sutherland, R. S., & Dopita, M. A. 1993, ApJS, 88, 253

Swinbank, A. M., et al. 2005, MNRAS, 359, 401

Thacker, R. J., & Couchman, H. M. P. 2000, ApJ, 545, 728

Theuns, T., Mo, H. J., & Schaye, J. 2001, MNRAS, 321, 450

Theuns, T., Viel, M., Kay, S., Schaye, J., Carswell, R. F., & Tzanavaris, P. 2002, ApJL, 578, L5

Veilleux, S., Cecil, G., & Bland-Hawthorn, J. 2005, ARA&A, 43, 769

Wadsley, J. W., & Bond, J. R. 1997, Computational Astrophysics; 12th Kingston Meeting on Theoretical Astrophysics, 123, 332

Wadsley, J. W., Stadel, J., & Quinn, T. 2004, New Astronomy, 9, 137

Walter, F., Weiss, A., & Scoville, N. 2002, ApJ, 580, L21

White, S. D. M., & Rees, M. J. 1978, MNRAS, 183, 341

Wiersma, R. P. C., Schaye, J., & Smith, B. D. 2009, MNRAS, 393, 99

Wiersma, R. P. C., Schaye, J., Theuns, T., Dalla Vecchia, C., & Tornatore, L. 2009, MNRAS, 399, 574

Williams, R. J. R., & Dyson, J. E. 2002, MNRAS, 333, 1

Zhang, Y., Anninos, P., & Norman, M. L. 1995, ApJ, 453, L57

Chapter 2

Method and Simulations

Simulating how the intergalactic medium is enriched is challenging. It requires that the simulation contain a substantial sample of the universe to examine the evolution of the IGM and its interaction with galaxies. Meanwhile, it requires correct modeling the physical processes that happen at much smaller scales, such as supernova feedback, metal injection, radiative cooling due to metals and chemical mixing due to turbulence in the IGM. While gravity and hydrodynamical equations can be evolved directly in simulations, the smaller-scale physical processes such as star formation and supernova feedback are below the resolution limit of current cosmological simulations. These processes are treated via "subgrid" models. In this study I use the Tree + Smoothed Particle Hydrodynamics code GASOLINE (Wadsley et al., 2004) for gravity and hydrodynamics, a star formation and adiabatic supernova feedback model (Stinson et al., 2006), a self-consistent treatment of metal cooling under the presence of evolving ultraviolet radiation and a Smagorinsky diffusion model for mixing of thermal energy and metals (Wadsley, Veeravalli &

Couchman , 2008). In this Chapter I will briefly describe the hydrodynamics in GASOLINE (Section 2.1), the SN feedback (Section 2.2) and the turbulent diffusion models (Section 2.3). Metal cooling and non-equilibirum ionization of primordial species will be described in a separate chapter (Chapter 3). In the last part of this chapter I will present how cosmological initial conditions are constructed, and list the simulations and parameters (Section 2.4)

2.1 Gravity and Hydrodynamics

The simulations in this work were evolved using the parallel code GASOLINE (Wadsley et al., 2004). The code uses the hierarchical tree method for gravity calculations and the smoothed particle hydrodynamics (SPH) method for fluid dynamics.

2.1.1 Gravity

Gravity is the driving force for the evolution of astronomical systems. In Newtonian physics, in a system with discrete objects, the gravitational acceleration for object i is:

$$\vec{a_i} = \sum_{j \neq i} \frac{GM_j(\vec{r_i} - \vec{r_j})}{|\vec{r_i} - \vec{r_j}|^3} \tag{2.1}$$

where G is Newton's gravitational constant, and $\vec{r}$ is the position of the objects. Early N-body simulations directly perform equation 2.1 to calculate the acceleration. For a system with N objects, it is a calculation of order N^2(i.e., $\mathcal{O}(N^2)$). This becomes impractical when the number of object is large like in astrophysical simulations today. Many algorithms have been developed to reduce the order of calculation to $\mathcal{O}(N \log N)$, including the Particle-Particle Particle-Mesh (P^3M) (Efstathiou et al., 1985; Couchman, 1991) method using the Fast Fourier Transform and the Hierarchical Tree method (Barnes & Hut, 1986).

The idea behind a tree method is that since gravity falls off as $1/r^2$, the detailed distribution of remote masses is not as important as that of closer ones and thus the forces from remote masses can be approximated. A binary tree structure can be built by dividing the simulation box down to regions that contain only a small number of particles. The root node corresponds to the whole box and every subsequent level of tree corresponds to the volume after one more division. GASOLINE uses a spatial binary tree to calculate gravity. In GASOLINE, a leaf node is called a bucket. For a certain particle i, forces by other particles in the same bucket B_i are calculated directly using equation 2.1. For other buckets and upper nodes, an opening radius r_{open} relative to the center of mass of B_i is used as a criterion. Any buckets or nodes which does not intersect with r_{open} are not opened, and forces are calculated approximately using multipole expansions to the fourth order. Otherwise, they are opened. For open nodes the intersection test is repeated on their child nodes until leaf buckets are reached. All the particles in the open buckets interact directly with particle i.

Note that the Newtonian gravity goes to infinity when the particle separation $\vec{r}$ approaches zero. GASOLINE uses a gravitational softening length, ϵ, to reduce the gravitational force when the particle-particle separation is too small. Within ϵ, the force is smoothed using the same spline kernel as in the Smooth Particle Hydrodynamics (SPH, cf. Section 2.1.2). An alternative way is to treat particles as spheres with smoothed density distributions using the same smoothing kernel as in the SPH calculations. Gravitational softening helps reduce the noise in simulations, increase integration timesteps and produces a smoother gravitational potential for the objects formed in simulations.

2.1.2 Hydrodynamics

Astronomical systems contain highly compressible gas with its dynamics described by Euler's equations. To solve these equations numerically, there exist two fundamentally different classes of methods: Eulerian methods and Lagrangian methods. The former solve the fluid equations on a fixed grid by calculating mass, momentum and energy fluxes on cell boundaries, while the latter solves the equations in a comoving reference frame following the fluid flow. The advantages of Lagrangian methods are that the resolution follows the mass flow, and the methods follow orbits well, which make them suitable for simulating the formation of large scale structure and disk galaxies. Smoothed Particle Hydrodynamics (SPH) is a Lagrangian method that is widely used in cosmological simulations. The principle of the SPH method is to represent continuous fluid fields (e.g., density) with a set of discrete particles, and interpolate values at any point with a kernel function W. For example, the density at position $\vec{r}$ can be represented as a weighted summation over all discrete masses (Monaghan, 1992),

$$\rho(\vec{r}) = \sum_i m_i W(\vec{r} - \vec{r}_i, h) \tag{2.2}$$

The weight function, W, is a smooth function having the following properties

$$\int W(\vec{r} - \vec{r'}, h) d\vec{r'} = 1 \tag{2.3}$$

and

$$\lim_{h \to 0} W(\vec{r} - \vec{r'}, h) = \delta(\vec{r} - \vec{r'}) \tag{2.4}$$

Here, h is the smoothing length, the characteristic length over which W falls off quickly. The immediate advantage of SPH is that all the spatial derivatives can be represented by derivatives of the kernel function, and as a result, all the partial differential equations in fluid mechanics become ordinary differential equations, which largely simplifies the numerical integration.

Similar to the mass equation, in GASOLINE, the momentum and energy equations can be written as (Wadsley et al., 2004; Monaghan, 1992):

$$\frac{d\vec{v_i}}{dt} = -\sum_{j=1}^{n} m_j \left(\frac{P_i}{\rho_i^2} + \frac{P_j}{\rho_j^2} + \Pi_{ij}\right) \nabla_i W_{ij} \tag{2.5}$$

and

$$\frac{du_i}{dt} = \sum_{j=1}^{n} \left(\frac{P_i}{\rho_i^2} + \frac{\Pi_{ij}}{2}\right) m_j \vec{v_{ij}} \cdot \nabla_i W_{ij} \tag{2.6}$$

where W_{ij}, v_i, u_i, ρ_i, P_i are the kernel function, velocity, internal energy, density and pressure of particle i, respectively. Π_{ij} is an artificial viscosity term to model entropy generation in shocks and to prevent unphysical interpenetration of gas flows.

To conserve energy and momentum during the calculation, GASOLINE uses a symmetric smoothing kernel so that $W_{ij} = W_{ji}$

$$W_{ij} = \frac{1}{2}w(|\vec{r_i} - \vec{r_j}|/h_i) + \frac{1}{2}w(|\vec{r_i} - \vec{r_j}|/h_j) \quad (2.7)$$

where h_i and h_j are the smoothing lengths for particles i and j and w(x) is a spline function defined in Monaghan (1992) which decreases to 0 when $x > 2$. The smoothing length h for each particle is obtained by finding N_{nbr} (~ 50 in our simulations) nearest neighbouring particles and setting $2h$ equal the distance to the last particle found.

2.2 Star Formation and Supernova Feedback

Because current cosmological simulations cannot resolve the interstellar medium, individual star formation (SF) and supernova explosions (SNe), various sub-grid "recipes" have been developed to model how SF and its feedback impact the surrounding gas in galaxies and the IGM. The star formation and feedback recipes used here constitute the "blastwave model" described in detail in Stinson et al. (2006), and they are summarized in the following sections.

2.2.1 Star Formation

To form stars, gas particles must be dense and cool, and in a convergent flow (i.e., $\nabla \cdot \vec{v} < 0$). In this work I use $n_{\rm min} = 0.1$ cm^{-3} for the density threshold and $T_{\rm max} = 15{,}000$ K for the maximum temperature of a star-forming particle for all simulations. The value of $n_{\rm min}$ and $T_{\rm max}$ is calibrated in galaxy formation simulations using GASOLINE by Stinson et al. (2006). Governato et al. (2007) also used the same $n_{\rm min}$ and formed realistic Milky Way-like disk galaxies in their simulations. A subset of the particles that pass these criteria are stochastically selected to form stars based on the commonly used star formation equation,

$$\frac{dM_\star}{dt} = c_\star \frac{M_{gas}}{t_{dyn}} \tag{2.8}$$

where $M_\star$ is mass of stars created, $c_\star$ is a constant star formation efficiency factor, M_{gas} is the mass of gas creating the star and t_{dyn} is the gas dynamical time. The constant parameter, $c_\star$ was set to 0.05 so that a simulated isolated model Milky Way matches the observed relationship between gas surface density and the star formation rate (SFR) – the Kennicutt-Schmidt Law (Kennicutt, 1998). Gas particles passing all the criteria form one star particle. The initial mass of the star particle remains constant throughout the simulation and is set as one-third of the original gas mass (which is between 10^6 $M_\odot$ and 10^7 $M_\odot$ in this work). The mass of the gas particle decreases as it is being converted into stars, and when it is less than 10 % of the original gas particle mass, the gas particle is deleted from the simulation and its mass is distributed to its neighbouring particles.

2.2.2 Stellar Feedback

At the resolution of cosmological simulations, each particle represents a whole population of stars. In a stellar population, the number of stars as a function of mass is described by an initial mass function (IMF). In this work, each star particle contains stars that cover the entire initial mass function presented in Kroupa et al. (1993). Stars with different masses evolve differently and have different lifetimes. The stellar lifetimes as a function of mass and metallicity is calculated as described Raiteri et al. (1996). Supernova rates for Type

II (SN II), Type Ia (SN Ia) were calculated also according to Raiteri et al. (1996). As stellar lifetime is a monotonic function of stellar mass, it is possible to determine the minimum and maximum mass (M_{min} and M_{max}) that will explode during a certain timestep. So the integration over the IMF with limits of M_{min} and M_{max} will give the total number and mass of the supernova. Stars larger than 8 $M_{\odot}$ and less than 40 $M_{\odot}$ explode as SN II. The explosion of SN will inject energy E_{SN} (usually a fraction of 10^{51} ergs) into the surrounding gas. But since the hot SN bubbles cannot be resolved in the simulation, simply injecting SN energy into dense, massive gas particles leads to unrealistically rapid radiative loss of the energy. To solve this problem the explosion of these stars is treated using the analytic model for blastwaves presented in McKee & Ostriker (1977). The model estimates the radius a superbubble can expand to (the blast radius, R_E), and the time scale (t_{max}) that the hot, low density superbubble shell can survive as a function of injected SN energy, local gas density and ambient gas pressure:

$$R_E = 10^{1.74} E_{51}^{0.32} n_0^{-0.16} P_{04}^{-0.20} \mathrm{pc} \tag{2.9}$$

$$t_{max} = 10^{6.85} E_{51}^{0.32} n_0^{0.34} P_{04}^{-0.70} \mathrm{yr} \tag{2.10}$$

where $E_{51} = E_{SN}/10^{51}$, n_0 is the ambient hydrogen number density and $P_{04} = 10^{-4} P_0 k^{-1}$ where P_0 is the pressure of the ambient gas and k is the Boltzmann constant. Note that to generate a superbubble many SN explosions need to co-exsist spatially and temporarily. So the energy injection E_{SN} is the sum of the energies from all SN explosions and thus can be much larger than the canonical energy of one SN explosion, 10^{51} ergs. The effect of (unresolved)

SN hot bubble is approximated by suppressing the radiative cooling of gas particles for the same time that the superbubble survives (Equation 2.10). While the blast radius and the cooling suppression time are calculated using the full energy output for each supernova explosion (i.e. 10^{51} ergs), less than half of that energy is transferred to the surrounding ISM. We use 4×10^{50} ergs for the energy injection per SN explosion. The rest of the supernova energy is assumed to be radiated away. The energy is transferred to the ISM by volume weighting, as also used in Mashchenko et al. (2008). Each affected gas particle, with mass m_i and density ρ_i receives a fraction of the SN energy and metals proportional to $m_i W_{ij}/\rho_i$, where W_{ij} is the SPH smoothing kernel. A similar method was also adopted in Wiersma et al. (2009) for the distribution of metals and the energy from SN Ia. The Blastwave model, as currently implemented, has a bias for more cooling suppression at earlier epochs relative to other approaches. Numerical feedback recipes differ substantially from code to code and their results vary with resolution. This provides motivation for the characterization of star formation regulation and wind generation in these simulations that is presented in Chapter 5. Binary systems with masses 3-16 $M_\odot$ are able to produce SN Ia, and the number of SN Ia during a timestep is calculated from integrating the initial mass function of the secondary in the binary system. Each SN Ia also ejects 4×10^{50} ergs into the surroundings gas but radiative cooling was not disabled for SN Ia, because SN Ia happen much later than SN II, when stars should have dispersed, and no strong collective effect or large blastwave are expected.

Metal enrichment from SN II and SN Ia follows the model of Raiteri et al. (1996), but metal production of AGB stars is not included. For SN II, metals produced in stars are released as the main sequence progenitors die and are distributed to the same gas as is influenced by the energy ejected from SN II. Iron and Oxygen are produced in SN II according to the analytic fits used in Raiteri et al. (1996) using the yields from Woosley & Weaver (1995):

$$M_{Fe} = 2.802 \times 10^{-4} M_{\star}^{1.864} \tag{2.11}$$

$$M_{O} = 4.586 \times 10^{-4} M_{\star}^{2.721} \tag{2.12}$$

Each SN Ia produces 0.63 $M_{\odot}$ Iron and 0.13 $M_{\odot}$ Oxygen (Thielemann et al., 1986) and the metals are ejected into the nearest gas particle. Stellar wind feedback was implemented based on Kennicutt et al. (1994), and the returned mass fraction was determined using a function derived by Weidemann (1987). The returned gas has the same metallicity as the star particle.

2.3 Turbulent Metal Diffusion

Astrophysical fluids such as the ISM, the IGM, and galactic outflows are expected to have very high Reynolds number ($Re = vL/\nu$ where v is the velocity of the fluid, L is the characteristic length scale of the flow and ν is the viscosity coefficient). This implies advective terms dominate the flow compared to dissipative terms. Flows with high Reynolds numbers are extremely turbulent and mixing of heat and metals occurs due to the turbulent motion. Modeling turbulent motions in simulations is important but very challenging, because as the turbulence cascades to smaller scales, at some scale numerical dissipation always dominates physical dissipation. For an Eulerian method, without turbulence, the full derivative of internal energy (same for other scalars) du/dt

in the energy equation (cf. Equation 2.6) is expressed as $\partial u/\partial t + (\vec{v} \cdot \nabla)u$. The second term denotes the advection which is computed explicitly. When moving the fluid through a fixed grid diffusion occurs, thus mixing is accidentally modeled to some extent. On the other hand, Lagrangian particle method like SPH does not include any implicit or explicit diffusion of scalar quantities such as energy and metals. In Equation 2.6, du_i/dt is computed along a fluid particle i and no advection is modeled. Wadsley, Veeravalli & Couchman (2008) demonstrated that this has physically incorrect consequences for even simple processes such as convection and Rayleigh-Taylor instabilities.

One common approach to approximate turbulence is to decompose the flow into an averaged, resolved, flow and an unresolved component with its mean value equals zero, and then model the unresolved flow as a diffusion term. For example,

$$\frac{\partial \bar{u}}{\partial t} + \bar{\mathbf{v}} \cdot \nabla \bar{u} = -(\gamma - 1)\bar{u}(\nabla \cdot \mathbf{v}) + \nabla(D\nabla \bar{u}) \tag{2.13}$$

where $\bar{u}$, $\bar{\mathbf{v}}$ are the energy and velocity of the resolved flow, respectively, γ is the ratio of specific heats (here the equation of state $P/\rho = (\gamma - 1)u$ is used), and D is the diffusion coefficient. Including a simple model for turbulent mixing (using a diffusion coefficient, $D = C\,\Delta\,v\ h_{\rm SPH}$ based on the pairwise velocity, $\Delta\,v$, at the resolution scale, $h_{\rm SPH}$ and $C \sim 0.1$) Wadsley, Veeravalli & Couchman (2008) were able to match Eulerian grid code results (which must mix due to the necessary advection estimates). In particular, it became possible to generate similar non-radiative galaxy cluster entropy profiles with SPH as with high resolution grid codes. This was a major discrepancy in the Santa Barbara Cluster Comparison Project (Frenk et al., 1999). The project compared simulations of the formation of a galaxy cluster using 12 different codes which employed either Lagrangian or Eulerian methods. Gas is not radiative (i.e. no radiative cooling) in these simulations. One of the discrepancies was the radial entropy profile: while mesh codes generated an entropy core, SPH codes produced a profile that decrease steadily towards the center of the cluster. The reason is likely due to the fact that SPH methods are Lagrangian and do not mix entropy, but Eulerian methods have advection terms which have numerical diffusion and allow mixing to occur. Greif et al. (2009) implemented a similar scheme and applied it to simulating supernova remnants. As discussed previously, galactic outflows should be highly turbulent and thus mixing is essential for IGM studies.

Turbulent mixing models have a long history in environmental and engineering fluid mechanics. Implemented by Dr. James Wadsley, GASOLINE now incorporates a more robust mixing estimator similar to that first proposed by Smagorinsky (1963) for the atmospheric boundary layer. For any scalar A, its full derivative due to diffusion $\frac{dA}{dt}|_{\mathrm{Diff}}$ is given by,

$$\begin{aligned} \frac{dA}{dt}|_{\mathrm{Diff}} &= \nabla(D\nabla A), \\ D &= C\,|S_{ij}|\,h^2, \end{aligned} \tag{2.14}$$

we use the trace-free shear tensor for S_{ij} and h is the measurement scale (here $\sim h_{SPH}$). This choice for S_{ij} results in no diffusion for purely compressive or uniformly rotating flows. In SPH terms the diffusion expression for a scalar A_p on particle p is computed as follows,

$$\tilde{S}_{ij}|_p = \frac{1}{\rho_p}\sum_q m_q(v_j|_q - v_j|_p)\nabla_{p,i}W_{pq},$$

$$
\begin{aligned}
S_{ij}|_p &= \frac{1}{2}(\tilde{S}_{ij}|_p + \tilde{S}_{ji}|_p) - \delta_{ij}\frac{1}{3}\ \mathrm{Trace}\ \tilde{S}|_p, \\
D_p &= C\ |S_{ij}|_p|\ h_p^2, \\
\frac{dA_p}{dt}|_{\mathrm{Diff}} &= -\sum_q m_q \frac{(D_p + D_q)(A_p - A_q)(\mathbf{r}_{pq} \cdot \nabla_p W_{pq})}{\frac{1}{2}(\rho_p + \rho_q)\,\mathbf{r}_{pq}^2},
\end{aligned}
\tag{2.15}
$$

where the sums are over SPH neighbours, q, δ_{ij} is the Kronecker delta, W is the SPH kernel function, ρ_q is the density, $\mathbf{r}_{pq}$ is the vector separation between particles, $v_i|_q$ is the particle velocity component in direction i, ∇_p is the gradient operator for particle p (operating on the SPH kernel function) and $\nabla_{p,i}$ is the ith component of the resultant vector. The difference between this model and the one used in Wadsley, Veeravalli & Couchman (2008) and Greif et al. (2009) is that the diffusion coefficient is calculated according to a turbulent mixing model instead of simply using velocity differences. The coefficient depends on the velocity shear hence it better models the mixing in shearing flows. On the other hand, if there is no shearing motion between two phases of fluids (such as a clumpy medium embedded in hot wind fluid and the two move with same speed), then no turbulent diffusion is added. The Smagorinsky model has also been used successfully in other fields such as weather modeling and engineering fluid flow modeling (Pope, 2000).

A coefficient value of order $0.05 - 0.1$ is expected from turbulence theory (depending on the effective measurement scale, h). It was found that a conservative choice of $C = 0.05$ was sufficient to match the cluster comparison. This diffusion was applied to thermal energy and metals in all runs except the one with no diffusion. Diffusion of density results naturally from the noise in the velocity field which moves particles around.

2.4 Initial Conditions and List of Simulations

Large-scale structures and galaxies form from gravitational collapse of initial density perturbations produced by quantum fluctuations in the very early Universe. The power spectrum of the initial perturbations can be precisely derived from observations of the angular temperature fluctuations of the CMB (e.g., Komatsu et al., 2009) and readily computed by softwares such as CMBFAST (Seljak & Zaldarriaga, 1996). The first step to perform a cosmological simulation is to generate an initial condition with initial density perturbations that follow the power spectrum. A common way to set up density fluctuations in an N-body simulation is to use the Zel'dovich approximation (Zel'Dovich, 1970), which utilizes the first-order Lagrangian perturbation theory,

$$\mathbf{x} = \mathbf{q} + \mathbf{f}(\mathbf{q}) \tag{2.16}$$

$$\dot{\mathbf{x}} = \dot{\mathbf{f}}(\mathbf{q}) \tag{2.17}$$

$$\nabla^2\phi(\mathbf{q}) = -4\pi G\rho_0\delta \tag{2.18}$$

$$\mathbf{f}(\mathbf{q}) = -\nabla\phi(\mathbf{q}) \tag{2.19}$$

where $\mathbf{q}$ and $\mathbf{x}$ are the initial and final position, respectively, $\dot{\mathbf{q}}$ is comoving final velocity, $\mathbf{f}$ is the force (displacement) field, δ is the overdensity defined as $\delta(\mathbf{q}) = \rho/\rho_0 - 1$, and ρ_0 is the mean density. The force field is usually calculated by taking spatial derivative of $\phi(\mathbf{q})$, the gravitational potential caused by the density fluctuation. It is also convenient to Fourier transform $\delta(\mathbf{q})$, $\phi(\mathbf{q})$ and $\mathbf{f}(\mathbf{q})$ into k space, $\hat{\delta}(k)$, $\hat{\phi}(k)$ and $\hat{f}(k)$ so that the Laplacian can be solved easily. In practice, the steps of making an IC include (i): In k space, obtain a CMB power spectrum $\mathcal{P}(k) = |\hat{\delta}(k)|^2$ extrapolated to current epoch from linear integrators such as CMBFAST (Seljak & Zaldarriaga, 1996) (ii) Populate a 3D grid of $\hat{\delta}(k)$ using the power spectrum, where the lowest k ($2\pi/L$ and L is the box size) and highest k ($2\pi/\Delta x$, where Δx is the 1D resolution $L/N^{1/3}$) values are determined by the size of the simulation and the resolution. (iii) Convert $\hat{\delta}(k)$ to potential using equation 2.18 and then compute $\hat{f}(k)$ using equation 2.19. (iv) Perform the inverse Fourier transform back to real space and perturb a lattice of dark matter and gas particles and assign them velocities following equations 2.16 and 2.17. The power spectrum generated, $\mathcal{P}(k)$, should be normalized for the present epoch using σ_8:

$$\sigma_8^2 = \frac{1}{(2\pi)^3} \int \mathcal{P}(k) W^2(k) k^2 dk \tag{2.20}$$

where $W(k)$ is the Fourier transform of a top-hat spherical window of radius $R = 8h^{-1}$ Mpc. The power spectrum also needs to be scaled back to the starting epoch of the simulation using the growth function $D(a)$ (which is also a function of the Hubble constant H, mass and vacuum content Ω_m and Ω_Λ for ΛCDM cosmology, cf. Peebles (1993)).

The initial conditions in this work are generated following the above steps using codes developed by T.Quinn and also by G. Stinson (*private communications*). The latter has a parallel version of generating $\hat{\delta}(k)$ and that was used for the high resolution (2×512^3) IC. Table 2.1 lists the simulations used in this study. The cosmological parameters are ($\Omega_m, \Omega_\Lambda, \Omega_b, h, \sigma_8$, n) = (0.279, 0.721, 0.0462, 0.701, 0.769, 1.0), consistent with the WMAP 5-year results (Komatsu et al., 2009). The first three simulations in the table share the exact same initial condition but have different subgrid models for metal cooling and diffusion. The particle masses are $m_g = 2.4 \times 10^7 M_\odot$ for gas particles

Name	Size (Mpc)	N_p	Metal Cooling	Diffusion	z_{final}
mcd_40_256	40.0	2×256^3	Yes	Yes	0
nmc_40_256	40.0	2×256^3	No	Yes	0
nmd_40_256	40.0	2×256^3	Yes	No	0
mcd_45_256	45.6	2×256^3	Yes	Yes	0
mcd_45_512	45.6	2×512^3	Yes	Yes	2

Table 2.1 List of Simulations

and $m_d = 1.2 \times 10^8 M_\odot$ for dark matter. When discussing the effects of metal cooling and diffusion, we will usually refer to the first simulation (mcd_40_256) "the reference run". The last two simulations were designed for a convergence study. To make the same ICs with different resolution, the potential grid $\hat{\phi}(k)$ was generated for the high-res (512^3) simulation (i.e. $k_{max} = 2\pi/L \times 512$), and then any modes with $k > 2\pi/L \times 256$ were filtered to make the lower-res 256^3 simulation. The high resolution case has particle masses $m_d = 3.6 \times 10^7 M_\odot$ and $m_g = 4.5 \times 10^6 M_\odot$. All the simulations have the same star formation, metal production and SN feedback models described below. The simulations were run to redshift zero, except for the "mcd_45_512"case which was stopped at z = 2 due to CPU limitations.

2.5 Summary

In this chapter I described the methods we used to perform hydrodynamical simulations in order to study the IGM enrichment. This work uses the Tree+SPH code gasoline (Wadsley et al., 2004), in which gravity is computed using the Hierarchical Tree method and the hydrodynamical equations are solved using the Smoothed Particle Hydrodynamics. Star formation, metal production and supernova feedback are treated according to Stinson et al. (2006), where the McKee & Ostriker (1977) blastwave model is adopted to model the unresolved SN superbubble, and galactic outflows were generated as a natural consequence of the SN feedback. To capture the turbulent mixing of energy and metals in the IGM, the code incorporates a Smagorinsky (Smagorinsky, 1963) turbulent diffusion model. In this model diffusion is applied only on unresolved, subgrid scales and the diffusion coefficient is proportional to the shear motions of the flow. The initial conditions of the simulations were generated using the Zel'dovich approximation (Zel'Dovich, 1970). The resolutions of the simulations are comparable to other studies (e.g., Wiersma et al., 2009) of the IGM enrichment.

This study consists of five simulations. The first set (three simulations) is designed to investigate the effects of metal cooling and turbulent diffusion, and the second set is performed for a convergence study.

Bibliography

Barnes, J., & Hut, P. 1986, Nature, 324, 446

Couchman, H. M. P. 1991, ApJ, 368, L23

Efstathiou, G., Davis, M., White, S. D. M., & Frenk, C. S. 1985, ApJS, 57, 241

Frenk, C. S., et al. 1999, ApJ, 525, 554

Governato, F., Willman, B., Mayer, L., Brooks, A., Stinson, G., Valenzuela, O., Wadsley, J., & Quinn, T. 2007, MNRAS, 374, 1479

Greif, T., Glover, S., Bromm, V., Klessen, R. 2009, MNRAS, 392, 1381

Kennicutt, R. C., Jr., Tamblyn, P., & Congdon, C. E. 1994, ApJ, 435, 22

Kennicutt, R. C., Jr. 1998, ApJ, 498, 541

Komatsu, E., et al. 2009, ApJS, 180, 330

Kroupa, P., Tout, C. A., & Gilmore, G. 1993, MNRAS, 262, 545

Mashchenko, S., Wadsley, J., & Couchman, H. M. P. 2008, Science, 319, 174

McKee, C. F., & Ostriker, J. P. 1977, ApJ, 218, 148

Monaghan, J. J. 1992, ARA&A, 30, 543

Peebles, P. J. E., *Principles of Physical Cosmology*, Princeton University Press, 1993

Pope, S. B. 2000, *Turbulent Flows*, by Stephen B. Pope, pp. 806. ISBN 0521591252. Cambridge, UK: Cambridge University Press, September 2000

Raiteri, C. M., Villata, M., & Navarro, J. F. 1996, A&A, 315, 105

Seljak, U., & Zaldarriaga, M. 1996, ApJ, 469, 437

Sirko, E. 2005, ApJ, 634, 728

Smagorinky, J., 1963, Monthly Weather Rev., 91, 3, 99

Stinson, G., Seth, A., Katz, N., Wadsley, J., Governato, F., & Quinn, T. 2006, MNRAS, 373, 1074

Thielemann, F.-K., Nomoto, K., & Yokoi, K. 1986, A&A, 158, 17

Wadsley, J. W., Stadel, J., & Quinn, T. 2004, New Astronomy, 9, 137

Wadsley, J., Veeravalli, G., & Couchman, H., 2008, MNRAS, 387, 427

Weidemann, V. 1987, A&A, 188, 74

Wiersma, R. P. C., Schaye, J., Theuns, T., Dalla Vecchia, C., & Tornatore, L. 2009, MNRAS, 399, 574

Woosley, S. E., & Weaver, T. A. 1995, ApJS, 101, 181

Zel'Dovich, Y. B. 1970, A&A, 5, 84

Chapter 3

Metal Cooling under a Photoionizing Background

Before the first stars form, the chemical composition of the Universe is predominately H and He, with only slight amounts of D and Li. Metals produced in stars are ejected into the surrounding gas within galaxies, and into the intergalactic medium via stellar winds, supernova explosions and large-scale galactic winds. Although only present in trace amounts compared to H and He, metals may significantly increase the radiative cooling rates of the gas, and thus affect subsequent gas accretion onto galaxies and star formation. Despite its importance, metal cooling is usually either neglected or modeled incorrectly in most cosmological simulations due to the complicated reaction network it involves to model metal cooling directly. A common approach is to calculate the metal cooling rate under the assumption of collisional ionization equilibrium (CIE), where the effect of photo-ionization is ignored or assumed to be small. Since the IGM is surely exposed to an ultraviolet background, this assumption results in a large overestimation of cooling rates. In this Chapter, I introduce a new method to model metal cooling self-consistently with a evolving UV background using photoionization package CLOUDY (Ferland et al., 1998). This cooling is implemented into the GASOLINE (Wadsley et al., 2004) code, together with a non-equilibrium calculation of the primordial species evolution. The chapter begins with a discussion of the ionization and radiative cooling/heating of the primordial species in Section 3.1. In Section 3.2, I describe how the metal cooling model is constructed. I also investigate the effect of UV radiation, cosmic rays, and the dependence of metal cooling rate on various parameters such as metallicity, density and temperature. In Section 3.5 I describe how the cooling model is implemented into the GASOLINE code.

3.1 Radiative Cooling of Primordial Species

Hydrogen and Helium are the dominant elements of the IGM. Without metal enrichment, they are also the major coolants. Under a ionizing radiation background generated by quasars and stars in galaxies, neutral hydrogen and helium can be photoionized or collisionally ionized. The ions can also recombine with free electrons. The evolution of primordial ions (H^0, H^+, He^0, He^+, He^{++}) is governed by the following differential equations:

$$\frac{dn_{H^0}}{dt} = \alpha_{H^+} n_{H^+} n_e - \gamma_{eH^0} n_e n_{H^0} - \gamma^{ph}_{H^0} n_{H^0} \tag{3.1}$$

$$\frac{dn_{He^0}}{dt} = (\alpha_{He^+} + \alpha_d) n_{He^+} n_e - \gamma_{eHe^0} n_{He^0} n_e - \gamma^{ph}_{He^0} n_{He^0} \tag{3.2}$$

$$\begin{aligned}\frac{dn_{He^+}}{dt} &= \gamma_{eHe^0} n_{He^0} n_e + \gamma^{ph}_{He^0} n_{He^0} + \alpha_{He^{++}} n_{He^{++}} n_e \\ &-(\alpha_{He^+} + \alpha_d) n_{He^+} n_e - \gamma_{eHe^+} n_{He^+} n_e - \gamma^{ph}_{He^+} n_{He^+}\end{aligned} \tag{3.3}$$

where γ_{eX}, γ^{ph}_X and α_X are the collisional ionization, photoionization and regular recombination coefficients for atom/ion X, respectively. Specifically, $\gamma^{ph}_X = \int^{\infty}_{\nu_0(X)} (4\pi J_\nu)/(h\nu)\sigma_\nu(X) d\nu$, where $\nu_0(X)$ is the threshold frequency for ion/atom X, J_ν is the mean intensity of incidental radiation, and $\sigma_\nu(X)$ is the ionization cross section. And α_d is the dielectric recombination rate for singly ionized helium. The collisional ionization and recombination coefficient are functions of temperature only, and the photoionization coefficient also depends on the wavelength. In this work we adopted the coefficients for collisional ionization and recombination from Abel et al. (1997) and references therein. The photoionization rate was computed according to the incident UV radiation using photoionization package CLOUDY (Ferland et al., 1998), to be consistent with our metal cooling model (cf. Section 3.5). For the IGM, in most cases the recombination timescale is much shorter than the Hubble timescale, so the ion species are close to ionization equilibrium. In this case the time derivative terms of the above equations are approximately zero. In the absence of a photo-ionizing background, the equilibrium is between collisional ionization and recombination. It is called collisional ionization equilibrium

(CIE).

After reionization of the Universe, the intergalactic gas is optically thin to photons, largely ionized and in ionization equilibrium. The ionization and recombination of primordial species (H^0, H^+, He^0, He^+, He^{++}) provide cooling and heating to the IGM. The processes include:

- Collisional excitation line cooling. Free electrons can collide with H or He atoms and cause the bound electron(s) within the atoms to excite to a higher-energy state. When these atom de-excite, they emit photons. Thus kinetic energy of the free electrons is converted to radiation and cools the plasma. The cooling rates can be written as

$$\Lambda^{line} = \zeta_{H^0}(T) n_e n_{H^0} + \zeta_{He^0}(T) n_e n_{He^0} + \zeta_{He^+}(T) n_e n_{He^+}, \tag{3.4}$$

  where $\zeta_{H^0}(T)$, $\zeta_{He^0}(T)$ and $\zeta_{He^+}(T)$ is the sum of the energy loss over all possible line transitions i→j. For each transition the energy loss is the product of collisional excitation strength per unit volume per unit time, times the energy difference between the two states. For simple primordial ions, these coefficients are usually only a function of temperature. We adopted rates $\zeta_{H^0}(T)$, $\zeta_{He^0}(T)$ and $\zeta_{He^+}(T)$ from Cen (1992).

- Collisional ionization cooling. When H^0, He^0 and He^+ are collisionally ionized, the kinetic energies of the ionizing free electrons are reduced by the amount equal to the ionization potential of the H and He species.

$$\Lambda^{coll} = E^p_{H^0} \gamma_{eH^0}(T) n_e n_{H^0} + E^p_{He^0} \gamma_{eHe^0}(T) n_e n_{He^0} + \\ E^p_{He^+} \Gamma_{eHe^+}(T) n_e n_{He^+} \tag{3.5}$$

Here E^p is the energy loss per ionization which is equal to the ionization potential energy (e.g., for H^0 it is 13.6 eV), and γ_{eX} are the ionization coefficients for ion X defined in the ionization equations and they are functions of temperature only.

- Recombination cooling. The kinetic energy of a free electron is radiated away when it recombines with an ion.

$$\Lambda^{rec} = \epsilon_{H^+}(T)\alpha_{H^+}(T)n_e n_{H^+} + \epsilon_{He^+}(T)\alpha_{He^+}(T)n_e n_{He^+} + \epsilon_{He^{++}}(T)\alpha_{He^{++}}(T)n_e n_{He^{++}} + \epsilon_d \alpha_d(T) n_e n_{He^+} \quad (3.6)$$

Here ϵ_X are energy losses in each recombination of ion X which are functions of temperature. The energy loss of dielectric recombination, ϵ_d is a constant (Cen, 1992). In the implementation of primordial cooling in GASOLINE, we used the convention in which the internal energy of the gas does not include ionization potential energies, thus the cooling rate is not equivalent to the radiative energy loss. For example, in the recombination process $H^+ + e^- \rightarrow H^0 + \gamma$, if the electron initially has temperature T_e, after recombination the total energy loss is $3/2kT_e$ (k is the Boltzmann constant). Part of this energy (equal to the hydrogen potential energy – 13.6 eV) is radiated away. According to our convention, this radiative loss is not subtracted, and the energy loss in cooling is $\Delta E = 3/2kT_e - 13.6\text{eV}$. For the same reason, in collisional ionization, the ionization potential energy *is* subtracted from the gas.

- Bremsstrahlung cooling (free-free emission). Free electrons can be accerlerated by the ions and emit photons thus cooling the gas.

$$\Lambda^{ff} = \xi_{Z=1}(T)n_e(n_{H^+} + n_{He^+}) + \xi_{Z=2}(T)n_e n_{He^{++}} \tag{3.7}$$

The cooling coefficient ξ depends on the temperature and electric charge Z. In this work, we adopted the formula from Cen (1992) to compute the coefficients.

- Compton heating/cooling. Compton scattering of the photons from the cosmic microwave background (CMB) on free electrons can causes an increase or decrease in energy of the photons and therefore provide cooling or heating to the gas. The total cooling/heating due to the CMB is

$$\Lambda_{Comp} = 5.4 \times 10^{-36}(1+z)^4 n_e(T - T_{\mathrm{CMB}}) \text{ erg s}^{-1} \text{ cm}^3, \tag{3.8}$$

where T_{CMB} = 2.735(1+z) K (Bromm et al., 2002).

- Photoionization heating. Photoioniation produces free electrons with kinetic energy $h(\nu - \nu_0)$, where $h\nu_0$ is the ionization potential energy of the atoms/ions. It thus converts radiation to kinetic energy and heats the plasma. The total heating rate can be written as:

$$\Gamma_{H,He} = \eta_{H^0} n_{H^0} + \eta_{He^0} n_{He^0} + \eta_{He^+} n_{He^+}, \tag{3.9}$$

where $\eta_X = \int_{\nu_0(X)}^{\infty} (4\pi J_\nu)/(h\nu) h(\nu - \nu_0(X))\sigma_\nu(X) d\nu$. $\nu_0(X)$, J_ν and $\sigma_\nu(X)$ have the same definition as in the expression of photoionization rates γ_X^{ph}. Similar to γ_X^{ph}, the photoionization heating rate η_X in this work was also computed using CLOUDY (Ferland et al., 1998) in order to be consistent with our metal cooling model (cf. Section 3.5).

The solid line in Figure 3.1 shows the primordial cooling rates normalized by n_H^2 as a function of temperature under the CIE assumption, where n_H is the total hydrogen number density. The rates were calculated using the photoionization package CLOUDY(Ferland et al., 1998) which assumes ionization equilibrium (described in detail in Section 3.2). The solid line in Figure 3.2 shows the fraction of neutral hydrogen n_{H^0}/n_H as a function of temperature assuming collisional ionization equilibrium. Below $\sim 10^4$K, H and He are mostly neutral and there are almost no free electrons and the radiative cooling rate is very low, although in the non equilibrium case traces of free electrons may exist and they are important for the formation of molecular hydrogen H_2, which would dominate cooling in this temperature regime. In computing this curve, however, the cooling due to H_2 is excluded, because CLOUDY gives unrealistically high H_2 cooling rates by assuming ionization equilibrium (detailed discussion in Section 3.4). Hydrogen starts to be ionized at $T > 10^4$K, which generates free electrons to excite the neutral hydrogen and collisional excitation cooling dominates (the first peak in Figure 3.1). When hydrogen is fully ionized around 10^5K, because of the decrease in neutral hydrogen (Figure 3.2), the cooling rate decreases. Similarly, collisional excitations of He^0 and He^+ generate the second peak in Figure 3.1. Helium is fully ionized beyond 10^6K, and collisional excitation cooling decreases. In this temperature range $(10^4 - 10^6\mathrm{K})$, recombination and collisional ionization cooling also exist, but are much smaller (at least an order of magnitude less). Beyond 10^6 K, free-free emission dominates.

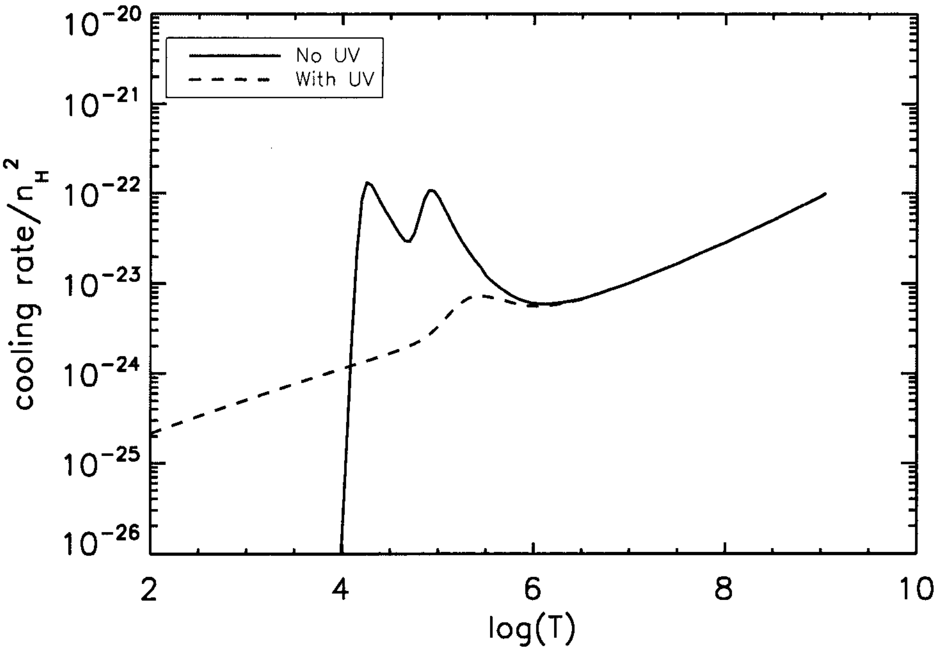

Figure 3.1 Cooling rates normalized by n_H^2 (in erg s^{-1} cm^3) for primordial gas with total hydrogen number density $n_H = 10^{-5}$ cm^{-3}. *Solid line*: cooling rates for gas in the collisional ionization equilibrium (CIE). *Dashed line*: cooling rates under a z=3 extragalactic radiation background adapted from Haardt & Madau (2005). The rates were calculated using the photoionization package CLOUDY (Ferland et al., 1998, , described in Section 3.2) with assumption of ionization equilibrium. Compton cooling is not included in this calculation.

3.1.1 Effect of Photo-ionization on Primordial Cooling and Heating

Photo-ionization changes the ionization balance of the H and He species and alters the cooling rates in a non-linear way. The effect is especially large for low density gas. The dashed line in Figure 3.1 shows the cooling rate normalized by n_H^2 under a UV radiation background (Haardt & Madau, 2005). And the dashed line in Figure 3.2 shows the fraction of neutral hydrogen for the gas under the same UV background. With photo-ionization, the number of free

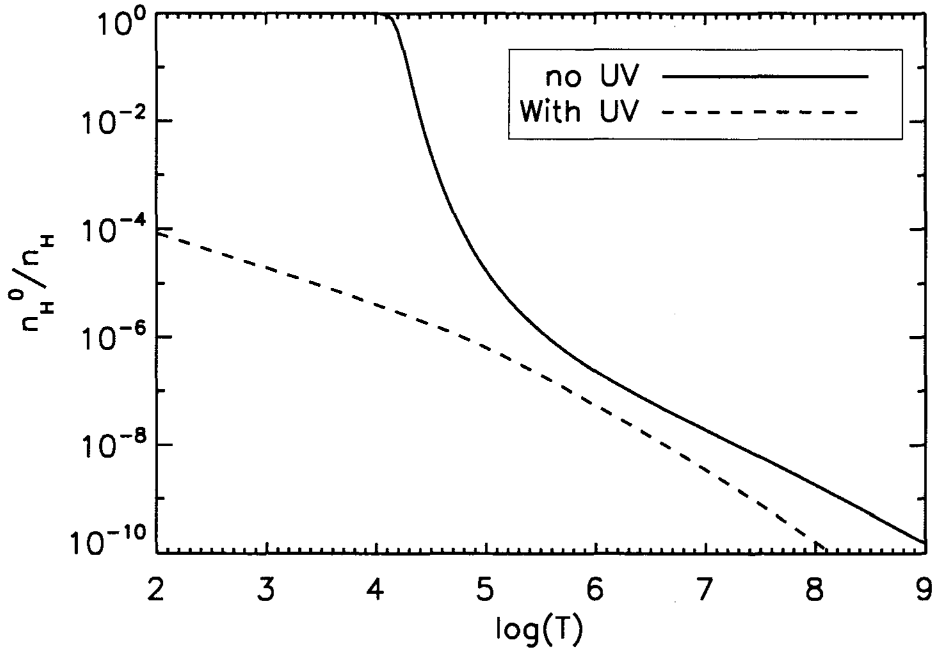

Figure 3.2 Number fraction of neutral hydrogen, n_{H^0}/n_H as a function of gas temperature. *Solid line*: neutral hydrogen fraction for gas without UV radiation. *Dashed line*: neutral hydrogen fraction for gas exposed to a z=3 extragalactic radiation background (Haardt & Madau, 2005). The fractions were computed using CLOUDY (Ferland et al., 1998) with the assumption of ionization equilibrium.

electrons increases dramatically at $T < 10^4$K. For example, at T = 1000 K, $n_H = 10^{-5}$ cm^{-3} the electron number density increases from $n_e \sim 10^{-9}$ cm^{-3} to $\sim 10^{-5}$cm^{-3}. As a result, cooling due to recombination dominates in this region. On the other hand, the collisional excitation peaks from H and He are suppressed, because photoionization decreases the fractions of H^0, He^0 and He^+, as shown in Figure 3.2. For example, at $T = 3 \times 10^4$K, the fraction of H^0/H decreases from 2.5×10^{-3} for pure collisional ionization to 1.7×10^{-6} when photo-ionization is included. The importance of radiation in primordial cooling has been recognized (e.g., Black, 1981; Efstathiou, 1992; Katz et al.,

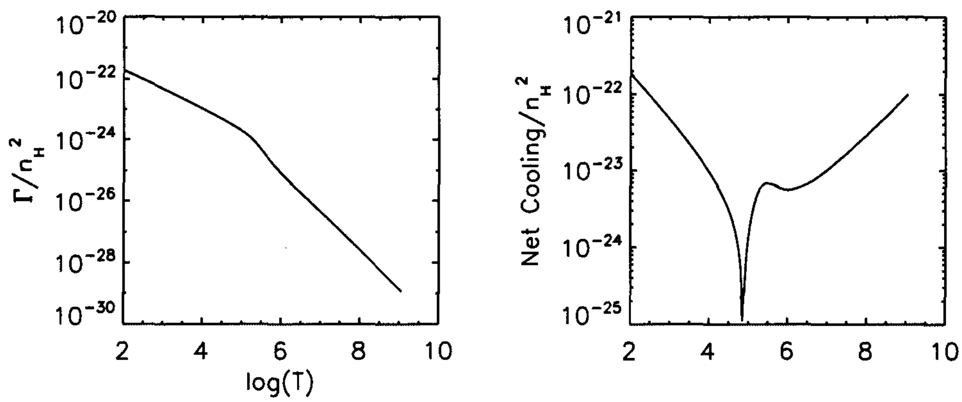

Figure 3.3 *Left Panel*: Heating rates normalized by n_H^2 (in erg s^{-1} cm^3) for primordial gas with total hydrogen number density $n_H = 10^{-5}$ cm^{-3}, under a z=3 extragalactic radiation background adapted from Haardt & Madau (2005). *Right Panel*: Net cooling rates (computed as the absolute value of cooling rates minus heating rates) for the same gas. Heating dominates for gas with T $< 10^5$ K. The rates were calculated using the photoionization package CLOUDY (Ferland et al., 1998, , described in Section 3.2) with assumption of ionization equilibrium.

1996) and included in many cosmological simulations (e.g., Aguirre et al., 2005; Cen & Ostriker, 2006; Oppenheimer & Davé, 2006). However, as will be discussed in detail in Section 3.2, UV radiation also has similar effects on metal cooling rates, but these effects are usually ignored in simulations. Thus simulations probably overestimate the cooling rates.

Photo-ionization of H^0, He^+ and He^{++} is also a major heating source of the gas. The left panel figure 3.3 gives the heating rate of the same gas under the z = 3 UV background. The right panel gives the net cooling rates (i.e. the absolute of cooling - heating rates) as a function of temperature. In this example, heating dominates below 10^5 K. UV heating is able to prevent gas accreting onto small galactic halos ($\lesssim 10^9$ $M_\odot$) and thus has a significant impact on the formation of dwarf galaxies.

3.1.2 Non-equilibrium Primordial Cooling

Under a UV radiation background, the IGM is mostly in ionization equilibrium. But before the reionization of the Universe, without UV radiation, the recombination time for the low density IGM can be longer than the Hubble time thus the ions are not in ionization equilibrium. So, for the formation of the first stars and for reionization, non-equilibirum effects can be important. For example, cooling due to molecular hydrogen, H_2, is essential for the formation of first generation stars. Without any metals, the formation of H_2 relies on the gas phase reactions (see e.g., Abel et al., 1997) that are sensitive to the abundance of free electrons. Under ionization equilibrium the fraction of electrons below 10^4 K is small (as seen in the above section) and there is not enough H_2. Non-equilibrium ionization of H and He under certain situations (e.g., when gas is shock heated from structure formation) can provide excess free electrons thus making it possible to form enough molecular hydrogen to cool the gas (Abel et al., 1997). Although first structure formation is beyond the scope of this work, and the formation and cooling of molecular hydrogen is not included, when implementing primordial gas cooling, the Equations 3.1, 3.2, 3.3 are directly integrated to evolve the ion fractions and the cooling rates (rf. Section 3.5). Thus the cooling model is able to capture the non-equilibrium effects and follow the gas thermal evolution more accurately, especially before and during reionization.

Figure 3.4 gives an example of how gas cooling is affected when non-equilibrium ionization is included. A thin slab of primordial gas with density $n_H \sim 2 \times 10^{-4}\text{cm}^{-3}$ is initially cold ($\sim$ 130 K) and neutral. The black curves show how the gas temperature and the neutral hydrogen fraction n_{H^0}/n_{tot}

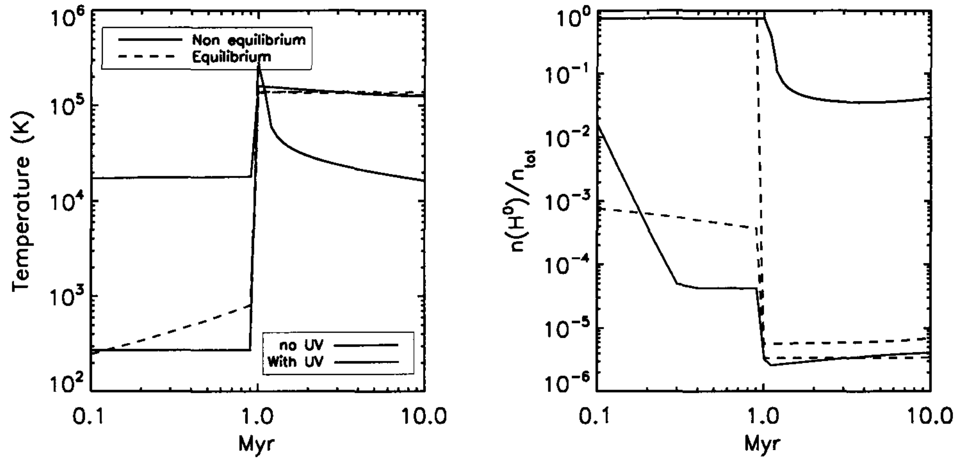

Figure 3.4 An example of non-equilibrium effects on gas cooling. *Black lines*: The gas is initially cold (~130 K) and neutral, with primordial composition $n_{H^0}/n_{tot} = 0.764$ and $n_{He^0}/n_{tot} = 0.236$. The density of the gas is about the cosmic mean density at z = 10, $n_H \sim 2 \times 10^{-4}\mathrm{cm}^{-3}$. From t = 0.9-1 Myr, a large amount of energy is injected to the gas and assuming ionization equilibrium, it will bring the gas to T = 1.4×10^5 K. *Blue lines*: The gas properties and the energy injection are the same as described above, but the gas is exposed to a z = 3 UV background (Haardt & Madau, 2005) turned on at t = 0. *Left panel*: the evolution of gas temperature. *Right panel*: evolution of the number fraction of neutral hydrogenn_{H^0}/n_{tot}. The solid and dashed lines indicate non-equilibrium and equilibrium calculation, respectively. Both calculations are performed using the cooling model implemented in GASOLINE.

evolve when a large amount of energy is injected to the gas for short periods of time from t = 0.9 Myr to 1 Myr. Assuming the gas is instantly ionized and reaches equilibrium, the energy injection would heat the gas to equilibrium temperature $T_{eq} = 1.4 \times 10^5$ K. The gas would then gradually cool down via collisional excitation of H and He. While the equilibrium calculation (dashed line) does show the trend described above, the non-equilibrium (solid line) gives a different picture. In this case, atoms are not ionized instantly. Take hydrogen as an example (right panel of Figure 3.4) Just after the injection of the energy, most hydrogen is still neutral. Thus the number density of the gas is about half of the one in the equilibrium case. Consequently for the same amount of energy injection the temperature is doubled. And because the neutral fraction is high, gas cooling via collisional excitation is much larger than in the equilibrium case, and thus the gas cools off rapidly to much below the equilibrium temperature. This example illustrates that an accurate treatment of non-equilibrium effects is important, especially within radiative shocks and when there is no UV radiation. For comparison, the blue lines in Figure 3.4 shows the case in which the same gas is under a UV background (z=3 from Haardt & Madau (2005)) that is turned on at t =0, then receives the same energy injection from t=0.9-1 Myr. With photoionization, hydrogen is already largely ionized before the injection of energy, so the effect of non-equilibirum after the energy injection is small (blue curves after 1 Myr). Therefore as far as the IGM *after* the reionization is concerned, non-equilibrium ionization does not affect the IGM temperature significantly. The situation is however different during reionization. This is shown by the blue curves at 0.1-1 Myr. In the non-equilibrium case, after the UV is turned on, the neutral hydrogen is gradually ionized and does not decrease instantly (as in the equilibrium case). Because the photoionization heating is dependent on the number density of neutral hydrogen (cf. Equation 3.9), the slower decrease of n_{H^0} allows the gas to receive more heating and reach a higher temperature (blue solid line of the left panel). In contrast, in the equilibrium calculation, the fraction of neutral hydrogen drops instantly and the photoionization heating is small (blue dashed line in the left panel). In principle the non-equilibrium could also affect metal cooling. A fully consistent metal cooling model would incorporate the non-equilirium ionization of metal ions. This has been done in modeling the shocks in the interstellar medium (Allen et al., 2008) or galactic halos (e.g., Indebetouw & Shull, 2004). However, it is still too computationally expensive to follow the non-equibrium chemistry (which involves hundreds of ionization equations with reaction timescales much shorter than the dynamical timescale) in full cosmological simulations. Also, as far as the intermediate or low redshift IGM ($z < 5$) is concerned, if it is subject to a UV ionization background and is not shocked, ionization equilibrium is a good approximation for most gas. In future work we will implement non-equilibirum ionization for the most abundant metals such as oxygen, carbon and silicon. How non-equilibirum ionization affects the metal absorption lines (such as O VI) will be investigated.

3.2 Metal Cooling

Although metals are much less abundant compared to H and He, metal ions usually have much lower collisional excitation potentials than primordial species. Thus collisionally excited metal ions can dominate the radiative cooling of the IGM in a large temperature range by their resonance line transitions (Sutherland & Dopita, 1993). Metal cooling thus affects the gas temperature, the ionization states of the observable metal species and ultimately the dynamics. It was not generally feasible to calculate metal cooling rates during a cosmological simulation. Instead, cooling rates have usually been calculated using sophisticated photo-ionization softwares and then tabulated and interpolated during the simulations as in Oppenheimer & Davé (2006), Wiersma et al. (2009a) and Choi & Nagamine (2009). In general, metal cooling rates were determined from the density, temperature, metallicity of the gas and the radiation background. While the IGM and ISM are exposed to UV radiation, metal cooling rates (e.g., Sutherland & Dopita, 1993; Gnat & Sternberg, 2007) were usually calculated assuming collisional ionization equilibrium (CIE), which is only valid when the radiation background is absent. These cooling rates were widely used in cosmological simulations (Oppenheimer & Davé, 2006; Choi & Nagamine, 2009). In this section I will explore how metal cooling depends on the UV radiation metallicity and density in the temperature range of 100 K to 10^9K. I will also discuss the effect of cosmic rays (CR) on metal cooling and the cooling due to H_2 at $T < 10^4$K.

The cooling and heating rates due to metals under the ultraviolet(UV) radiation background were calculated using the photoionization code CLOUDY (version 07.02, Ferland et al. (1998)). CLOUDY allows the user to define the incident ionization spectrum and the properties of gas such as chemical abundances, temperature, density and geometry, and calculates the ionization states, cooling and heating rates. CLOUDY assumes that metals are in ionization equilibrium, a good approximation when extragalactic UV radiation is present. In general for a slab of optically thin gas, the metal cooling rate is a function of temperature, density, metallicity and redshift, i.e., $\Lambda_{metal} = \Lambda_{metal}(\rho, T, Z, z)$. Metal cooling depends on redshift because the radiation background evolves with time. Under CIE, there is no dependence on redshift, and because most of the cooling processes are two-body collisional, the rates also scale well with density, thus $\Lambda_{metal}/n^2 = \Lambda_{metal}(T, Z)/n^2$, where n is the number density of the gas. With UV photoionization the dependence of cooling on all parameters is more complicated.

3.2.1 CLOUDY Inputs

1. UV background. The extragalactic UV background consists of radiation from active galactic nuclei (AGN) and stars in galaxies, and generally varies its functional form in space and time. However, with current data of QSO absorbing systems, it is difficult to constraint the spatial distribution of the UV radiation. With the development of efficient UV spectrographs such as the Cosmic Origins Spectrograph (COS, Shull (2009)), we may be able to probe the spatial variation. But for the current study, as commonly adopted by other works, a uniform UV background is assumed. The spectrum of a UV radiation is usually calculated by modeling the reprocessing of incident photons in the IGM using 1D radiative transfer. In this study, we obtained the UV spectrum by extracting the CLOUDY (07.02) built-in extragalactic UV background calculated by Haardt & Madau (2005). It includes radiation from both quasars and galaxies. The radiation field is a function of wavelength and redshift, and it turns on at redshift $z = 8.9$ (i.e., it assumes reionization happens at this redshift) and evolves with redshift to $z=0$. The same UV background was also adopted to calculate the cooling due to primordial species.

2. Metal abundance. Although our simulations trace the formation of alpha elements and iron separately (cf. Chapter 2), our metal cooling assumed relative solar abundances for simplicity. We used the most up-to-date CLOUDY solar composition, which contains the first thirty elements in the periodic table. The solar composition data were compiled from Grevesse & Sauval (1998); Holweger (2001); Allende Prieto et al. (2001, 2002) (see Table 9 of the CLOUDY version 07.02 documentation for details). Deviation from solar composition does exist in galaxies because massive stars explode (as Type II SN) earlier than intermediate mass stars do (as Type Ia SN). Thus at early stages there would be an α element enhancement in galaxies. A more accurate treatment of metal cooling would require following the injection of each element and computing the cooling due to each element separately. However, given that the yield of metal elements still has large uncertainties (See, e.g., Wiersma et al., 2009, and references therein), we assume solar composition as a first order approximation, and focus on the effect of the UV background.

3. Density and Temperature. While typical studies of IGM cooling usually focus on $T > 10^4$K, we choose to include the low temperature range down to 100 K which can occur in dense environments where galaxies form, or in the IGM that is cooled by adiabatic expansion, although the latter is generally not enriched. It is also interesting to explore the effect of UV on metal cooling in the low temperature range. A physical number density range of $n_H = 10^{-9}$ cm^{-3} - 10^3cm^{-3} covers the density variation of the IGM. The lower limit, 10^{-9} cm^{-3}, is about 0.01 of the cosmic mean density today. It was assumed the gas is optically thin to the ionizing background for all wavelengths, which is valid for the IGM. The cooling table is stopped at 10^3 cm^{-3} because beyond this point the optical depth of the ISM gas is large and the gas is self-shielded from the hydrogen-ionizing photons. Thus the optically-thin approximation is no longer valid and a proper radiative transfer calculation is necessary to model the ISM. Because current cosmological simulations still lack the resolution to incorporate ISM modeling directly, the cooling table in this work is stopped where the gas is turning optically thick.

3.2.2 Effect of UV on Metal Cooling and Heating

Figure 3.5 shows cooling rates normalized by n_H^2 as a function of temperature at various metallicities. The black curves show the total cooling rates with a z=3 radiation background, while the red curves show the CIE metal cooling (no UV background) plus the cooling of H and He under the UV background (i.e. the dashed-line curve in Figure 3.1), a model often adopted in cosmological simulations (e.g., Choi & Nagamine, 2009; Oppenheimer & Davé, 2006). With or without UV, the presence of metals can increase cooling rates by up to several orders of magnitude. In the temperature range $10^4 < T < 10^8$ K, radiation ionizes the plasma and reduces the number of ions that can be collisionally excited therefore decreasing the cooling rates significantly (e.g., about an order of magnitude at 10^5 K in Figure 3.5). The cooling peak also shifts from 10^5K to 10^6K due to the change of ionization states of the metal elements. From 100 K to 10^4 K, the UV background increases the number density of free electrons (n_e) hence enhancing forbidden line cooling from low ionization species such as C I, C II, Si I, Si II and O I. Forbidden line cooling is the dominant cooling process in enriched IGM at low temperatures. At low densities ($n_H \lesssim 10^{-4}cm^{-3}$), photo-ionization also creates some higher-ionized species with strong magnetic dipole transitions (e.g. Ne V and Ne VI). These ions can cool the plasma more efficiently, producing a local cooling peak around 10^3K (Figure 3.5). However with an increase in density these ions disappear and the major coolants are the less ionized species mentioned, consistent with ISM cooling models (e.g. Wolfire et al., 2003). Overall, the radiation background increases the metal cooling rate substantially between 100 K and 10^4 K over CIE. Figure 3.5 shows unequivocally that simply adding the

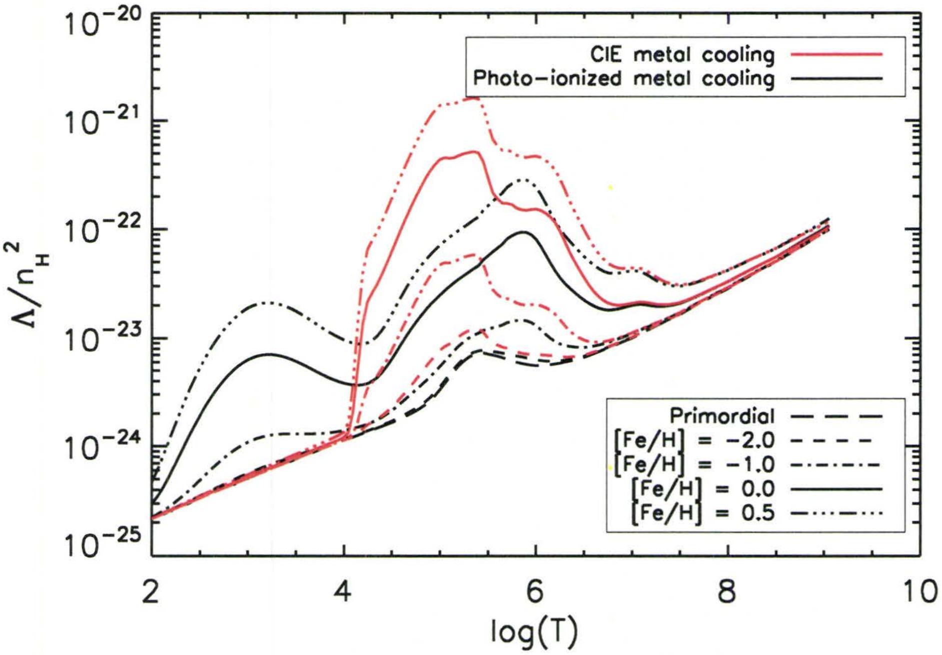

Figure 3.5 Cooling rates normalized by n_H^2 (in erg s^{-1} cm^3) with metallicities [Fe/H] = -2.0, -1.0, 0 and 0.5. The gas has density $n_H = 10^{-5}$ cm^{-3}. *Black*: total cooling rates (include H, He and metals) under the z=3 extragalactic radiation background from Haardt & Madau (2005); *Red*: Sum of cooling rates of H and He under the same radiation background, and metal cooling rates, calculated without UV background

CIE model of metal cooling on the primordial cooling rates results in dramatic over or under-estimation of the cooling rates, depending on the temperature.

Beside primordial ions, UV radiation can also ionize metal species such as O, C, Ne, Si, N, S, and Fe and provide heating to the gas. Figure 3.6 shows that the heating rates increases with increased metallicity, especially at higher temperature. For example, there is about an order of magnitude difference between the heating rate of primordial gas and gas with solar abundance at 10^5 K. This difference is significant and also needs to be included into the radiative cooling/heating model.

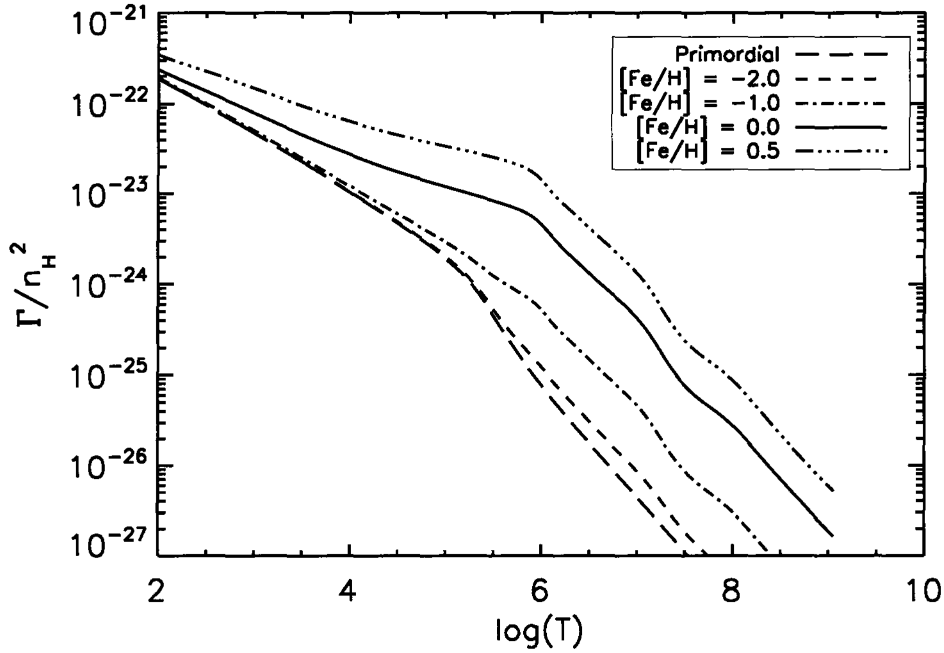

Figure 3.6 Heating rates normalized by n_H^2 (in erg s^{-1} cm^3) with metallicities [Fe/H] = -2.0, -1.0, 0 and 0.5. The gas has density $n_H = 10^{-5}$ cm^{-3}. The curves are computed under the z=3 extragalactic radiation background from Haardt & Madau (2005); The primordial heating rate (long dashed line) is identical to the left panel of Figure 3.3.

3.2.3 Metal Cooling/Heating Dependence on Density

Figure 3.7 shows the dependence of cooling rates on density under different UV backgrounds. The upper panel shows the cooling rate at T = 10^5 K, a temperature close to the peak of collisional excitation cooling. The plotted cooling rates are due to metals only and are normalized by n_H^2. In the CIE case (solild line), cooling scales with n_H^2 as expected. With UV radiation, however, at low density the cooling rate is orders of magnitude lower, and it follows a much steeper relation with density. It scales with n_H^2 only when $n_H > 10^{-2} cm^{-3}$. At the low density region, photoionization substantially affects the abundance of cooling ions. For example, at $n_H = 10^{-5}\text{cm}^{-3}$ and T = 10,000 K, the major coolants are the carbon ions (CIII, CIV). But under a z = 3 UV background, carbon is totally ionized at this density and the major coolant is the O IV ion, which has a much higher excitation potential , thus leading to a lower cooling rate. The scaling also depends sensitively on the UV background. This non linear dependence on density is also prominent at lower temperatures (lower panel of Figure 3.7, where T = 1000 K). At this temperature, there is no simple scaling relation over the whole density range. The same is also true for metal heating rates. Thus in the construction of the metal cooling model, density is kept as an independent parameter. Although the rates were tabulated as Γ/n_H^2 for convenience, there is no scaling with n_H^2.

3.2.4 Metal Cooling and Heating Dependence on Metallicity

The metal cooling process is dominated by collisional excitation, thus is proportional to $n_e n_{ion}$, where n_e is the electron density and n_{ion} is the total density of metal ions. Since the abundance of metals is small compared to primordial ions, the ionization of metals does not contribute significantly to n_e. Thus, we expect that the metal cooling rates scale linearly with the total amount of metal ions and hence the metallicity. Similar arguments can also be applied to metal heating, which is proportional to $n_\gamma n_{ion}$. Because the number density of ionizing photons, n_γ, is independent of metals, the heating rates scale linearly with the metallicity.

Figure 3.8 shows an example in which the metal cooling and heating rates do scale linearly with metallicity as expected. This is true for all tem-

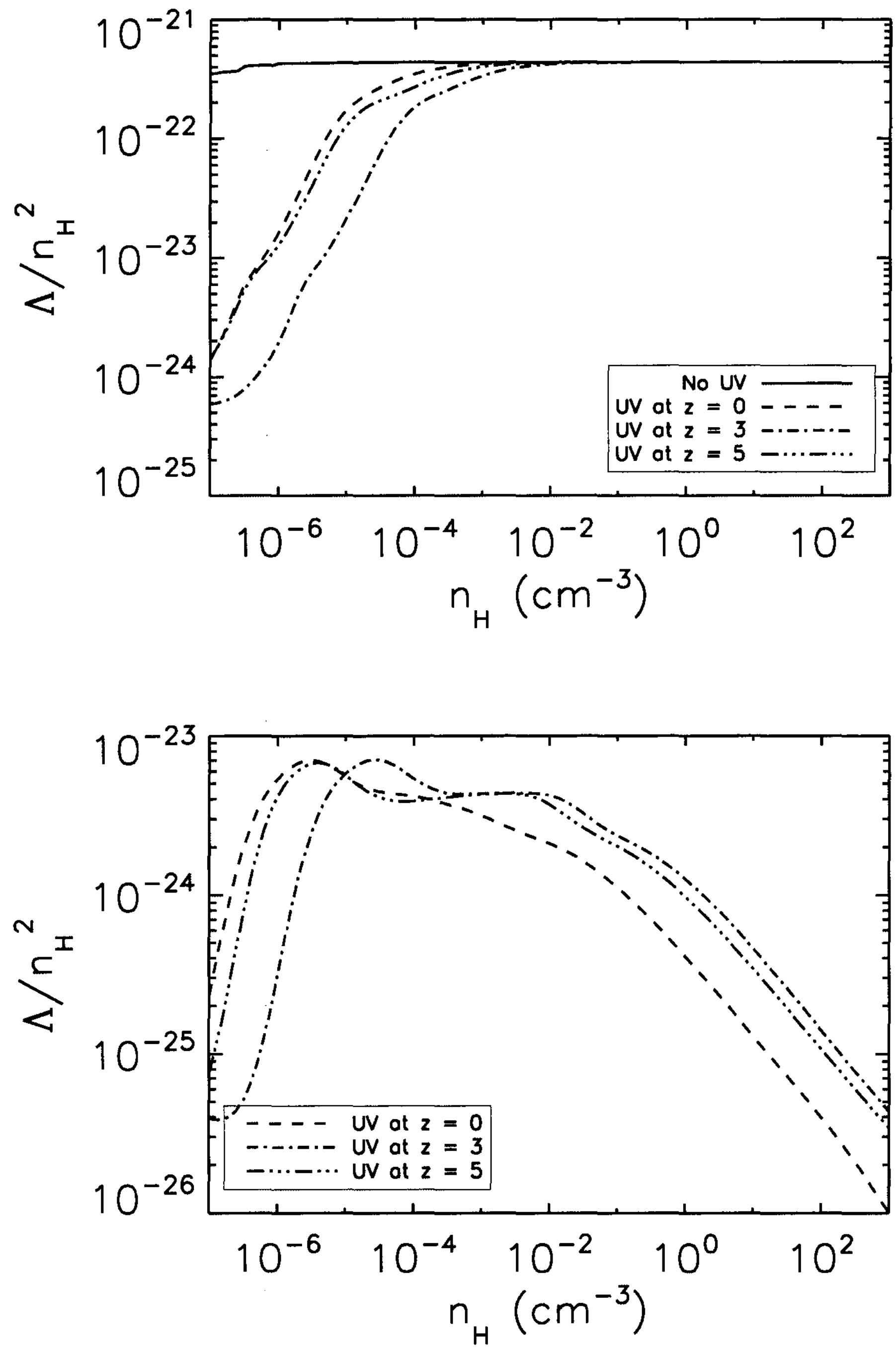

Figure 3.7 Cooling rates normalized by n_H^2 (in erg s^{-1} cm^3) as a function of n_H. The gas has solar metallicity. Upper panel: T = 10^5K. Bottom panel: T = 10^3 K.

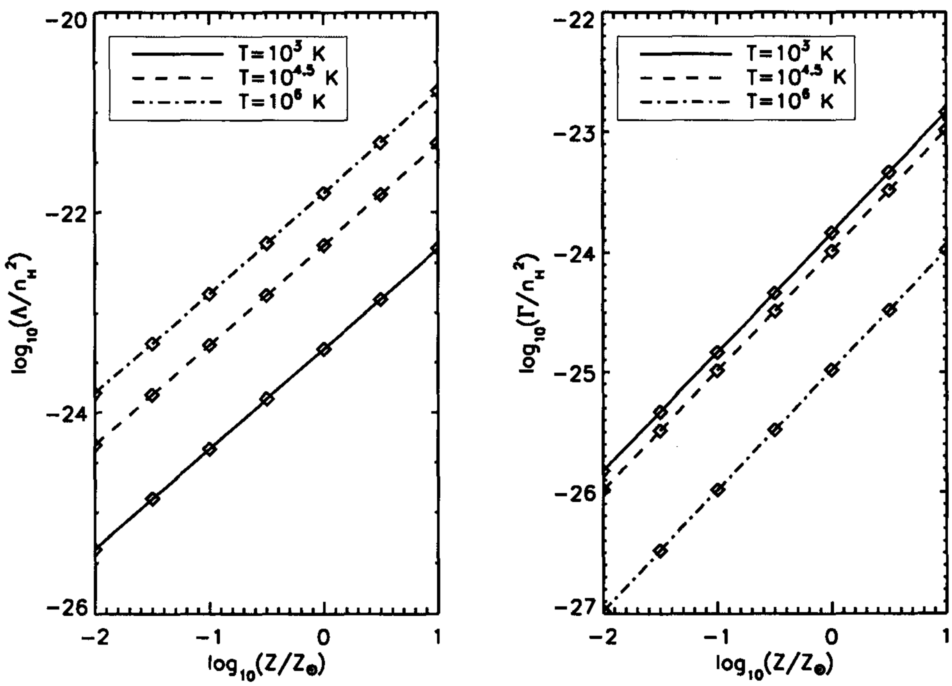

Figure 3.8 Metal cooling and heating rates normalized by n_H^2 (in erg s^{-1} cm^3) as a function of metallicity at temperatures 10^3K (solid line), $10^{4.5}$K (dashed line) and 10^6K (dot-dashed line). The gas has density $n_H = 10^{-3}$ cm^{-3} and it is under the z = 3 UV background adopted from Haardt & Madau (2005). Both cooling and heating scale linearly with metallicity.

peratures and densities investigated in this work. The χ^2 errors of linear fits are generally below 10^{-4}. This scaling relation simplified our cooling model by reducing the number of parameters to three. The general expression for metal cooling and heating can be written as:

$$\Lambda_{metal}(T, \rho, z, Z) = \frac{Z}{Z_\odot}\Lambda_{metal,\odot}(T, \rho, z) \tag{3.10}$$

and

$$\Gamma_{metal}(T, \rho, z, Z) = \frac{Z}{Z_\odot}\Gamma_{metal,\odot}(T, \rho, z) \tag{3.11}$$

The functions $\Lambda_{metal,\odot}(T, \rho, z)$ and $\Gamma_{metal,\odot}(T, \rho, z)$ cannot be further simplified since the dependence on temperature, redshift and density are more complicated, as seen in the above sections.

3.3 Effect of the Cosmic Ray Background on Heating and Cooling

Cosmic rays (CRs) are energetic, relativistic nuclei and electrons that can provide heating and ionization of gas (Osterbrock & Ferland, 2006). It is believed that they are generated in AGN, supernovae or shock waves of structure formation, and it was found (e.g., Sijacki et al., 2008) that CRs can have a significant impact on galaxy cluster formation and the intracluster medium. At the low temperature and high density end, where gas is self-shielded from UV, CRs are also the main source of ionization (Osterbrock & Ferland, 2006). However, neither the formation of galaxy clusters or the chemistry of the ISM is the focus of this work. In this section I focus on studying how CRs change the ionization, heating and cooling of the IGM *under UV radiation*, using the CLOUDY package.

Figure 3.9 shows the effect of the cosmic ray background on the cooling of the IGM. Here, a galactic-level cosmic ray background is applied to gas with number density $n_H = 10^{-3}$ cm^{-3}. At $T < 10^4$ K, without UV radiation (dot-dashed line), the ionization of H and He by cosmic rays provides free electrons (e.g., n_e $10^{-2} n_H$ at 100 K). This allows metal atoms or low metal ions (C I, Si II, etc.) to cool the gas via forbidden line cooling. The effect is however negligible when UV radiation is turned on (the solid line and thick dashed

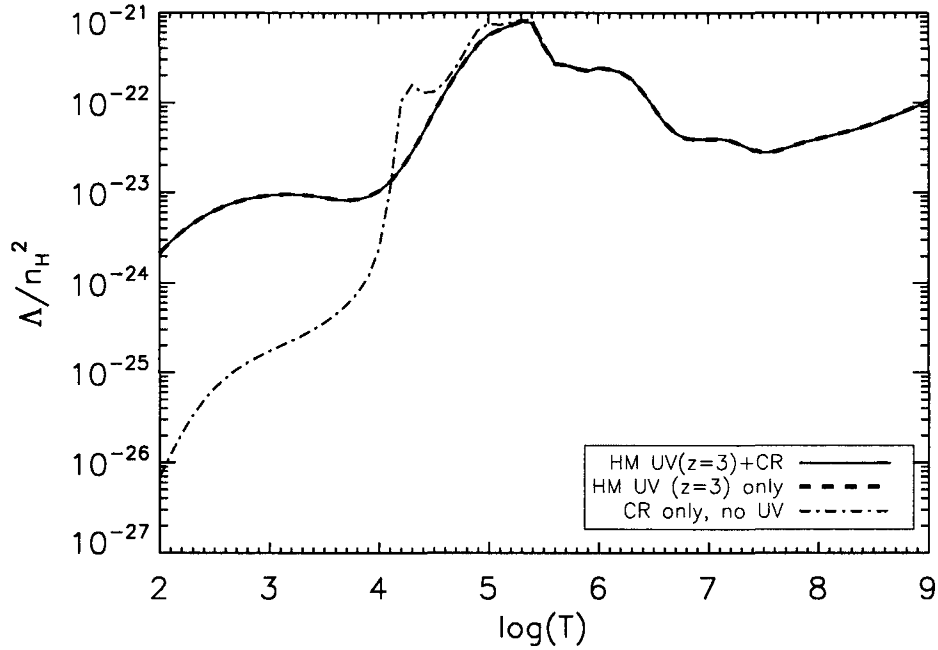

Figure 3.9 Total cooling rates normalized by n_H^2 (in erg s^{-1} cm^3) as a function of temperature. The gas has density $n_H = 10^{-3}$ cm^{-3}. *Solid line*: the gas is under a the z = 3 UV background adopted from Haardt & Madau (2005) and a cosmic ray background of the Galactic level (H^0 ionization rate of 2.5×10^{-17} s^{-1} and H_2 ionization rate of 5.0×10^{-17} s^{-1}, cf. CLOUDY c07.02.01 documentation). *Thick dashed line*: cooling rates for gas under z = 3 UV background but not CR background. *Dot-dashed line*: cooling rates under galactic CR background only, no photoionization.

line of Figure 3.9 are identical), because photoionization provides significantly more free electrons ($n_e\, n_H$). The UV radiation shown in Figure 3.9 is relatively strong (at z = 3), but even for a weak background (e.g., z > 7) the above conclusion remains true. Beyond $10^{5.5}$ K, collisional excitation dominates and the effect of either UV or cosmic rays is small. Thus as long as the gas is under UV radiation (as is the case for the IGM), the effect of cosmic rays on cooling are negligible.

Ionization of H I, He I and He II does provide heating to the gas, as

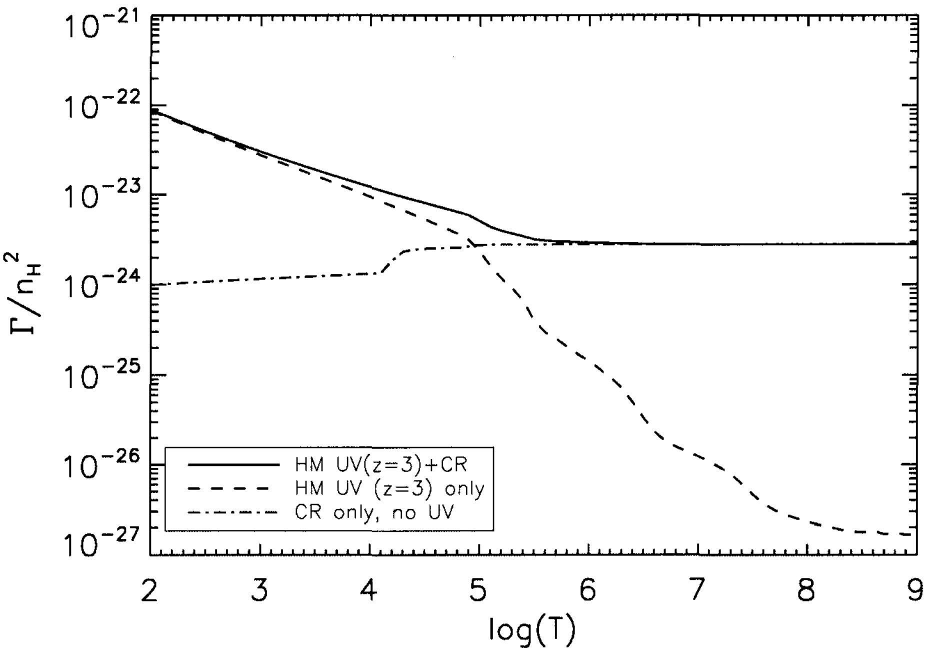

Figure 3.10 *Black curves*: total heating rates normalized by n_H^2 (in erg s^{-1} cm^3) as a function of temperature. The gas has density $n_H = 10^{-3}$ cm^{-3}. The notation is same as in Figure 3.9.

shown in the dot-dashed line of Figure 3.10. In the case shown in Figure 3.10, at $T \lesssim 10^5$ K, heating due to photoionization still dominates. At higher temperature, since the UV heating declines rapidly while cosmic ray heating increases slightly with temperature, CRs largely dominates the heating rate at this region. However at this temperature gas cooling is much higher than heating, hence the net cooling rate is not significantly changed (cf. black curves in Figure 3.11). This is not the case for gas with lower densities if CR remains the same level. For example, at $n_H < 10^{-5}$ cm^{-3}, if the CR background is still at the galactic level, heating from CR may dominate cooling over the whole temperature range and thus the net cooling curve can be significantly affected. However, because CRs are generated from supernova, shock waves or AGN, it

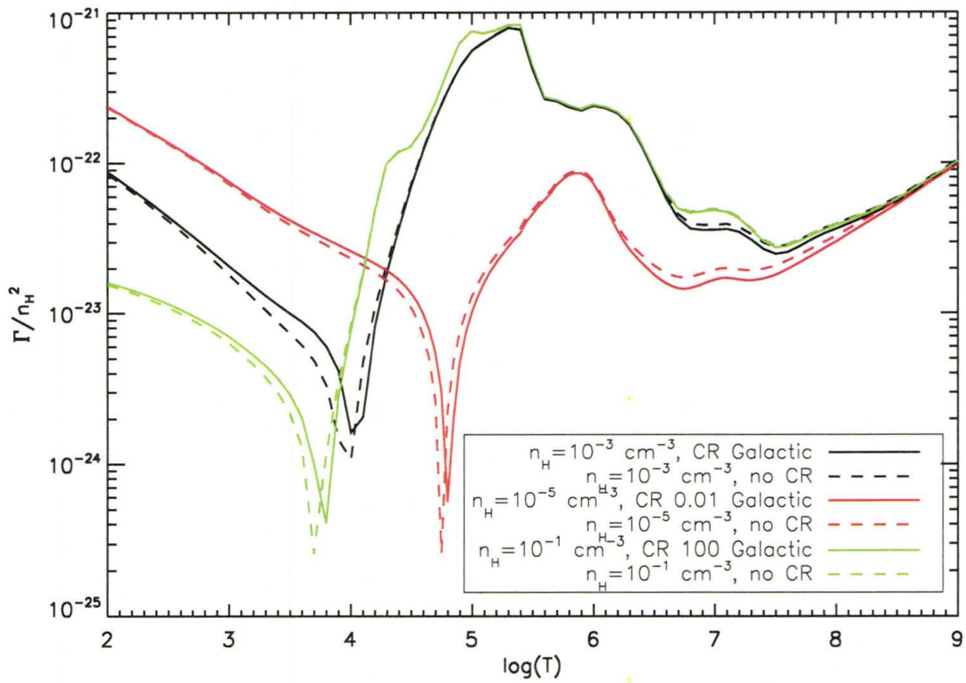

Figure 3.11 Net cooling rates normalized by n_H^2 (in erg s^{-1} cm^3) as a function of temperature. The gas has density $n_H = 10^{-1}$ cm^{-3} (green), 10^{-3} cm^{-3} (black) and 10^{-5} cm^{-3} (red) and correspondingly, the CR background intensity is 10^2 galactic level, galactic level and 10^{-2} galactic level. The solid lines are the net cooling with CR and the dashed lines are the net cooling without CR.

is a reasonable to assume a positive correlation between the CR level and the gas density. It was found that if the CR background intensity is scaled linearly with gas density, then the heating and cooling due to CR is unchanged. In this case, the net cooling rates with CR do not deviate significantly from the ones without CR, as shown in Figure 3.11. Similar results were also obtained for gas with different metallicities and under radiation backgrounds at different redshifts.

Note that in Figure 3.11 the CR background level is normalized at the galactic level for gas with $n_H = 10^{-3}$ cm^{-3}, a density that is much lower than typical in the interstellar medium. The effect of CR is even smaller if the same level of CR is applied to high densities, assuming there is still UV radiation on the gas. However for gas within galactic disks, it is uncertain if CR can be scaled linearly with density, or if it can be treated as a uniform background. To realistically model the gas within the galactic disk and/or the ISM, one would have to consider the distribution of local stellar UV radiation and the generation and distribution of cosmic rays (e.g. Sijacki et al., 2008). This is beyond the scope of the current study.

The results in this section show that for IGM under extragalactic UV, the impact of CR in gas radiative heating/cooling is small. Since the cooling model in this work is designed for the IGM and resolving the ISM is beyond the ability of current cosmological simulations, the cosmic ray background is *not* included.

3.4 Molecular Hydrogen Cooling at Low Temperature

As discussed in Section 3.1.2, at temperatures lower than 10^4 K and without strong UV radiation, cooling due to molecular hydrogen is important, especially for the formation of the first stars. The formation and destruction of H_2, however, follows non-equilibrium processes (Abel et al., 1997). Because CLOUDY always assumes ionization equilibrium, whereas the true time to reach equilibrium is long, it assumes high H_2 and thus overestimates the cooling rate in the low temperature region.

Figure 3.12 shows an example. Without a UV background, the fraction

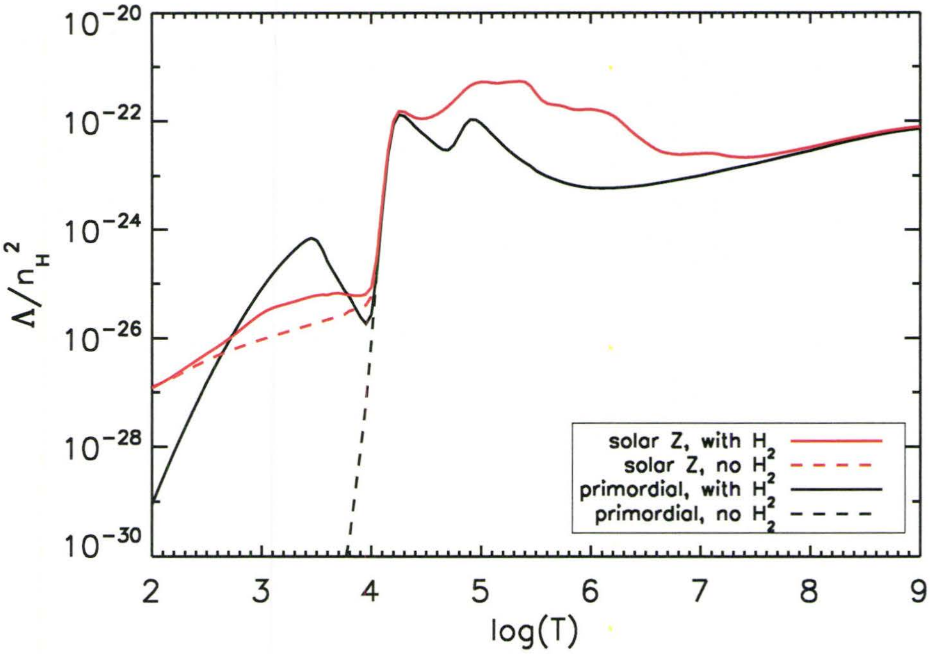

Figure 3.12 Cooling rates normalized by n_H^2 (in erg s^{-1} cm^3) as a function of temperature computed in CLOUDY. The gas has density $n_H = 10^{-3}$ cm^{-3}, and is under a very weak UV background (z = 8.9 UV spectrum divided by 10^8 in intensity). The solid lines indicate gas cooling with H_2 and the dashed lines indicate cooling without H_2. CLOUDY assumes ionization equilibrium for molecular hydrogen and overestimated its cooling rate when there is little UV radiation.

of molecular hydrogen n_{H_2}/n_H reaches about 4×10^{-3} for the primordial gas, and the cooling rate due to H_2 dominates for $T < 10^4$K. This cooling rate is even larger than the one with solar metal abundance (if comparing the black solid curve with the red one in Figure 3.12), which is different than the results obtained from integrating the non-equilibrum equations of H_2 evolution (e.g., Smith et al., 2008). Therefore, We have turned off H_2 calculation in CLOUDY using the "no H_2 molecule" command. Note that for a fully consistent model of the molecular region, it is necessary to follow the H_2 formation and destruction, together with cooling due to dust grains, and this is not included in the current cooling model since neither first object formation nor the ISM is the focus of this study.

3.5 Implementation into the GASOLINE code

To implement the metal cooling and heating into GASOLINE, the radiative cooling was separated into three components:

$$\Lambda_{rad} = \Lambda_{H,He} + \Lambda_{metal} + \Lambda_{Comp} \tag{3.12}$$

where $\Lambda_{H,He}$ is the cooling due to primordial species (H^0, H^+, He^0, He^+ and He^{++}), including cooling processes due to collisional excitation, collisional ionization, free-free emission and recombination. i.e., $\Lambda H, He = \Lambda^{line} + \Lambda^{coll} + \Lambda^{ff} + \Lambda^{rec}$. Λ_{metal} is the rate due to metals, dominated by collisional metal-line cooling. And Λ_{Comp} is the Compton cooling/heating given in Equation 3.8. Heating rates can be similarly written in primordial, metal and Compton parts and most heating is from photoionization. For the primordial gas the ionization, cooling and heating rates were calculated directly from Equations 3.1, 3.2 and 3.3, and Equations 3.4-3.9) with rates matching Abel et al. (1997). This enables the simulations to capture the non-equilibrium cooling of primordial species. In order to be consistent with metal cooling calculations, which use the Haardt & Madau (2005) UV background, I obtain the ionization and heating rates (i.e., $\gamma^{ph}(X)$ and $\eta(X)$) under the same UVB using the "punch gammas" command for the primordial species, and use these values in the time-dependent calculation. The CMB Compton cooling/heating is also directly calculated using Eq. 3.8.

The helium abundance generally increases with metallicity. We adapted the relation from Jimenez et al. (2003) to estimate the helium mass abundance Y as it varies with metallicity. For metal mass abundance $Z < 0.1$ (which is about 10 times the solar metallicity), we assume $Y = Y_p + (\Delta Y/\Delta Z)Z$, where $Y_p = 0.236$ is the helium abundance for primordial gas, and $\Delta Y/\Delta Z = 2.1$ is the ratio of helium mass to metal mass produced in stars. If the metal mass abundance exceeds 0.1 ($\sim 10Z_{\odot}$), Y is linearly decreased so that when $Z = 1.0$ (100% metals), $Y = 0$. In practice, the gas metallicity in our simulations is always less than 0.1.

For metal cooling and heating, the rates were calculated using CLOUDY with cosmic rays and molecular hydrogen turned off as described in previous sections. According to Equation 3.10 and 3.11, only rates for gas with solar abundance were calculated. We obtained the metal cooling/heating rates by subtracting the primordial cooling/heating rates from the total rates of 30 elements (with abundance described in Section 3.2), including H and He, assuming that metals do not contribute significantly to the electron density of the gas. The rates are then tabulated in log(T) (from 100 K to 10^9K with Δlog(T)= 0.05), log(n_H) (where n_H from 10^{-9} cm^{-3} to 10^3 cm^{-3} with Δlog(n_H) 0.1), and redshift z ($8.9 \leq z \leq 0$ with grid size 0.1). Cooling and heating rates were interpolated separately in log space in the simulation. The RMS of relative interpolation errors for cooling and heating is less than 1 percent. At $z > 8.9$ cooling was calculated with effectively no UV background and the UV heating is zero. For gas with density or temperature exceeding the boundaries ($T <$ 100K or $n_H <$ 10^{-9} cm^{-3} or $>$ 10^3 cm^{-3}), the rates (normalized by n_H^2) at the boundaries were used for simplicity.

In GASOLINE, we solve a set of four equations including 3.1-3.2 and an energy equation,

$$\frac{dE}{dt} = \Gamma_{ext} - \Lambda_{net}, \tag{3.13}$$

where Γ_{ext} is the heating or cooling by external processes such as the adiabatic cooling by the expansion of the universe and shock heating in structure formation, etc. $\Lambda_{net} = \Lambda_{rad} - \Gamma_{rad}$ is the net cooling due to radiative processes. The thermal energy can be converted to temperature by $T = E/(2/3n_{tot}k)$, where k is the Boltzmann constant and n_{tot} is the total gas number density and is calculated by:

$$n_{tot} = n_e + n_H + n_{He} + \rho_Z/\mu \text{ where} \tag{3.14}$$

$$n_e = n_{H^+} + n_{He^+} + 2n_{He^{++}} \tag{3.15}$$

here ρ_Z is the mass density of metals and μ is the mean "molecular" weight of gas with solar composition metals. Note that the small electron contribution from metals (<1% effect) is neglected in equation 3.15 for simplicity. The temperature is then used in calculating all of the ionization/recombination rates. In practice, because GASOLINE is a particle code, all the number density quantities or cooling/heating rates per volume were converted to numbers per baryon or cooling/heating rates per baryon in the code.

Numerically, the equation set is called "stiff" which means that the dependent variables change according to the independent variables on two or several very different scales. In the case discussed here, the ionization timescales are usually much shorter than the energy update timescale. Thus simply integrating the equations using an explicit integrator will easily lead to a

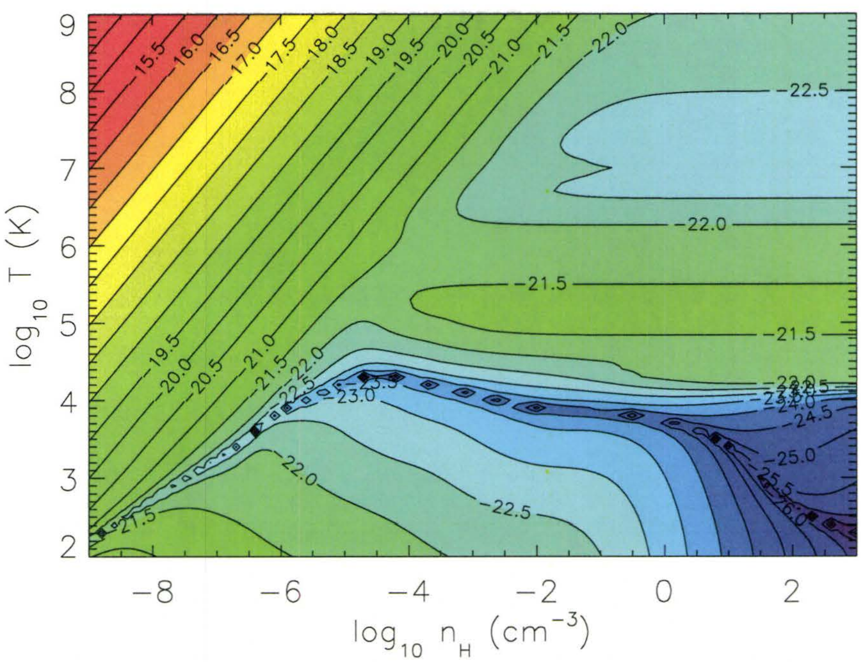

Figure 3.13 Contours of the log of the normalized net cooling rates (i.e., $\log_{10}(|\Lambda - \Gamma|/n_H^2$, in units of erg s^{-1} cm^3) in the density-temperature plane. The contours ranges from -28 to -14 with spacing $\Delta = 0.5$. The rainbow color scale indicates $\log_{10}(|\Lambda - \Gamma|)$ from the highest value (-14) in red, to the lowest (-28) in black. The gas has solar metallicity $Z_\odot = 0.0127$, is exposed to a z = 3 Haardt & Madau (2005) UV background and has Compton cooling rate also at z = 3. Cooling due to the adiabatic expansion of the Universe at z = 3 is also included.

stability problem, unless we follow the shortest timescale, which will make the simulation computationally expensive. We adopted a stiff solver from Press et al. (2007) which uses a semi-implicit extrapolation method to integrate these equations.

Figure 3.13 shows the contours of the net cooling rate ($\log_{10}(|\Lambda - \Gamma|/n_H^2)$ in the density-temperature phase diagram. Besides the radiative cooling/heating, Compton cooling from the CMB and the adiabatic cooling due to the expansion of the Universe are also included. The gas has a uniform solar metallicity and is exposed to a z=3 Haardt & Madau (2005) UV background. There are three regions in this diagram: the upper-left part where the gas is cooled by adiabatic expansion, the bottom part where the gas is heated by photoionization, and the right part where the gas is cooled by radiative cooling (metal and primordial cooling). Equilibrium is reached between adiabatic cooling and UV heating for the low density gas with $n_H \lesssim 10^{-5}\text{cm}^{-3}$, and between radiative cooling and UV heating for higher density gas. Due to the inclusion of metals, the equilibrium temperature of the gas with higher density (especially for $n_H \gtrsim 1\text{cm}^{-3}$ can be significantly below 10^4K, which will affect star formation in the ISM. Radiative cooling is the most important for warm-hot gas (between $\sim 10^5 - 10^7$K), and this will have impact on how halo gas accretes onto galaxies and how hot winds generated from stellar feedback cool. We will discuss these aspects in later chapters (cf. Chapter 4). We will show also in Chapter 4 that most gas in our simulations is distributed in the phase diagram along the equilibrium curve, except for the gas that is shock heated during accretion or heated by feedback energy (cf. Figure 4.16).

3.6 Summary

In this Chapter we investigated the radiative cooling and heating for enriched gas in the IGM. In particular, we examined the effects of photoionization from extragalactic UV radiation, non-equilibirum ionization and cosmic rays. We found that photoionization due to UV significantly alters the metal cooling rates at all temperatures from 100 K to 10^9 K. Above 10^4 K it decreases the cooling rate and shifts the cooling peak to a higher temperature, while below 10^4 K the UV increases the metal cooling rates, mainly due to the increase in free electrons. Non-equilibrium ionization of primordial species is important for gas that is not exposed to UV radiation or during reionization. Because the IGM is subject to UV radiation for most of the time, the non-equilibrium effects are small. However we still integrate the ionization equation for primordial species directly to capture any of these effects. We also found that the overall effects of cosmic rays on IGM heating/cooling is not significant if the gas is subject to photoionization and if the magnitude of the CR background scales with gas density.

Using photoionization package CLOUDY, we constructed a self-consistent metal cooling model in which the cooling and heating rate were calculated assuming the gas has solar composition and is exposed to a uniform extragalactic UV radiation (Haardt & Madau, 2005). The metal cooling rates are functions of density, temperature and redshift, but scale linearly with metallicity. The metal cooling table is interpolated in the GASOLINE code. Although many uncertainties exist regarding the ISM modeling such as stellar UV, cosmic rays and non-equilibrium ionization for metals, these effects are generally not important as far as the IGM is concerned. By including the extragalactic UV radiation into the metal cooling, we have constructed a more realistic heating/cooling model suitable for the IGM than prior works (e.g., Oppenheimer & Davé, 2006).

Bibliography

Abel, T., Anninos, P., Zhang, Y., & Norman, M. L. 1997, New Astronomy, 2, 181

Aguirre, A., Schaye, J., Hernquist, L., Kay, S., Springel, V., & Theuns, T. 2005, ApJL, 620, L13

Allen, M. G., Groves, B. A., Dopita, M. A., Sutherland, R. S., & Kewley, L. J. 2008, ApJS, 178, 20

Allende Prieto, C., Lambert, D. L., & Asplund, M. 2001, ApJL, 556, L63

Allende Prieto, C., Lambert, D. L., & Asplund, M. 2002, ApJL, 573, L137

Black, J. H. 1981, MNRAS, 197, 553

Bromm, V., Coppi, P. S., & Larson, R. B. 2002, ApJ, 564, 23

Cen, R. 1992, ApJS, 78, 341

Cen, R., & Ostriker, J. P. 2006, ApJ, 650, 560

Choi, J.-H., & Nagamine, K. 2009, MNRAS, 393, 1595

Efstathiou, G. 1992, MNRAS, 256, 43P

Ferland, G. J., Korista, K. T., Verner, D. A., Ferguson, J. W., Kingdon, J. B., & Verner, E. M. 1998, PASP, 110, 761

Gnat, O., & Sternberg, A. 2007, ApJS, 168, 213

Grevesse, N., & Sauval, A. J. 1998, Space Science Reviews, 85, 161

Haardt F., Madau P. 2005, *unpublished*

Holweger, H. 2001, Joint SOHO/ACE workshop "Solar and Galactic Composition", 598, 23

Indebetouw, R., & Shull, J. M. 2004, ApJ, 605, 205

Jimenez, R., Flynn, C., MacDonald, J., & Gibson, B. K. 2003, Science, 299, 1552

Katz, N., Weinberg, D. H., & Hernquist, L. 1996, ApJS, 105, 19

Oppenheimer, B. D., & Davé, R. 2006, MNRAS, 373, 1265

Osterbrock & D. E., Ferland, G. J. *Astrophysics of Gaseous Nebulae and Active Galactic Nuclei*, Second Edition, University Science Books, 2006

Press, W. H., Teukolsky, S. A., Vetterling, W. T., & Flannery, B. P., *Numerical Recipes: The Art of Scientific Computing*, Third Edition, Cambridge University Press, 2007

Shull, J. M. 2009, American Institute of Physics Conference Series, 1135, 301

Sijacki, D., Pfrommer, C., Springel, V., & Enßlin, T. A. 2008, MNRAS, 387, 1403

Smith, B., Sigurdsson, S., & Abel, T. 2008, MNRAS, 385, 1443

Sutherland, R. S., & Dopita, M. A. 1993, ApJS, 88, 253

Wiersma, R. P. C., Schaye, J., & Smith, B. D. 2009, MNRAS, 393, 99

Wiersma, R. P. C., Schaye, J., Theuns, T., Dalla Vecchia, C., & Tornatore, L. 2009, MNRAS, 399, 574

Wolfire, M. G., McKee, C. F., Hollenbach, D., & Tielens, A. G. G. M. 2003, ApJ, 587, 278

Chapter 4

Results and Discussion

4.1 Global Properties of the Simulation

Figure 4.1 depicts the formation and evolution of large scale structures in the simulations. Under gravitational force, initial density perturbations grow and collapse into sheet and filamentary structures. At the intersections of these structures, galactic halos form. Initially, gas follows the dark matter flows, accretes onto galaxies and fuels star formation. Stellar feedback then injects energy and momentum into the gas and distributes metals. As halo masses grow through mergers and accretion, gas is heated as it accretes and its temperature is significantly increased (as shown in the $z = 0$ and $z = 1$ temperature panels). On the other hand, gas in the under-dense regions is cooled adiabatically due to the expansion of the universe. The metallicity distribution is clumpy (right column of Figure 4.1), indicating that enriched wind material does not travel far into the IGM, and there is a clear correlation between gas metallicity and density. As discussed in Chapter 1, stellar feedback and galactic winds do not only distribute metals into the surroundings but also regulate the star formation rate (SFR) in galaxies and gas accretion. Most accreted, high density gas is self-shielded from UV radiation and is thus neutral. The evolution of the total neutral hydrogen density, $\Omega_{\rm HI}$, (in units of the critical density) reflects the evolution of this accreted gas. On the other hand, neutral gas in the IGM is a small fraction of the total and can be traced by the Lyα forest. Before embarking on a detailed, quantitative examination of the metal distribution and evolution in the IGM, it is worth establishing the basic properties of the simulated volume with respect to the star formation history (SFH), the Lyman-α forest and the evolution of total neutral hydrogen. These properties directly reflect the effectiveness of the feedback processes and allow the galaxy model to be calibrated with respect to observations.

4.1.1 Star Formation History

4.1.1.1 Global Star Formation History

Figure 4.2 shows the evolution of global star formation rate (SFR) as a function of redshift. The simulations record the formation time of the stars, and the global SFR, at a certain time t, is computed by adding up the total stellar mass formed in a time range $t - \Delta t/2 - -t + \Delta t/2$ (where $\Delta t = 5 \times 10^7$ years), and dividing it by the volume of the simulation box (i.e. (40 Mpc)^3 or (45 Mpc)^3). The observational data with error bars were adapted from Hopkins (2004) and scaled to the same IMF and cosmology as used in our simulations. The figure shows that all simulations with moderate resolution (with or without metal cooling and diffusion) produce an SFH that is consistent with observations for $z \gtrsim 0.5$. The peak of star formation lies around $z \sim 2$ for all simulations. It has been claimed by other authors that explicit galactic wind models are necessary

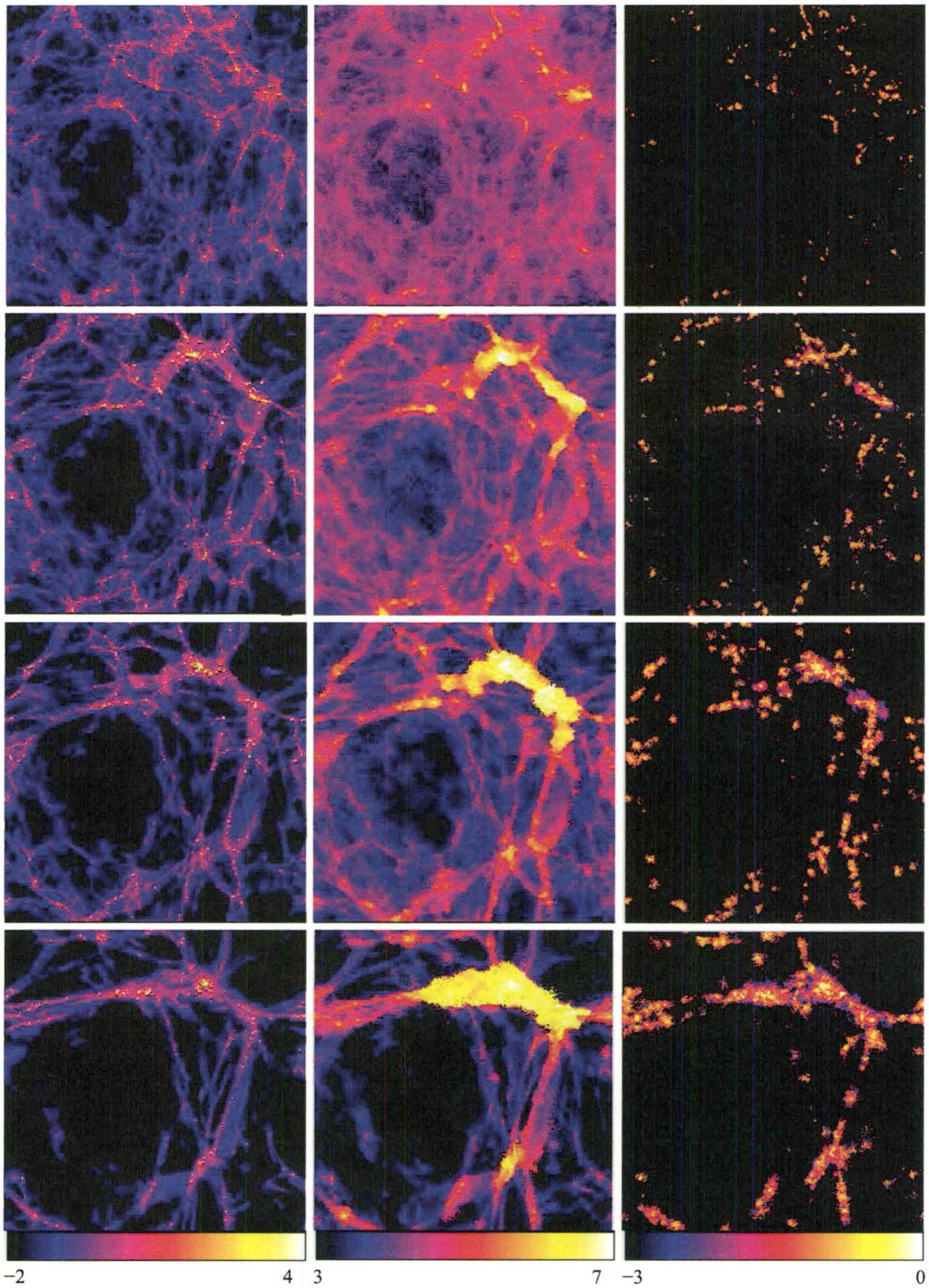

Figure 4.1 Snapshots of density (left), temperature (middle) and metallicity (right) for a thin slice (40 Mpc × 40 Mpc × 0.8 Mpc) of the reference simulation "mcd_40_256". From top to bottom row the redshifts are: z = 4, 2, 1 and 0, respectively. The color bars indicates the range in logarithmic space. The units for density, temperature and metallicity are ρ_{mean}, K and $Z_{\odot}$, respectively. Here we use $Z_{\odot} = 0.0127$.

for regulating the SFH. For example, without superwind models, Springel & Hernquist (2003) and Oppenheimer & Davé (2006) found higher SFR than the observations and a SFH that peaked at $z \sim 4$. Our results suggest that the suppression of SFR can also be attained using feedback models without explicit winds. Until $z \sim 0.5$, our simulations show no overproduction of stars.

The simulations do form too many stars at $z < 0.5$. At z = 0 the SFR in simulations is about 2-3 times higher than observations. It appears that star formation in galaxies larger than the Milky Way produces too many stars in simulations compared with observations (cf. Section 4.1.1.2). This is the so called "overcooling" problem that persists in most current cosmological and galaxy-scale simulations, where too much gas in simulations cools and accreted onto galaxies and form too many stars at low redshift. As large galaxies or galaxy clusters become more prevalent at low redshift, the problem becomes more prominent at $z < 0.5$. One possible mechanism to suppress the SFR in large halos is AGN feedback from supermassive black holes (e.g., McCarthy et al., 2010). Since AGN were not included in our model, the global SFR is higher than observations. This will be further discussed in next section where the SFH for different mass halos is shown.

The simulation without metal cooling produced fewer stars at $z < 5$. The difference in SFR between the simulations with and without metal cooling increases from $\sim$ 5 % at z =4 to $\sim$ 20 % at z=1, then decreases to 10 % at z=0. Metal cooling enhances the cooling of the IGM and therefore its accretion rate onto galaxies. Choi & Nagamine (2009) also found enhancement of the SFR with metal cooling, though their SFR was generally enhanced by 20% to 30% over all redshifts below z=15, and in some runs by 50% at z=1. The discrepancy may result from their adoption of the Sutherland & Dopita (1993)

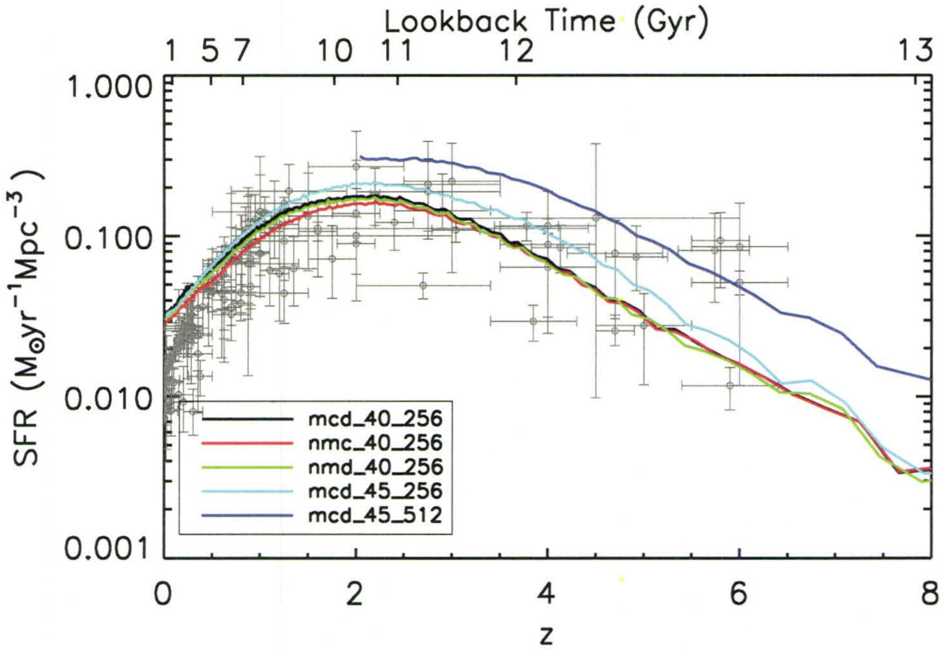

Figure 4.2 Star formation rate (SFR) density (in unit of $M_\odot$ yr^{-1} Mpc^{-3}) as a function of redshift. Data were compiled from Hopkins (2004) and scaled to the same IMF and cosmology as in our simulations. The moderate resolution simulations give SFR consistent with observations down to redshift 0.5. The high resolution run has a significantly higher SFR but is still in broad agreement with observations.

metal cooling rates that are significantly higher than what we used, since their rates do not include the radiation background. However, Schaye et al. (2010) used the cooling model from Wiersma et al. (2009a) which also includes the suppression of metal cooling by UV background, and yet still found a larger enhancement of the SFR comparable to Choi & Nagamine (2009). This is possibly due to the much higher metallicities in stars and the ISM in their simulations (Wiersma et al., 2009). They used higher yields in general, and in particular, they included mass loss by AGB stars which may dramatically contribute to the enrichment of the ISM.

The simulation without metal diffusion (but with metal cooling) also produced slightly fewer stars (about 6% mean) than the reference run at $z < 4$, because metal diffusion allows enriched particles to mix their metals, so more particles experience metal cooling and turn into stars. On the other hand, the metallicities of the original enriched particles are reduced because of the diffusion, thus those particles have less cooling hence are less likely to form stars. Our result suggests that the first factor dominates. Since the effect of metal diffusion relies heavily on metal cooling, it is smaller than in the case where the metal cooling was turned off.

The effect of resolution on the SFR is shown in the convergence runs "mcd_45_256"(cyan) and "mcd_45_512" (blue). At z = 8, the high resolution run produces a 3 times larger SFR. Although the result does not converge by z = 2, the difference between these two runs does steadily decrease with time. At z = 2, it reaches about 50%. The SFR from "mcd_45_512" is close to the high end of the observational data but still consistent with them. The increased star formation is the same magnitude seen in the convergence tests in Stinson et al. (2006), where it was determined that higher resolution simulations produce more high density gas. High density gas forms more stars because it surpasses the density threshold (cf. Section 2.2.1) where gas in the low resolution simulations does not. In fact, the SF density threshold used in this work, $n_H = 0.1\ \mathrm{cm}^{-1}$, is low compared to the gas density of the ISM in reality. This value is suitable for moderate resolution cosmological simulations and was used as a standard value (Stinson et al., 2006, and references therein). But with increased resolution, when the galactic structure can be better resolved, the threshold should be increased accordingly. To single out the resolution effect, in this work the threshold is kept the same, thus it is expected that higher resolution run produce more stars. The difference in SFR is most prominent in early epochs when galaxies are small. This will be further discussed in the next section where the SFRs from different mass halos are plotted. The effect of variability in the initial conditions due to cosmic variance is also worth noting: the "mcd_45_256" run has slightly lower (but comparable) resolution than the reference run. However, it has a higher SFR at z > 1.

4.1.1.2 SFH from Different Mass Halos

To investigate how halos of different masses contribute to the total SFH, Figure 4.3 shows the SFH for halos with masses in the ranges of $10^9 - 10^{11} M_\odot$, $10^{11} - 10^{12} M_\odot$, $10^{12} - 10^{13} M_\odot$ and $> 10^{13} M_\odot$. At each redshift, the halos were identified using a friends of friends (FOF) algorithm with a linking length (ϵ_{link}) of 0.2 of the mean inter-particle separation (which is about 30 kpc in the reference simulation). FOF is a simple halo finding method. Any particle that is within the linking length of another particle that belongs to a halo, also belongs to that halo. The linking length is related to the overdensity by $\delta \sim (1/\epsilon_{link})^3$ so a choice of $\epsilon_{link} = 0.2$ of the inter-particle separation implies gas with overdensity $\gtrsim 125$ will be found within a halo. The halo mass plotted here is the sum of dark matter, gas and stars. The halo finding was performed on all the outputs ($\Delta z = 0.25$) from $z = 7$ to $z = 0$. The simulation records the formation time t for each star. The time is converted to redshift $z(t)$ according to the cosmology used. If $z(t)$ lies between two output redshifts, $z_1 < z(t) \leq z_2$ then the halo mass at z_1 is used. Because we use the lower-redshift output for halo mass, the mass may be slightly higher since haloes grow with time.

The plot shows that at high redshift ($z > 5.5$) the star formation is

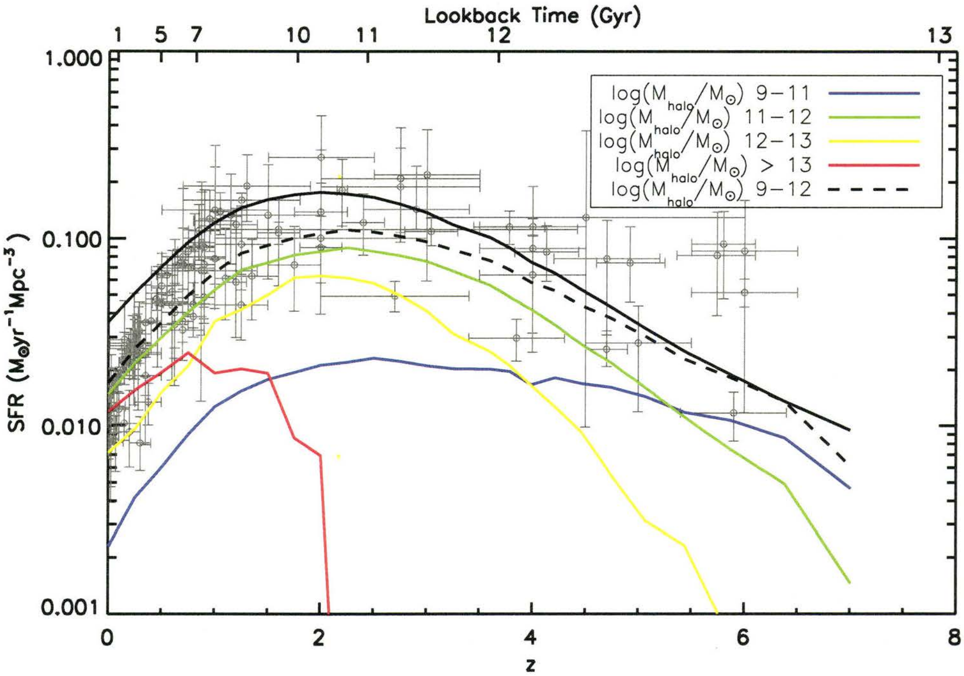

Figure 4.3 Star formation rate (SFR) density (in unit of $M_\odot$ yr^{-1} Mpc^{-3}) contributed from different halos masses as a function of redshift for the reference run. The data shown are the total SFR density, compiled from Hopkins (2004) and scaled to the same IMF and cosmology as in our simulations. The black solid line indicates the total SFH (i.e. same as the black curve in Figure 4.2). The black dashed line indicates total SFR contribution from all halos with mass less than or equal to $10^{12}M_\odot$.

mostly contributed by low mass dwarf galaxies and galaxy progenitors. This is consistent with the hierarchical structure formation model in which small progenitor galaxies form first, and large galaxies form through merging of smaller objects. Below z $\sim$ 5 galaxies with intermediate mass range (10^{11}-10^{12} $M_\odot$) start to dominate the star formation. At $z < 2$ the SFR declines for all halos less than 10^{13} $M_\odot$, but the contribution from large halos > $10^{13}M_\odot$ (can be large galaxies or galaxy groups/clusters, indicated by the red curve in the figure) becomes important. And this remains the case to z=0. Observationally, large elliptical galaxies and galaxies in clusters appear red and do not have strong star formation activity. As discussed above, the inconsistency with observations may be due to the lack of additional strong feedback processes such as AGN in our simulations. Because large halos have deeper gravitational potentials, stellar feedback itself may not be sufficient to disperse the star-forming gas and suppress the SFR in these objects. As a result, at z <0.5, although the SFR from galaxies of Milky Way mass or less ($\lesssim 10^{12}M_{\odot}$) is consistent with the observations (as shown by the dashed line in Figure 4.3), contributions from large halos significantly increase the total SFR, making it higher than the data.

Figure 4.4 shows the level of convergence of the SFR in each halo mass range using the (45 Mpc)^3 runs "mcd_45_256" and "mcd_45_512". Except for the most massive halos ($> 10^{13}M_{\odot}$), resolution increases the SFR for all halo masses. This is related to the implementation of star formation in the GASOLINE code, as discussed in the previous section and in Stinson et al. (2006). The increment in SFR generally decreases as halo mass increases, as more massive halos are better resolved even for the lower resolution runs. For halos with mass above $10^{11}M_{\odot}$ the increment of SFR varies from 30% to 50%, consistent with the Stinson et al. (2006) test. For halos of $10^9 - 10^{11}M_{\odot}$ the effect of resolution is more significant and the average increase in SFR is about a factor of 2.5-3 in this mass range. In the range of $10^9 - 10^{10}M_{\odot}$ (not plotted in the figure), the difference between high and low resolution is more than an order of magnitude. For an object of $10^9M_{\odot}$, in the high resolution case it is sampled by $\sim$ 100 particles, while in the low resolution case it contains only about 10 particles, below the resolution limit. Because the halo is not sampled and its density peak is not resolved, the chance for particles to surpass

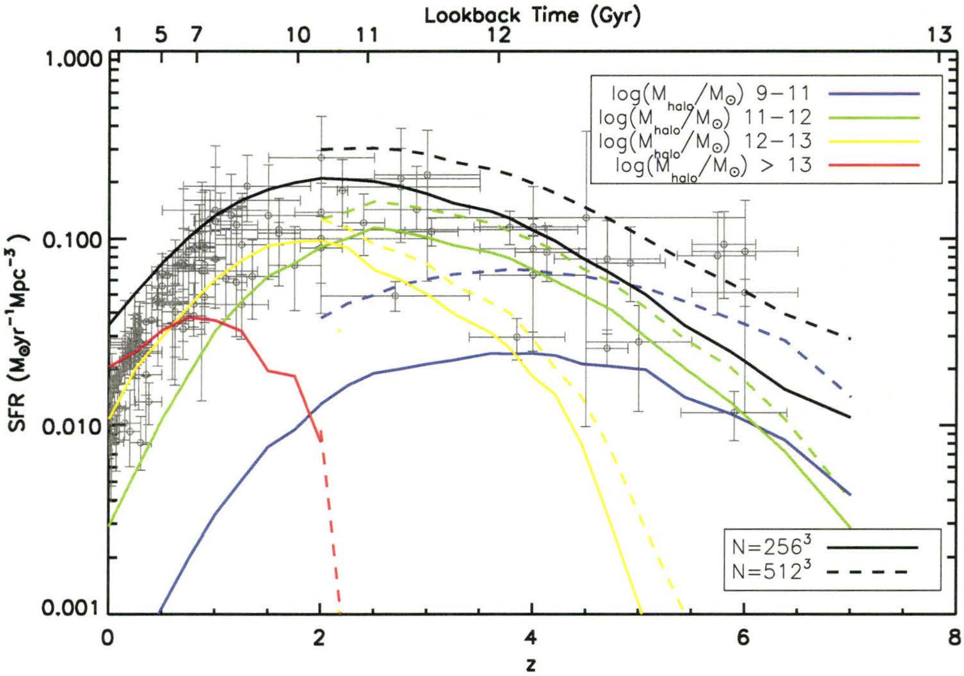

Figure 4.4 Star formation rate (SFR) density (in unit of $M_\odot$ yr^{-1} Mpc^{-3}) contributed from different halos masses as a function of redshift for the runs "mcd_45_256" (solid line) and "mcd_45_512" (dashed line). The observational data shown are the total SFR density, compiled from Hopkins (2004) and scaled to the same IMF and cosmology as in our simulations. The black lines indicates the total SFH, and the coloured lines indicated the contribution from different mass halos.

the threshold is much lower. Since at high redshift the total SFR is dominated by dwarf galaxies, the discrepancy in total SFR is higher at early epochs.

4.1.2 Evolution of $\Omega_{\rm HI}$

The evolution of the cosmic mass density in neutral hydrogen ($\Omega_{\rm HI}$) with redshift and its relation to stellar mass density is one of the key observables for understanding the interaction between gas and galaxies. Observations of damped Ly-α systems (DLAs) (Prochaska et al., 2005; Rao et al., 2006; Prochaska &

Wolfe, 2009) and the H I 21-cm emissions (Zwaan et al., 2005; Lah et al., 2007) (shown in Figure 4.7) suggest that $\Omega_{\rm HI}$ does not evolve substantially through cosmic time, even though the stellar mass density keeps increasing. This implies that there is a steady supply of gas cooling onto galaxies, providing fuel for star formation. The decrease of H I at z $\sim$ 2.3 has been linked to violent feedback processes, including SN, galactic winds and AGN activities (Wolfe et al., 2005; Prochaska & Wolfe, 2009), but it is not clear why the amount of H I increases back at z $<$ 2.3. Prochaska & Wolfe (2009) argued that the data at z $\lesssim$ 2 was biased high and $\Omega_{\rm HI}$ should remain constant from z = 2.2 to z=0 (the last 10 Gyrs). The non-evolution of $\Omega_{\rm HI}$ suggests that star formation is self-regulated such that gas accretion, star formation and feedback processes balance each other. Numerical simulations without mass loss through winds (Cen et al., 2003) found $\Omega_{\rm HI}$ is several times higher. Nagamine et al. (2004a) included the superwind model from Springel & Hernquist (2003) in their simulations so that neutral gas could be ejected from the galaxies, which produced the correct amount of $\Omega_{\rm HI}$ at $z > 2$, but at $z < 2$ too much material was blown away, resulting in a deficit of $\Omega_{\rm HI}$ (dashed line in Figure 4.7).

Because most neutral hydrogen resides in damped Ly-α systems, which are clouds with H I column densities larger than 2×10^{20} cm $^{-2}$ (Wolfe et al., 2005, and references therein), the gas is mostly self-shielded from external ionizing photons. Self-shielding was not modeled during the simulations, however we used the results from a radiative transfer post-processor to recalculate the ionization states of hydrogen (Pontzen et al., 2008). In this post-processor, the UV background is attenuated as $I = I_0 e^{-\tau_{eff}}$ where I and I_0 are the intensities of the attenuated and original UV background, respectively. τ_{eff} is the effective optical depth for certain species (H I, He I or He II) and is a function of gas density $\tau_{eff} = \tau_{eff}(\rho)$. The dependance on density was calculated by Pontzen et al. (2008) using an iterative radiative transfer calculation on an adaptive mesh in their cosmological simulations of Damped Lyman-α systems. Specifically, τ_{eff} was averaged over six different directions along the density gradient. Because it is post-processing, the model ignores the heating rate change caused by self-shielding and its effects on dynamics. However, (Pontzen et al., 2008) evaluated this effect and found it to be very small. Figure 4.5 plots the attenuation in photo-ionization coefficients $\Gamma_{\rm HI}$, $\Gamma_{\rm HeI}$ and $\Gamma_{\rm HeII}$ as a function of density. In our implementation, these attenuation-density relations are provided in the code as interpolation tables (linear interpolation is used).

With the attenuated UV radiation, the new ionization state of hydrogen is then calculated assuming ionization equilibrium (cf. Equation 3.1 in Chapter 3). The incident (unattenuated) ionizing background was the standard UV from Haardt & Madau (2005) used in calculating metal cooling, reduced by a factor of ~ 2 (this will be discussed in section 4.1.3 below). However, variations of this magnitude have practically no impact on the dense gas that dominates $\Omega_{\rm HI}$ since they are mostly self-shielded. Figure 4.6 shows, at z=2, the mass fraction of neutral hydrogen ($Y_{\rm HI}$) of each gas particle as a function of density and temperature before and after the self-shielding approximation. The figure indicates that gas with density $n_H \gtrsim 10^{-4}\mathrm{cm}^{-3}$ (corresponding to overdensity $\delta \gtrsim 300$ at this redshift) and temperature $T \lesssim 10^{4.5} K$ is mostly affected by self-shielding. This is the gas that accretes onto galaxies and participates in star formation. Self-shielding makes $Y_{\rm HI}$ increase faster towards higher densities and lower temperatures. The left lower corner of the panels indicate that the underdense IGM that is cooled by adiabatic expansion is not affected. For the

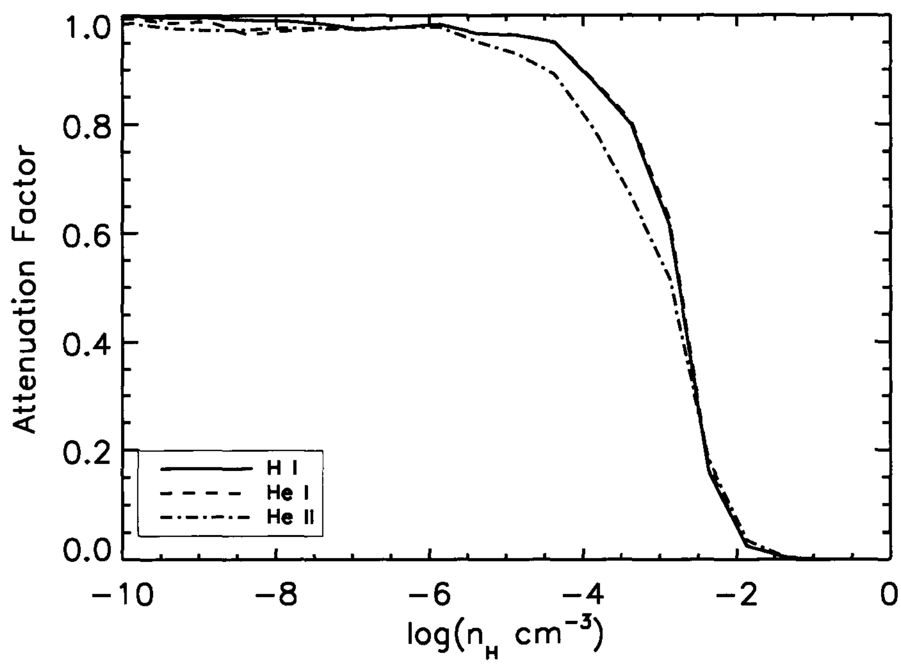

Figure 4.5 The attenuation of the photoionization coefficients for H I (solid line), He I (dashed line) and He II (dot-dashed line) as a function of hydrogen number density, calculated by Pontzen et al. (2008) using a radiative transfer post processor.

gas hotter than $\sim 10^5$ K (indicated by the right "branch" in the lower panel), although it can be dense, the self-shielding effect is also small, since at this temperature collisional ionization dominates.

Figure 4.7 shows the evolution of $\Omega_{\rm HI}$ in our simulations. It shows that after we applied the self-shielding correction, our feedback model produced similar $\Omega_{\rm HI}$ to observations from $z \sim 3.5$ down to $z = 0$ for the runs with moderate resolution. At higher redshift these simulations underestimate $\Omega_{\rm HI}$, possibly because of insufficient resolution (discussed below). The result indicates that our feedback models effectively regulates star formation but not too strongly, so that gas accretion onto disks is not disrupted. Thus it can

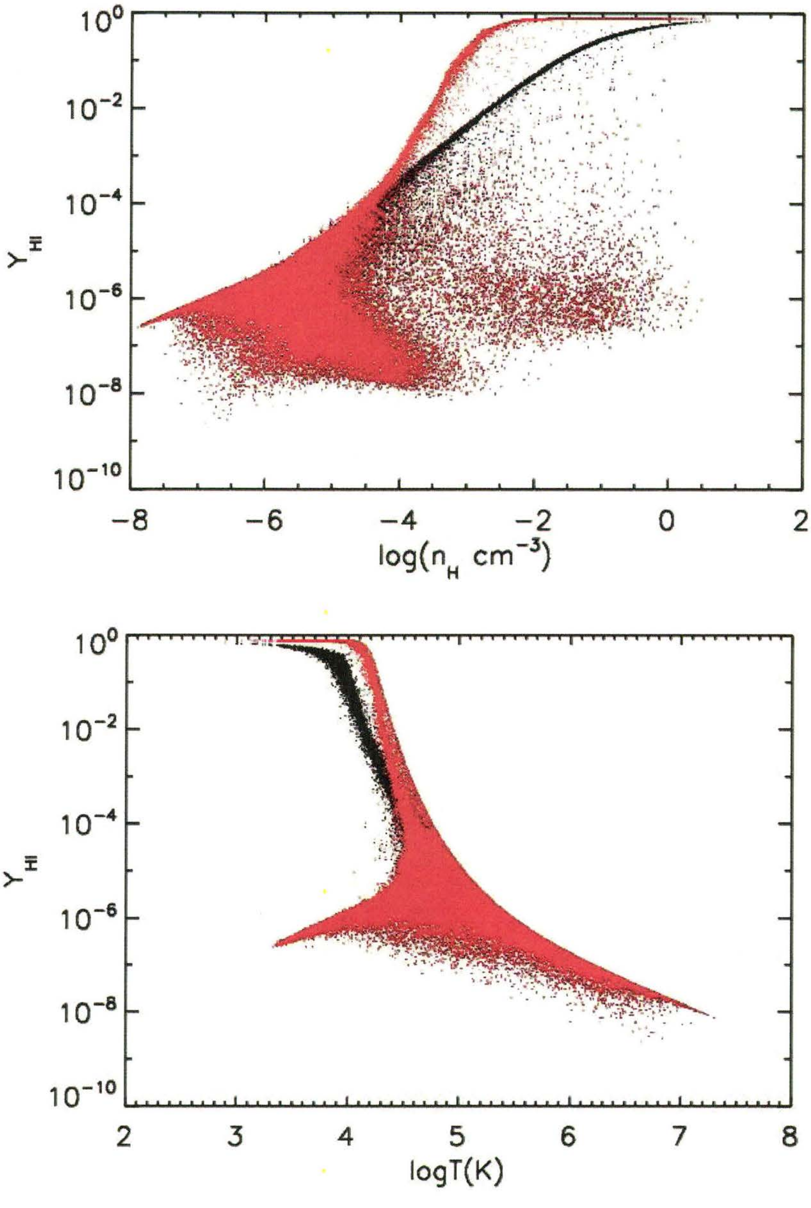

Figure 4.6 *Upper Panel*: Mass fraction of neutral hydrogen, $Y_{\rm HI}$ as a function of hydrogen number density (n_H) at z = 2. *Lower Panel*: Mass fraction of neutral hydrogen as a function of gas temperature at z = 2. Both panels are plotted using 1/100 particles of the reference run. In both panels, the black points indicate the values before applying self-shielding calculation and the red points indicate the ones after.

maintain the steady supply of neutral hydrogen to galactic disks. The shape of the Ω_{HI} relation follows the SFH, which reflects the relation between the H I density and SFR density, i.e. the Schmidt Law for star formation. The decrement at $z = 2.3$ is not reproduced in our simulations, indicating that more violent feedback may be necessary at this limited redshift range if this feature is confirmed. We will investigate wind models in high resolution single galaxy and galaxy group simulations in future work.

As expected, Figure 4.7 shows that metal cooling and metal diffusion increases the amount of neutral hydrogen. The metal cooling effect is obvious at z $\lesssim$ 3 and at z = 0 the increase is $\sim$ 17 %. Metal diffusion has a smaller effect. The reasons for these effects are similar to the ones discussed in SFR analysis in section 4.1.1.

With eight times higher resolution, the simulation "mcd_45_512" produces a significantly higher Ω_{HI} and a flatter curve at z > 2.5 which makes the result compare better with observations. At z = 5, the high resolution run contains about 80% more neutral hydrogen. At z = 2 the Ω_{HI} curve joins the moderate resolution run "mcd_45_256" but has a slightly steeper decreasing slope towards lower z. The difference in Ω_{HI} is likely because the high resolution run better resolves small halos, thus increasing the amount of self-shielded gas. Since small halos dominate at high redshift, the difference is most obvious there. We note that as a result of cosmic variance the "mcd_45_256" simulation contains 15-30% less HI throughout the simulation than the fiducial run even though it has a higher SFR. Thus the relationship between SFR and the gas reservoir Ω_{HI} is not always monotonic as seen in the cases for "nmc_40_256" and "nmd_40_256", higher SFR consumes more neutral gas and thus may decrease the amount of Ω_{HI}.

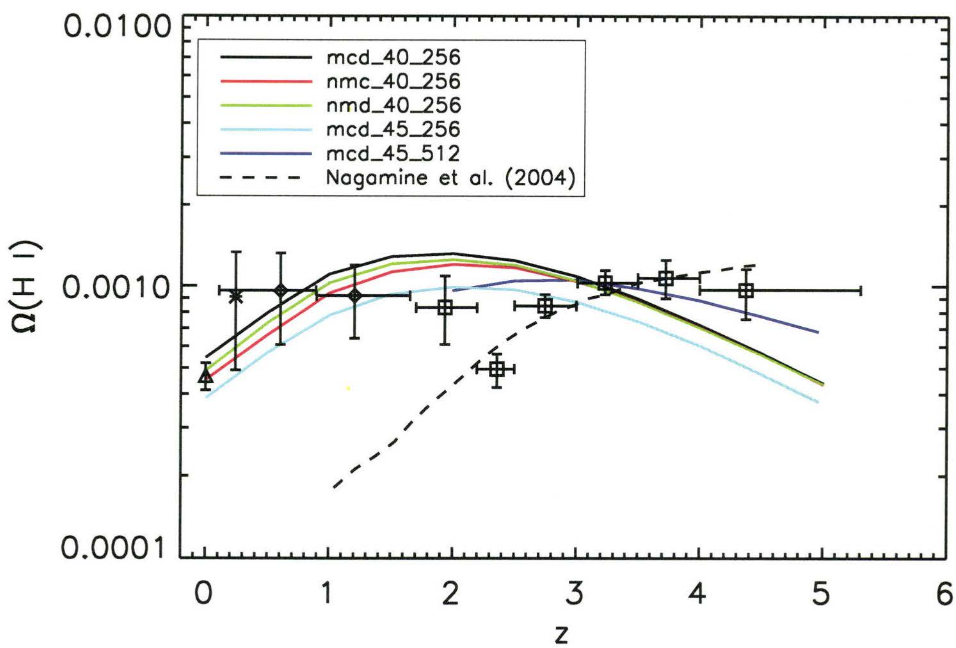

Figure 4.7 Evolution of total neutral hydrogen density in units of critical density today ($\Omega_{\rm HI}$). Observational data points: *Square*: Prochaska et al. (2005); *Diamond*: Rao et al. (2006); *Asterisk*: (Lah et al., 2007); *Triangle*: Zwaan et al. (2005).

Similar to the SFH, the evolution of $\Omega_{\rm HI}$ from contributions of different mass haloes is also plotted (Figure 4.8) for the runs "mcd_45_256" and "mcd_45_512". The convergence level for each mass range is also shown. The halos masses were calculated at the same redshift when the $\Omega_{\rm HI}$ is computed. As for the cosmic SFH, smaller galaxies contribute more to $\Omega_{\rm HI}$ at earlier epochs, as expected from the hierarchical structure formation picture. The majority of $\Omega_{\rm HI}$ comes from galaxies less than $10^{12}\rm M_\odot$, until z $\lesssim$ 2 when objects larger than 10^{12} start to contribute significantly. At low redshift, the existence of significant amounts of neutral hydrogen in halos of mass larger than the Milky Way may explain the overproduction of stars from these halos.

Rees & Ostriker (1977) estimated that for halos of mass $\gg 10^{12}\mathrm{M}_{\odot}$, accreted gas is shock heated to $\gg 10^5$ K thus atoms should be collisionally ionized. Meanwhile, strong feedback from central super massive black holes in these objects can inject kinetic and thermal energy to the ISM. In both cases, the amount of Ω_{HI} from these object is small. As discussed in Section 4.1.1, adding feedback from AGNs is probably necessary to solve this "overcooling" problem in simulated massive halos (See, e.g. McCarthy et al., 2010). The overall near constant evolution of Ω_{HI} comes from contributions of halos in the range of $10^{10} - 10^{12}\mathrm{M}_{\odot}$. The low mass halos ($10^9 - 10^{10}\mathrm{M}_{\odot}$) initially (z $\sim$ 5) contain some H I but the amount decreases quickly with time, possibly because of the increase of UV intensity towards lower redshift. Heating due to photoionization increases the gas temperature to be comparable to the virial temperature of dwarf galaxies thus preventing gas accretion (Quinn et al., 1996). At the high mass end, the contribution from $M > 10^{12}\mathrm{M}_{\odot}$ mass halos increases significantly at later times, because large halos generally form later.

For the intermediate mass range, $10^{10} - 10^{12}\mathrm{M}_{\odot}$, the high and low resolution simulations produce similar amounts of H I for the redshift range compared. Note that although the H I contents are similar, the high resolution run increases its SFR about 40-50%, implying that it is resolution of the high density regions, not the total amount of star forming gas, that affects the SFR in these halos. At $10^9 - 10^{10}\mathrm{M}_{\odot}$, however, the high resolution run gives about 20 times more H I than the low resolution case, this makes the total Ω_{HI} in the former larger than in the latter in the high redshift regime and more consistent with observations. Similar to the SFH case, because the self-shielding optical depth depends sensitively on density, and the density structures in these $10^9\mathrm{M}_{\odot}$ halos are not resolved in the 256^3 run, gas that should have been self-shielded

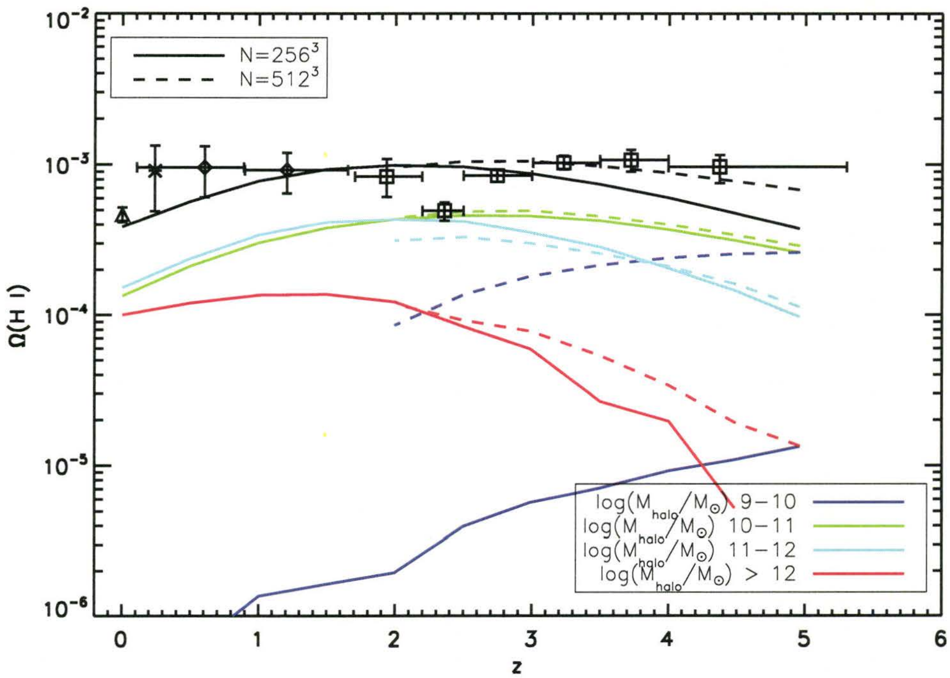

Figure 4.8 Evolution of total neutral hydrogen density in halos of difference masses in units of critical density today ($\Omega_{\rm HI}$). The solid lines are the results from "mcd_45_256" and the dashed lines indicate the high resolution run "mcd_45_512". The Observational data points are from *Square*: Prochaska et al. (2005); *Diamond*: Rao et al. (2006); *Asterisk*: (Lah et al., 2007); *Triangle*: Zwaan et al. (2005).

and would remain ionized thus largely decreasing the amount of neutral gas.

4.1.3 Lyman-α Forest and its Flux Decrement

4.1.3.1 Generate Mock QSO Absorption Spectra

The majority of the intergalactic medium is not luminous. It cannot be observed directly like stars or galaxies. But when there is a background radiation source (most commonly quasars, but also the afterglows of γ-ray bursts or even star light from background galaxies Steidel et al. (2010)), photons with certain wavelengths can be absorbed exciting or ionizing certain ion species in the intervening medium thus produce an absorption line. Absorption features due to primordial and metal ions in QSO spectra provide information about the gaseous medium in the Universe and how it was enriched, and the comparison between observed and synthetic spectra has become an essential tool to understand the nature of these absorbers (Rauch, 1998; Oppenheimer & Davé, 2006, 2009). For example, it is found that the origin of the Lyman-α forest is the cool, diffuse intergalactic medium which is the major baryon repository at high redshift (Rauch, 1998) and the Damped Lyα systems likely to trace the gas accreted onto galaxies and the multiphase ISM (Wolfe et al., 2005). The majority of our knowledge of how metals are distributed in the IGM has also been obtained through absorption spectra of abundant ions such as C III, C IV, Si IV and O VI. In this section I will briefly described how I generate mock QSO absorption spectra for hydrogen. The same method applies for generating metal spectra.

The optical depth of Lyα photons of frequency, ν, is given by (Rybicki & Lightman, 1985; Peebles, 1993):

$$\tau(\nu) = \int n_{HI}(\vec{x})\sigma(\nu)dx \tag{4.1}$$

where $n_{HI}(\vec{x})$ is the number density of H I atoms at position $\vec{x}$ and dx is the physical unit length increment along the line of sight which depends on redshift: $dx = dl/(1+z)$ where dl is the increment in comoving space. $\sigma(\nu)$ is the cross section of Lyα absorption at frequency , given by the Voigt profile:

$$\sigma(\nu) = \frac{3\Gamma\lambda_\alpha^2}{8\pi}\int_{-\infty}^{\infty} dv \frac{1}{b\sqrt{\pi}} exp(-v^2/b^2) \cdot \frac{\Gamma/(4\pi^2)}{(\nu-\nu_0(1+v/c))^2 + (\Gamma/4\pi)^2} \tag{4.2}$$

where $\Gamma = 6.25 \times 10^8 \mathrm{s}^{-1}$ is rate of spontaneous decay from the 2p to 1s level for the hydrogen atom, b is the Doppler width and $\nu_0 = c/\lambda_\alpha$. $\lambda_\alpha = 1216\mathrm{\AA}$ and c is the speed of light. The Voigt profile is the convolution of a Doppler profile and a Lorentz profile. In practice, it is convenient to compute the optical depth from the Doppler profile at each velocity in the spectrum $\tau^D_{v_i}$, then convolve it with the Lorentz profile. From equation 4.1, the optical depth at given velocity v_i is

$$\tau^D(v_i) = \int n_{\mathrm{HI}}\sigma(v; v_i)dx \tag{4.3}$$

where v is the velocity of the intervening gas projected onto the line of sight, including the velocity due to Hubble expansion and the peculiar velocity of the gas. Using SPH simulation data, the above integral can be approximated by a sum:

$$\tau^D(v_i) = \frac{3\Gamma\lambda_\alpha^3}{8\pi^{3/2}} \sum_k \frac{m_p^k Y_{\mathrm{HI}}^k}{b_k m_H} W_{2D} exp((v_k - v_i)^2/b_k^2) \tag{4.4}$$

Here $3\Gamma\lambda_\alpha^3/(8\pi^{3/2}b_k)exp((v_k - v_i)^2/b_k^2)$ is the contribution to the Doppler profile line centre from particle i, i.e. $\sigma(v; v_i)$, m_p^k is the mass for particle k, Y_{HI}^k is the H I mass fraction, $m_H = 1.67 \times 10^{-24}$ g is the mass of hydrogen atom, and W_{2D} is the SPH kernel projected onto two dimensions (with units of length^{-2}). Initially only thermal broadening is added, so $b_k = \sqrt{2k_B T_k/m_H}$, in which T_k is the temperature of the gas particle and k_B is the Boltzman constant. In practice, only particles with distances to the line of sight of less than 2 smoothing length for this particle, $2h_k$, contribute to the absorption. To fully utilize most information in the box, a line of sight may be sent through the box multiple times at different locations. The periodicity of the simulation box is used so that there is no discontinuity in the spectra.

This Doppler-only spectra is then convolved with the Lorentz profile.

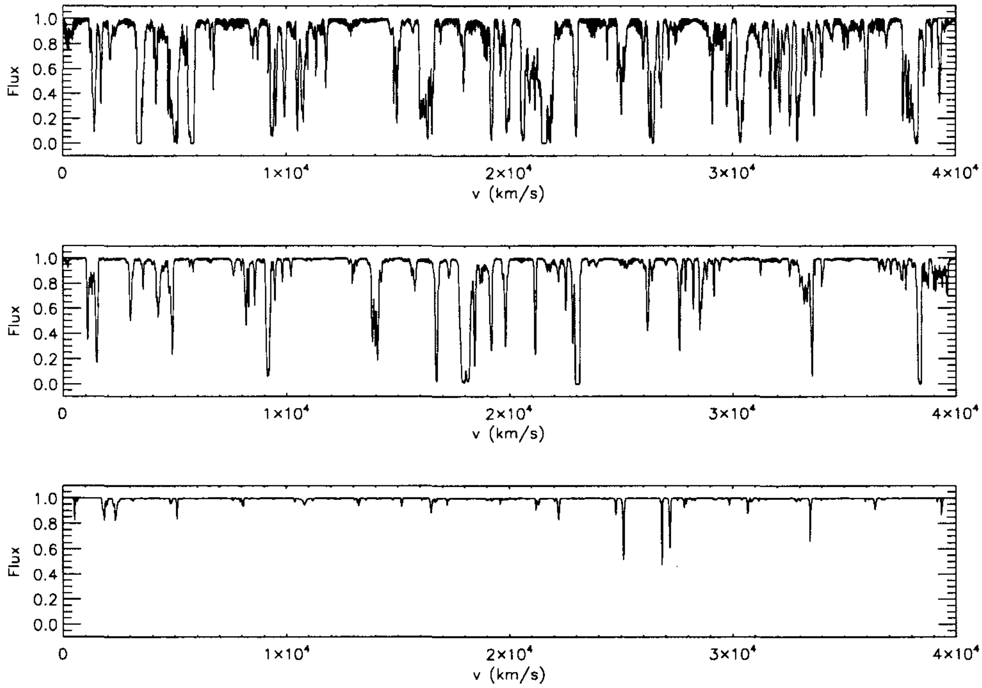

Figure 4.9 Simulated Lyα spectra from the reference run "mcd_40_256" with spectral resolution $\Delta v = 12$ km/s. The continuum flux is assumed to be $F_0 = 1$. The spectra are "clean" and have not been convolved with an instrumental profile or combined with any noise. From the upper panel to the bottom panel it is the spectrum extracted from simulation outputs of z = 3, 2 and 0, respectively.

After discretization, the convolved spectra at certain velocity v_j is given by

$$\tau^c(v_j) = \sum_i \tau^D(v_i) \frac{\Gamma/(4\pi^2)}{(\nu_0/c)^2(v_j - v_i)^2 + (\Gamma/4\pi)^2} \cdot (\nu_0/c)\Delta v \qquad (4.5)$$

Here the sum is over all possible v_i and Δv is the velocity increment. The relation $\nu = (1 + v/c)\nu_0$ and $\Delta\nu = \nu_0/c\Delta v$ are used to convert frequency ν to velocity v. With the optical depth, the flux at each velocity is given by $F = F_0 e^{-\tau^c(v)}$ with F_0 the continuum flux.

Figure 4.9 gives an example of mock Lyα spectra generated from the reference simulation. The spectra are generated from the reference 40 Mpc run, but not convolved with an instrumental profile or combined with any noise. It shows how the number of absorbing systems decreases with redshift, as the Universe expands and the amount of cool, diffuse IGM decreases with time. QSO spectra with metal absorptions can be generated similarly using the method described above. It will be interesting to carry out detailed comparisons of the Lyα forest and metal absorber properties with observations, including, for example, the column density distribution and the line width distribution. From such comparisons we can understand how the essential quantities of the IGM, such as temperature and metallicity, are reflected in the hydrogen or metal absorption lines. For example, the equivalent width of an absorption line (if not saturated) indicates the gas motion. If thermal motion dominates the gas motion, then the line width indicates the temperature. Other motions such as turbulence also contribute to the line width. A discrepancy between the properties of simulated and observed spectra can imply that certain important physics is omitted in simulations (e.g. Oppenheimer & Davé, 2009). These comparisons will be performed in future work but are not included in this thesis.

4.1.3.2 Evolution of Lyα Flux Decrement

The Lyman-α forest traces the neutral hydrogen in the diffuse IGM. Since the IGM is optically thin, the mean flux decrement of the Lyman-α forest, $\mathrm{D}_{\mathrm{Ly}\alpha}$, is sensitive to the UV radiation and can be used to calibrate the UV background in simulations. The mean flux decrement is defined by:

$$D_{\mathrm{Ly}\alpha} =< 1 - F/F_0 >=< 1 - e^{-\tau} >= 1 - e^{-\tau_{eff}} \tag{4.6}$$

where F is the observed flux, F_0 is the continuum flux and τ_{eff} is the effective optical depth defined as $\tau_{eff} \equiv -ln(1 - D_{\mathrm{Ly}\alpha})$. We generated $Ly\alpha$ spectra by tracing lines of sight through every simulation box and each line of sight consists of 25 line segments (i.e. the line of sight passes through the simulation 25 times), which were spread through the entire box. We have used more line segments (75) with different orientating angles and compare to test if the box is sufficiently sampled. It is found that 25 segments is sufficient to compute $D_{\mathrm{Ly}\alpha}$. As described in the previous section, particles that lay within two smoothing lengths measured perpendicularly to their closest line segments contributed to the absorption along the line, and the amount of contribution was weighted using the SPH smoothing kernel. The particles' peculiar velocity and thermal velocity and the Hubble expansion were all taken into account. The H I, He I and He II fractions ($Y_{\mathrm{HI}}, Y_{\mathrm{HeI}}$ and Y_{HeII}) were calculated during the simulation as described in Chapter 3. The Lyα optical depth at each velocity due to Doppler broadening was calculated and then convolved with the Lorentz profile.

Figure 4.10 depicts the evolution of $D_{Ly\alpha}$ compared to the observations of Bernardi et al. (2003), Schaye et al. (2003), Kirkman et al. (2007) and Faucher-Giguère et al. (2008). When we attenuate the UV spectrum by a factor of 2, our results agree with most observations up to z $\sim$ 3.5. At higher redshift, our results are slightly lower than, but still broadly consistent with, the observational data. The biggest difference is seen when comparing to Bernardi et al. (2003). The discrepancy may indicate that more UV attenuation for z $\gtrsim$ 3 in our simulation is necessary. However, observations of the Lyα forest at high redshift may be subject to large uncertainties due to the continuum correction (Bernardi et al., 2003) and metal line contamination (Schaye

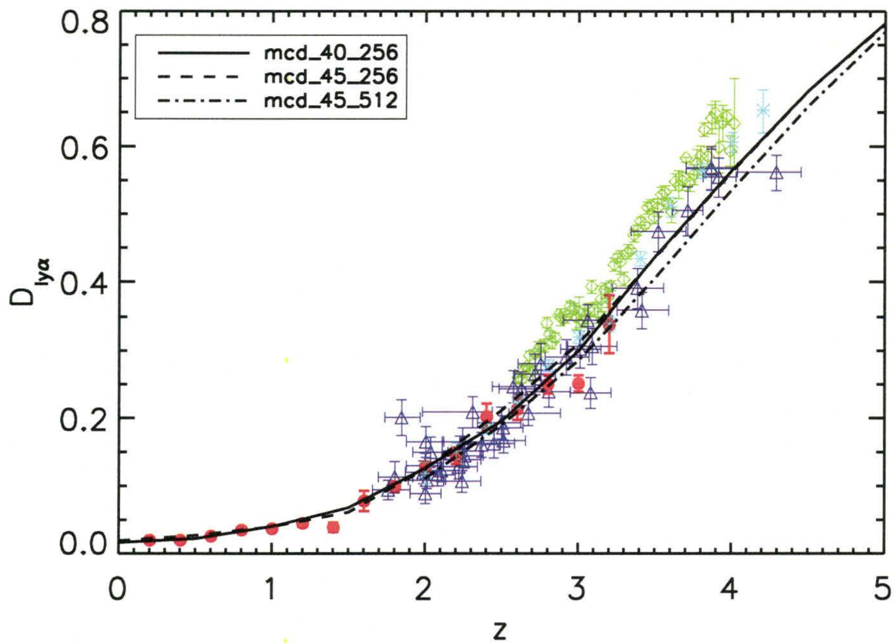

Figure 4.10 The evolution of the mean flux decrement of the Ly-α forest from the reference simulation ("mcd_40_256") and the convergence test ("mcd_45_256" and "mcd_45_512"). The UV background was attenuated by a factor of 2 as discussed in the text.
Color symbols with error bars indicate the observational data. *Green diamonds*: Bernardi et al. (2003); data here are derived from their original evolution of effective optical depth, $\tau_{\rm eff}$ in their Fig. 4; *Blue triangles*: Schaye et al. (2003); data here are derived from the original $\tau_{\rm eff}$ (cf. equation 4.6) after removal of pixels contaminated by metal lines (Table 5); *Red solid dots*: Kirkman et al. (2007); *Cyan asterisks*: Faucher-Giguère et al. (2008); derived from their $\tau_{\rm eff}$ evolution after contamination correction (Table 1).

et al., 2003). The Schaye et al. (2003) and Faucher-Giguère et al. (2008) data are contamination corrected and our results compare better with these data. Hence, a factor of 2 seems sufficient and we use this value for all subsequent calculations. Due to limitations of the observations, the exact shape and intensity of extragalactic UV is poorly constrained. Recent radiative transfer calculations from Haardt and Madau found a similarly lower UV background intensity compared to their previous result in Haardt & Madau (2005) (private communication with Francesco Haardt). The attenuated UV background is only used in the analysis, but not in the entire simulation. The star formation model is also only calibrated for the unattenuated UV. Although for the diffuse, highly ionized primordial IGM, the effect of photoionization on gas dynamics is small (Croft et al., 1998), UV does affect metal cooling and hence star formation. Thus, by using the original UV background without attenuation, our metal cooling calculation may have overestimated the effect of photo-ionization. However, along with other authors, we are also neglecting local ionizing sources which correct the UV upward to a significantly greater extent within galaxies. These details of ISM physics are potentially important but beyond current capabilities where we must rely upon relatively crude ISM models.

Focusing on the convergence test, with high resolution (dot-dashed line) the Lyα decrement evolves very similarly with redshift, but is a few percent smaller than the lower resolution (dashed line) run. The decrease in $D_{Ly\alpha}$ is consistent with the increase in SFR and $\Omega_{\rm HI}$. It can be interpreted as when more gas accretes onto galaxies and forms stars for high resolution, the H I content in the IGM (probed by the Lyα forest) decreases.

4.2 Metal Enrichment History

We now examine the enrichment of the IGM through the metal distribution in different gas phases. We examine how they evolve and the effects of metal diffusion and cooling. The gas phases were defined using the convention of Wiersma et al. (2009). All the gas that has hydrogen number densities $n_H > 0.1$ cm^{-3} is star forming gas (SF gas). Of all the non-star forming gas (non-SF gas), gas with $10^5K < T < 10^7K$ is the warm-hot intergalactic medium (WHIM) and gas with $T > 10^7K$ is the intracluster medium (ICM). Of the cooler medium ($T < 10^5K$), that with overdensity $\rho/\rho_{mean} > 100$ is associated with galactic halos, while that with $\rho/\rho_{mean} < 100$ is the diffuse IGM (cf. Figure 4.11). Note that these definitions are somewhat arbitrary and there is no well-defined border for each gas phase. In particular, at low redshift, a substantial part of the WHIM comes from the shock-heated gas accreting onto galaxies so it is likely to be associated with galactic halos. However, by these definitions gas is roughly divided according to its location and key physical processes.

4.2.1 Evolution of Gas and Metal Fractions

Figure 4.12 shows how the mass fractions of stars and each gas phase evolve. Almost all baryonic mass is in the diffuse IGM at z=7. By z=0, the mass fractions in stars, the diffuse IGM and the shock heated WHIM are about 20%, 40% and 40%, respectively for the moderate resolution runs. The stellar mass fraction at z =0 is consistent with observations (Wilkins et al., 2008, and references therein), although close to the high end. A large amount of WHIM forms at low redshift when gas is shock heated when falling into halos. The

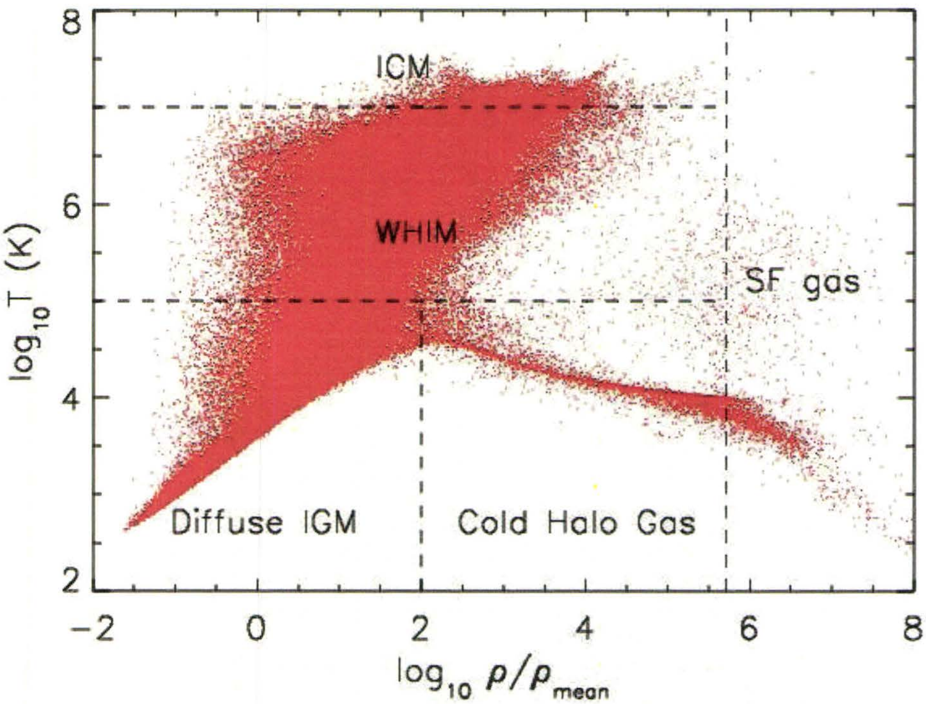

Figure 4.11 Distribution of gas particles from the reference run in the temperature-density ($\rho - T$) phase diagram at z = 0. The dashed lines indicate the definitions of the diffuse IGM, the cold halo gas, the star forming (SF) gas, the WHIM and the ICM. Here the density criterion for star forming gas, $n_{\rm H} > 0.1{\rm cm}^{-3}$, is converted to an overdensity criterion $\rho/\rho_{mean} \gtrsim 5.1\times10^5$. See detailed definitions of different gas phases in the text. These definitions are the same as in Wiersma et al. (2009)

.

mass fraction of WHIM gas is consistent with SPH simulations using explicit galactic superwind models (Oppenheimer & Davé, 2006; Choi & Nagamine, 2009), and simulations using an Eulerian code (Cen & Ostriker, 2006). The amount of star forming gas (ISM) and galactic halo gas evolves similarly to the SFH shown in Figure 4.2, reflecting the close relationship between the ISM, halo gas and SF activity.

The blue and cyan lines in Figure 4.12 show the convergence of mass fractions. At high redshift, the 512^3 simulation has a larger mass fraction in stars, the ISM, halo gas and the WHIM. Resolving smaller halos at large z increases the amount of gas in galaxies (halos and the ISM) and enhances SF. Consequently, enhanced stellar feedback increases the amount of WHIM. This effect is more significant at higher redshift and decreases with time. The WHIM fraction converges at $z < 4$. The ISM and halo gas fractions reach similar values as in the low resolution run at z =2, although they seem to decline slightly faster towards low z. A similar trend is also seen in the evolution of Ω_{HI} as described in Section 4.1.2. This is expected because most of the neutral gas in the Universe located in galaxies. For the stellar mass, however, there is about 37 % more in the high resolution run at z = 2. Although it is still difficult to predict the stellar fraction at z = 0, we expect that the difference will be lower at z = 0 since there is already no excess in the reservoir gas (the ISM) at z =2. In fact, early star formation seen in the high resolution simulation may consume the gas that would otherwise contribute to SF at low redshift, hence the SFR may decline faster towards low z.

Figures 4.13 show how the metal fractions present in stars and different gas phases evolve. At z = 7, gas (SF and Non-SF) contains the majority of the metals while stars contain only a few percent, which is possibly because the time scale for gas consumption is longer than the age of the Universe, so that metals in the ISM do not have enough time to be incorporated into stars. With metal diffusion, initially the non-SF gas (the IGM + halo gas) and the SF gas (i.e. the ISM) contain comparable amounts of metals, with the former having slightly more in most runs. With time, the metal fraction in the non-SF gas decreases and the metals budget is dominated by the ISM and later by stars. As z=0, 80% to 90% of metals reside in stars. The IGM and

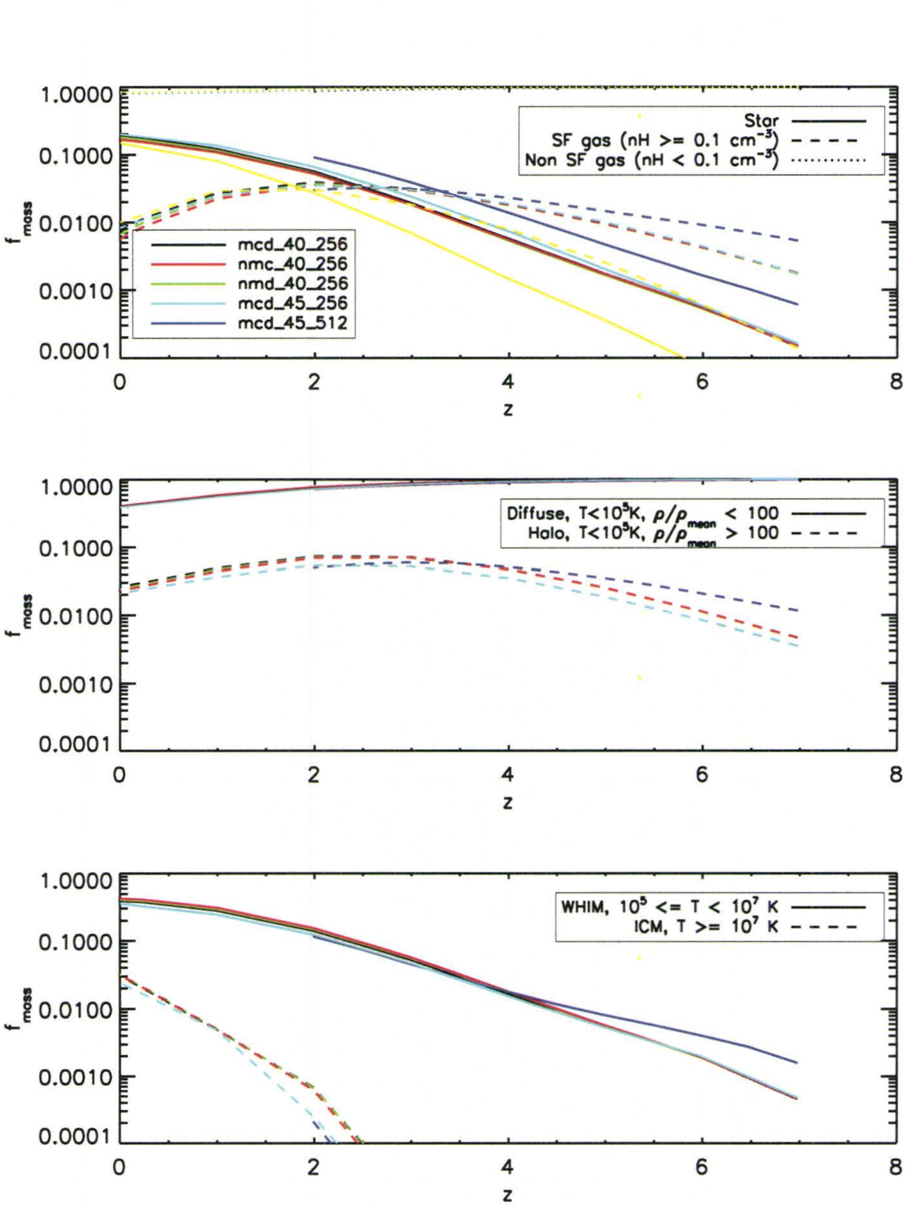

Figure 4.12 The evolution of the baryon mass fraction in various gas phases and stars. The gas is divided into star forming gas, diffuse IGM, halo gas and WHIM according to the definition described in the text. *Black*: the standard run "mcd_40_256". *Red*: the run with metal cooling turned off. *Green*: the run with no metal diffusion. *Cyan*: medium resolution run in the convergence test "mcd_45_256". *Blue*: high resolution run "mcd_45_512". The meaning of each line type in each panel is defined by the legends in that panel.

halo has about 10% of the metals and the ISM has only a few percent. That the IGM contains a larger fraction of metals at higher redshifts suggests that the IGM enrichment process is efficient at early epochs, possibly because it is easier for wind material to leave the shallow potential wells of early objects. For different phases of the IGM, metal fractions in both the WHIM and the diffuse IGM decrease with time. For example, in the standard run, the WHIM metal fraction decreases from $\sim$ 40% at z=7 to about 10% at z=0, the metal fraction in diffuse IGM decreases from $\sim$ 10% to $\sim$ 1%. The ICM, on the other hand, increases its share of metals as galaxy clusters form at low redshift.

Figure 4.14 shows how different wind models can result in different enrichment histories by comparing our results of metal fraction evolution with the ones from Wiersma et al. (2009) (red lines) and Davé & Oppenheimer (2007) (blue lines). Both used kinetic feedback and explicit wind models characterized by a wind speed (v_w) and a mass-loading factor (η). The former uses fixed values for the wind parameters and wind materials are not decoupled while ejected (Dalla Vecchia & Schaye, 2008). The latter adopted the "momentum driven wind" model (Murray et al., 2005) with v_w proportional to the galaxies velocity dispersion and η inversely proportional to it. The winds are also hydrodynamically decoupled when ejected into the ISM. For the definition of different gas phases, Davé & Oppenheimer (2007) used a different criteria for their shock heated WHIM gas ($T > 3 \times 10^4$ K) and for halo gas (which includes hot intracluster gas). Thus the comparison between Davé & Oppenheimer (2007) and this work is not direct, but such a comparison can still be indicative.

In general, with the efficient decoupled wind model, Davé & Oppenheimer (2007) obtained a large fraction of metals in the IGM, less in stars

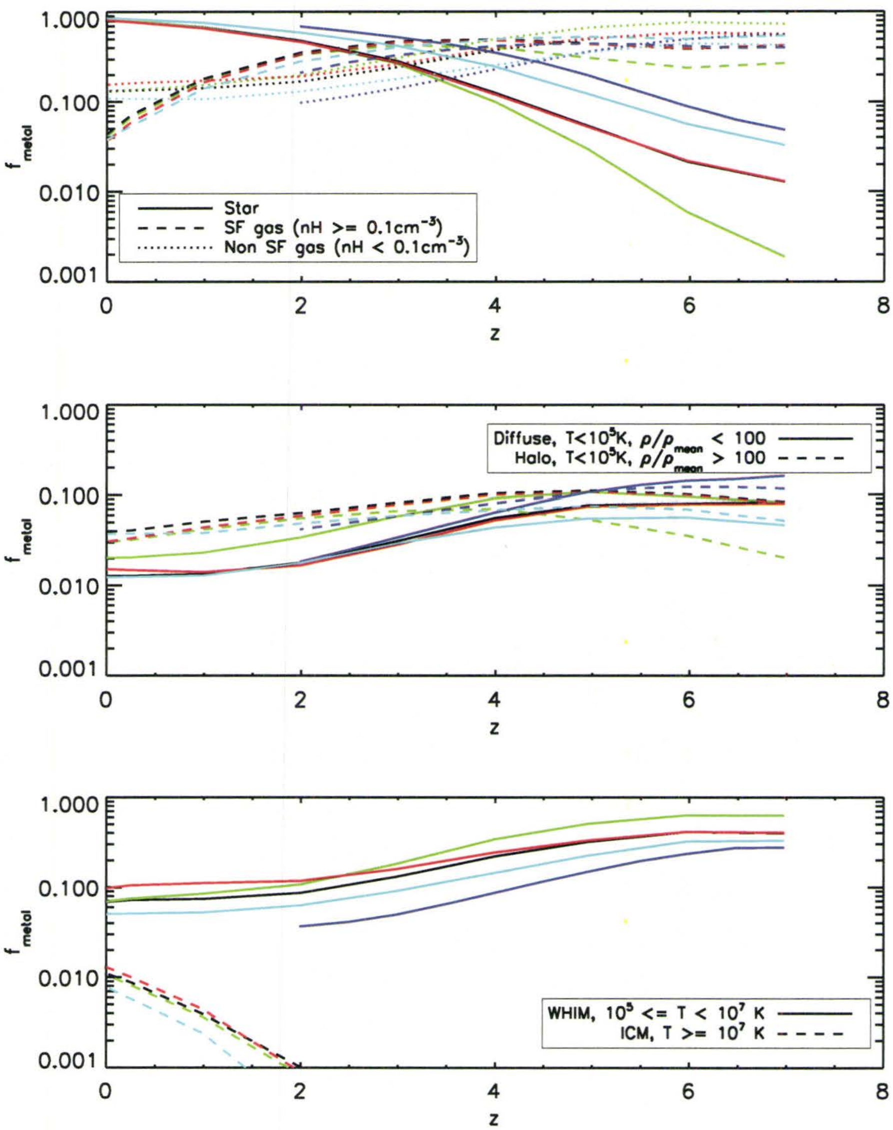

Figure 4.13 The evolution of metal fraction in various gas phases and stars. The gas is divided as star forming gas, diffuse IGM, halo gas and WHIM according to the definition described in the text. *Black*: the standard run "mcd_40_256". *Red*: the run with metal cooling turned off. *Green*: the run with no metal diffusion. *Cyan*: medium resolution run in the convergence test "mcd_45_256". *Blue*: high resolution run "mcd_45_512". The meaning of each line type in each panel is defined by the legends in that panel.

and the ISM. The most significant difference is that most metals reside in the cooler, diffuse IGM from $1.5 < z < 6$, before stars start to dominate the metal content. In Wiersma et al. (2009), ISM contains most of the metals from early epochs until $z \sim 1.5$ and then stars dominate. In this work, the IGM and the ISM contains comparable amount of metals at early epochs, until below $z \sim 4$ the ISM contains most metals and below $z \sim 2$ stars dominates. Therefore, although all the results agree on that stars dominates the metal budget at $z \sim 0$, different models result in rather different enrichment histories. In this work and in Wiersma et al. (2009), metals in the IGM are primarily in the WHIM, with a smaller fraction in the diffuse IGM. This remains the case for the entire cosmic history, which differs from Davé & Oppenheimer (2007). This is probably because they use hydrodynamically decoupled winds. As their superwinds originate in cold SF gas were hydrodynamically decoupled, the wind material does not interact with the dense ISM, and thus is likely to remain cool. Our feedback model ejects SN energy into the surroundings and suppresses the gas cooling and the winds are generated by thermal pressure, which makes them more likely to be hot and in the WHIM phase. Wiersma et al. (2009) obtained a similar result when the kinetic energy is injected locally and the winds interact with the ISM and shocks. While more controlled simulations are necessary to explain the difference in detail, it seems that subgrid feedback models alter metal enrichment significantly. Exactly how our adiabatic SN feedback generates winds and enriches the IGM will be discussed in Chapter 5.

Focusing back on Figure 4.13, the high resolution simulation increases the metal fraction in stars while decreasing it in the ISM and non-SF gas. Between different phases of the non-SF gas, halo gas and the diffuse IGM

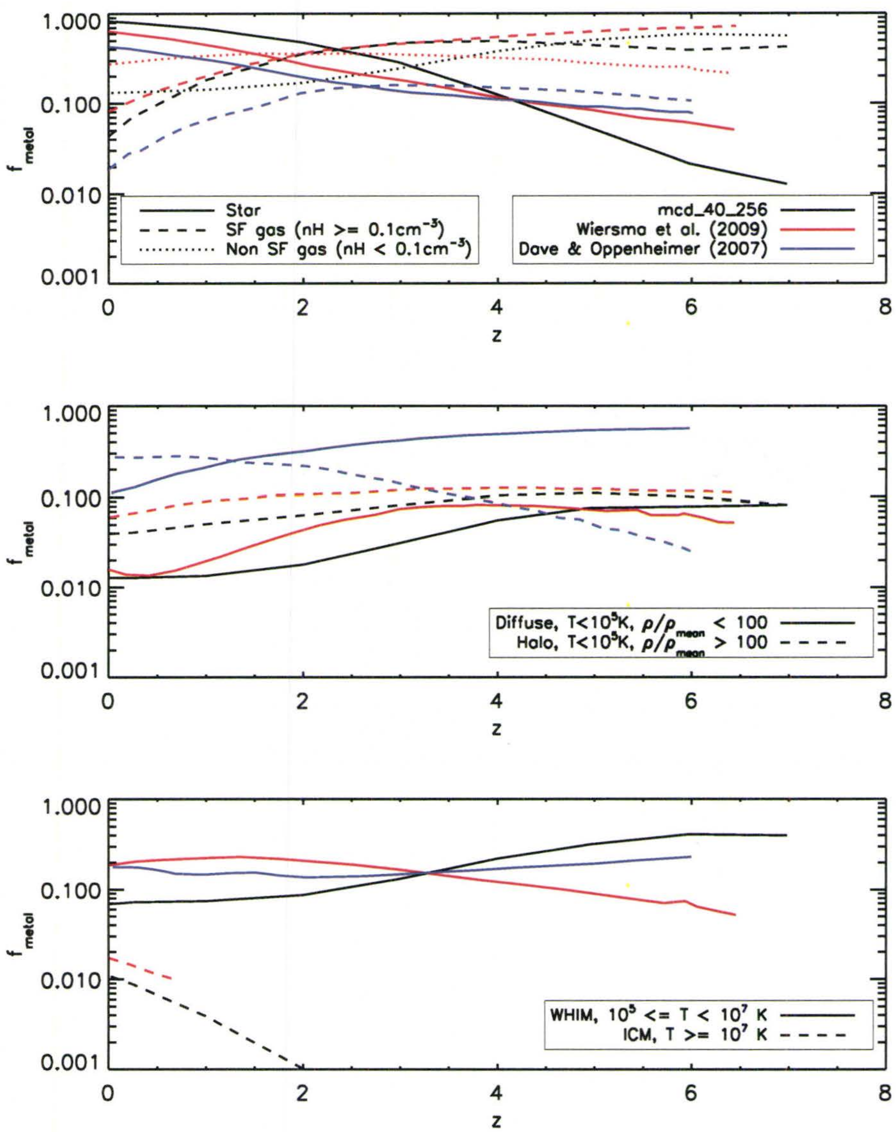

Figure 4.14 The evolution of metal fraction in various gas phases and stars in comparison with results from Wiersma et al. (2009) (red lines) and Davé & Oppenheimer (2007) (blue lines). Only the result from the reference run is plotted for simplicity. Note that Davé & Oppenheimer (2007) used a different criteria for its shock heated WHIM gas ($T > 3 \times 10^4$ K) and for halo gas. Their halo gas were identified as all gas belong to identified halos but not star-forming, thus includes hot intracluster gas.

increase their shares of metals, while metal fractions in the WHIM decrease. There are two possible causes. First of all, with high resolution SN feedback events are more frequent but each has smaller impact. As a result, particles that receive feedback energy and metals generally have shorter cooling shut-off times in the blastwave model (cf. Figure 18 in Stinson et al. (2006)). Thus they can be cooled more efficiently by metal cooling to the diffuse IGM, or to the cool halo gas. Second, with high resolution, halos of smaller mass (in particular $< 10^{11}M\odot$) are better resolved thus have more SF and feedback activities, as seen in Section 4.1.1. Because the halos are small, the winds generated do not need to have high temperature to leave the potentials of the halos. No clear convergence is seen at z = 2 when the high resolution simulation was terminated. The differences in stars, the ISM, halo gas and the WHIM are 17%, 25%, 14% and 41%, respectively. However the trend of metal fraction evolution as a function of redshift remains similar for high and low resolution runs. The general conclusions about enrichment efficiency and about metal distribution in each phase also remain the same.

4.2.2 Evolution of Metallicity

Figure 4.15 shows how the mass weighted metallicity in stars and the gas phases evolves. Stars and SF gas have the highest metallicities throughout the simulation. The metallicities are about 10^{-2} $Z_\odot$ at z = 6-7 and steadily increase to $\sim$ 0.5 solar at z=0. At z =0, the value is in agreement with the observed stellar metallicities in galaxy groups, $Z_\star \sim 0.6$ $Z_\odot$ (Finoguenov et al., 2003) and simulation results from Davé & Oppenheimer (2007). However, it is about 0.5 dex lower than the measurement from Gallazzi et al. (2008)

(diamond symbol in left upper panel of Figure 4.15), although our total stellar metal density (Ω_Z) is 4-5$\times10^{-5}$ at z = 0, consistent with the Gallazzi et al. (2008) value. Because the stellar metal density is a product of stellar density ($\Omega_\star$) and metallicity ($Z_\star$), i.e., $\Omega_Z = \Omega_\star Z_\star$, the fact that our simulations have the correct amount of total stellar metals and low stellar metallicity implies our models produce too many stars at $z \sim 0$, which is shown in the SFH (cf. Section 4.1.1). The low metallicity may be because we used a relatively low yield. In fact the metallicities in all gas phases from our simulation are generally lower than in Wiersma et al. (2009), who used a more recent, higher yield. At z = 2, the stellar metallicity is consistent, but slightly lower than the observation by Halliday et al. (2008).

Metallicities of stars and SF gas are similar throughout the simulation. The non-SF gas has an overall similar trend of evolution as the stars and SF gas, but is less enriched on average. The metallicity of the diffuse IGM evolves significantly but is much less enriched comparing to other phases. At z=0 it is only $10^{-2.5}$ $Z_\odot$. The metallicities of the WHIM and the ICM evolve slowly with a slight decreasing trend, despite their rapid mass increase at low redshift. Both values vary between 0.01 $Z_\odot$ and 0.1 $Z_\odot$. Since WHIM and the cool diffuse IGM contains similar mass at z = 0, the fact that WHIM metallicity is much higher than the diffuse gas implies our IGM enrichment process happens primarily in the WHIM. The convergence is better for metallicity than metal fractions, and the metallicities of most gas phases are nearly converged at z = 2. The largest difference is seen for the diffuse IGM and the halo gas, where the high resolution run has about 43% and 26% higher metallicites, respectively. Again, it is due to better resolving the dwarf halos and the feedback gas has a shorter cooling shut-off time so is more likely to be cooled to $< 10^5$ K.

We computed the mean metallicities of the halo gas and the ISM and compared it with the metallicity evolution of the DLAs and sub-DLAs from Prochaska et al. (2003) (triangle symbols in the bottom right panel of Figure 4.15). The DLA and sub-DLA systems trace the gas in galactic disks and halos. Our results compare well with observations. We also compare the diffuse IGM metallicity with observations from Schaye et al. (2003) using C IV lines (square symbol) and Aguirre et al. (2008) using O VI lines (cross symbol) at z $\sim$ 2.5. Our result is smaller than both observations even for the high resolution case, but the latter does bring the results closer to observations. This suggests that increasing the resolution even more may be helpful, or some additional feedback mechanisms which can enrich the diffuse IGM is probably necessary here. For the intracluster medium, observations found higher metallicities than our results at z=0, about 0.2 -0.5 $Z_{\odot}$ (Aguirre & Schaye, 2007, and references therein). This inconsistency may be because the AGN feedback is absent in the simulations. Moreover, the size of our simulation also limits the number of galaxy clusters that can form (below the cosmic average). Since our simulations were designed for studying metal enrichment in the IGM, we will not further address the intracluster medium.

4.2.3 The Effects of Metal Cooling and Metal Diffusion

4.2.3.1 The Effects of Metal Cooling

The red curves in Figure 4.12 show the evolution of mass fraction without metal cooling. At z = 0, metal cooling increases the stellar and halo mass fraction each by $\sim$ 14%, increases the SF gas fraction by 32%, and decreases the WHIM fraction by 7%. This result reflects the fact that metals enhance

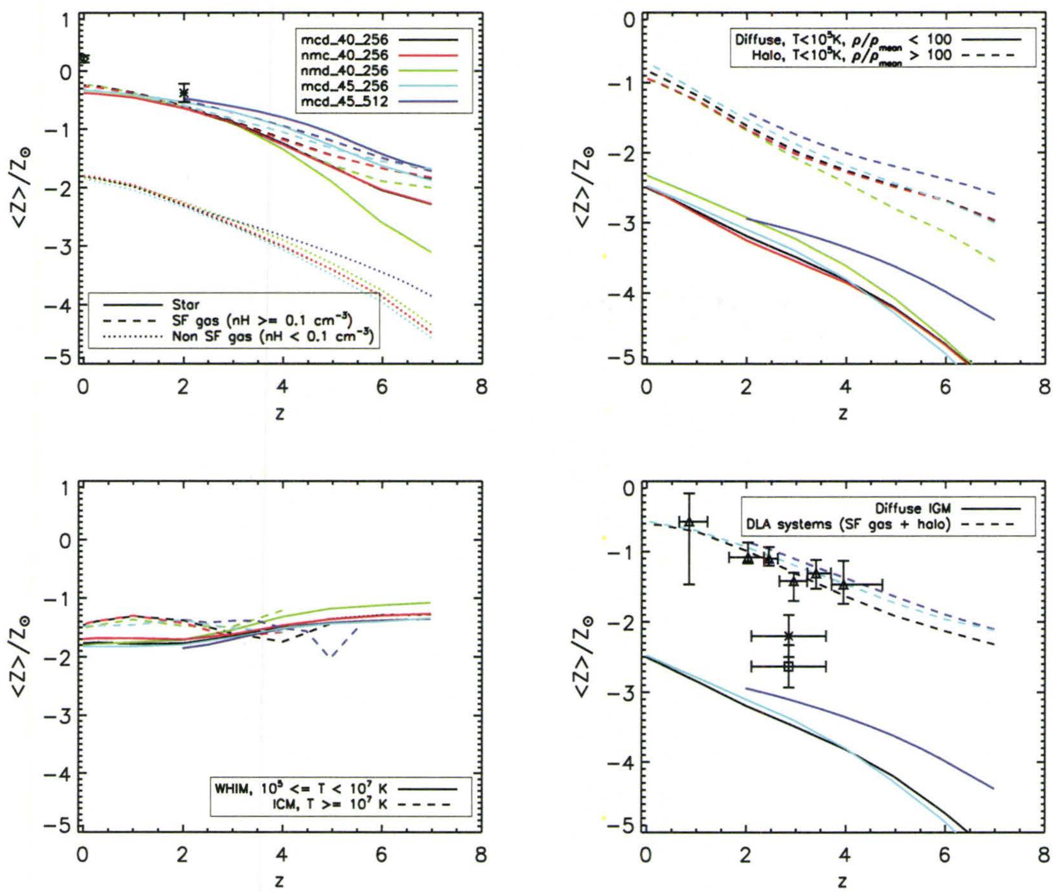

Figure 4.15 The evolution of metallicity in stars and various gas phases described in the text. The same legend as in Figure 4.12 and Figure 4.13 is used. The solar metallicity is defined as $Z_\odot = 0.0127$. Observational data: *Diamond*: stellar metallicity at z = 0 (Gallazzi et al., 2008). *Asterisk*: stellar metallicity at z = 2 from Halliday et al. (2008). *Triangles*: the metallicity evolution of DLA and sub-DLA systems from Prochaska et al. (2003). *Cross*: the IGM metallicity traced by O VI from Aguirre et al. (2008); *Square*: the IGM metallicity traced by C IV from Schaye et al. (2003). The observations were scaled to the same solar abundance as the simulations. $Z_\odot = 0.0127$

the cooling at WHIM temperatures ($10^5K - 10^7K$) and thus more WHIM cools onto galaxies and forms stars. The mass of diffuse IGM is almost unaffected by metal cooling ($\sim$ 1% decrease at z =0) as its metallicity is very low, as shown in Figure 4.15.

Similarly, Figure 4.13 shows that the metal cooling significantly decreases the metal fraction in the WHIM and increases it in the halo gas and the SF gas, because it enhances the cooling of enriched WHIM onto galactic halos and disks. At z=0, the decrease in WHIM gas is $\sim$ 24%, the increase in halo gas is $\sim$ 42%. For stars and SF gas the increments are 14% and 32%, respectively. For the WHIM and the halo gas, the effects of cooling in metal fractions (which traces the enriched gas) are larger than in mass fractions (which traces the total gas). For stars and SF gas, the effect of metal cooling is similar in both mass and metal fractions. For the diffuse IGM, metal cooling increases its metal fraction at z > 1.5, but decreases it at lower redshift. The early increase is likely due to the cooling of WHIM to become diffuse IGM, while the later decrease is probably because the diffuse IGM itself is enriched enough so that metal cooling can enhance its accretion onto halos.

4.2.3.2 The Effects of Metal Diffusion

Metal diffusion produces similar effects on mass fraction as metal cooling, as shown by the green curves in Figure 4.12. Metal diffusion contaminates large amounts of otherwise pristine gas with metals, enabling it to cool through metal lines from WHIM to SF gas or halo gas, and enhances the SFR. As it depends on the metal cooling, the effects of metal diffusion on mass fraction are smaller in magnitude than having metal cooling off (similar to the effects on the SFH). At z = 0, the increase in halo and stellar mass fractions are about 7% and 5%, respectively, and the decrease in WHIM is $\sim$ 3%.

The green curves in Figure 4.13 show the direct impact of metal diffusion on the metal content of various gas phases. Metal diffusion increases the metal content of stars, the ISM and halo gas (i.e., gas in the galaxies), and decreases the metal content of the WHIM, the ICM and the diffuse IGM (i.e., the IGM). This is counter intuitive since one expects diffusion to distribute the metals more evenly. However, as the enriched gas is ejected out of the galaxies, metal diffusion mixes its metals with the ambient gas (i.e., the ISM and the galactic halos) along the outflow trajectory so that by the time the outflow reaches the IGM (WHIM, diffuse gas or the ICM), its metal content has decreased. In other words, diffusion prevents highly enriched gas from transporting all its metals to the WHIM. This is further discussed in Section 4.3. Metal diffusion may alleviate the problem found in previous SPH simulations where the metals are too inhomogeneous (e.g., Aguirre et al., 2005). In future work, I will make a detailed analysis of the effects of metal diffusion in observable ions such as C III, C IV and O VI.

The impact of metal diffusion changes with redshift. It is more significant at high redshift for the WHIM, the halo, the ISM and the stars. For example, from z = 7 to z = 0, the increase in star metal fraction varies from 0.4% to 580%, in SF gas from 7% to $\sim$ 60%, in halo gas from 30% to 300%. The decrease in the WHIM metal fraction varies from 0.6% to 60%. Since diffusion arises from velocity shear, the diffusion effects are high near winds. The concurrent decrease in the WHIM metals and the increase in stellar, SF or halo metals imply that the winds take metals from galaxies directly to the WHIM. The fact that the diffusion impact is higher at high redshift suggests that the winds between these phases are more effective at early times.

4.3 Distribution of Gas and Metals in Density and Temperature at z=0

In this section, we examine the detailed distribution of mass and metals in the density-temperature (ρ-T) phase diagram at z=0. In Figure 4.16, the green contours indicate the mass distribution of gas across the phase diagram while the labeled darker contours indicate mean metallicities for that gas. The upper panel shows the standard run ("mcd_40_256") while the bottom panel has diffusion turned off ("nmd_40_256"). Looking at the standard run, it can be seen that gas with T $< 10^4 K$ and $\rho < 10\ \rho_{mean}$ follow a power law equation of state (EOS). It is heated by photoionization and cooled by adiabatic expansion and has generally not participated in star formation or feedback, following the standard expectation for the diffuse IGM (e.g. Hui & Gnedin, 1997). At $\rho > 10\ \rho_{mean}$, the gas distribution splits into high and low temperature branches. The low temperature branch extends to star-forming gas in galaxies. Due to metal cooling, gas with $\rho > 10^4 \rho_{mean}$ can reach temperatures below the atomic hydrogen cooling cut-off at $\sim 10^4$ K. The WHIM is apparent as the less dense gas with temperatures above 10^5 K. There is less gas around $\sim 10^{5.5}$ K compared to the peaks at 10^4K and $10^{6.5}$K due to the peak in metal cooling rates at 10^5 to 10^6 K.

The WHIM arises from both metal enriched winds and pristine virial shocks. Wind material can get out to very low densities but, with realistic diffusion operating, the typical metallicities are not that high and the cooling times can be very long. The most enriched gas is at the highest densities: star forming gas in galaxies. The metallicity of this gas can be super-solar. The highly enriched gas (near solar metallicities) is all above $\rho/\rho_{mean} \sim 10^4$.

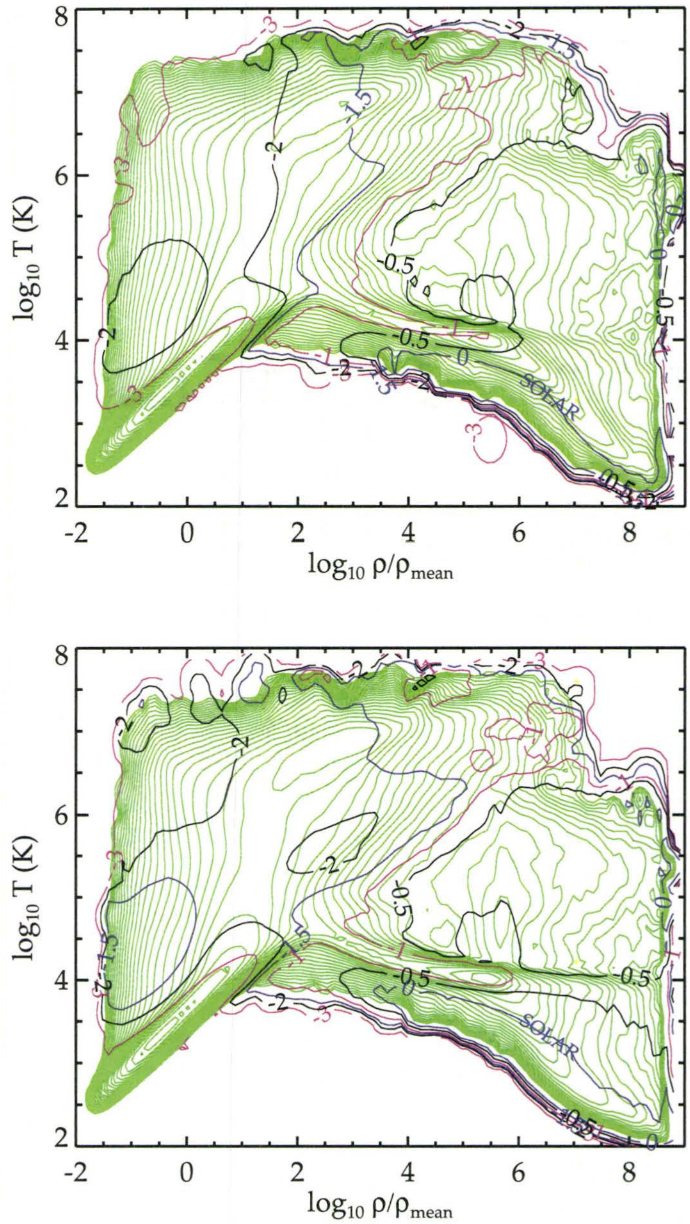

Figure 4.16 Distribution of gas and its metallicity in the ρ-T phase diagram of the reference simulation at z=0. The green contours indicate the gas mass distribution, and the black,magenta and blue contours with labels indicate the metallicities. From low to high, the metallicity labels are [Fe/H] = -3.0, -2.0, -1.5, -1.0, -0.5 and 0.0. Solar metallicity is defined as $Z_{\odot} = 0.0127$. The upper panel is the standard run with metal diffusion and the bottom panel is without diffusion.

The metallicity decreases as the wind propagates and mixes moving to lower densities. This steady progression with density can be seen in the hot gas ($T > 10^5$ K). The WHIM is enriched up to 10^{-2} Z$\odot$ to 10^{-1} Z$\odot$, while the diffuse IGM following the power-law EOS is barely enriched. The metallicity contours in Figure 4.16 show that metal enriched IGM is hotter than this diffuse phase.

The metallicity distribution on the phase diagram without metal diffusion in the bottom panel of Figure 4.16 is similar, but the metals are less evenly distributed. In particular, more low density material becomes enriched. For example, some gas around T$\sim 10^4 K$ and $\rho/\rho_{mean} \sim 0.01$ has metallicities up to 0.1 solar. On the other hand, relatively dense, cool halo gas ($\rho/\rho_{mean} > 100$, T$< 10^5$K) is less enriched, as shown in the plot by the horizontal strip of lower metallicities extends to higher densities. As discussed in Section 4.2.3, this is because, without metal diffusion, the metals are locked into the original wind material and must travel with it.

The above effect of metal diffusion is shown intuitively in Figure 4.17. The left panel shows the density distribution of a slice of the volume for the reference run at z = 0. The middle and the right panel shows the metallicity distribution of the same slice from the reference run and from the run without metal diffusion. While the left and middle panels show a clear relation between density and metallicity, the right panel shows that there are a large number of highly enriched gas particles surrounding the galaxies (because the visualization tool always plots light-colored particles on the top, the underlying distribution is partially covered). These are the particles ejected as winds from the enriched ISM, but the metals were locked in them as they leave the galaxies because there is no mixing.

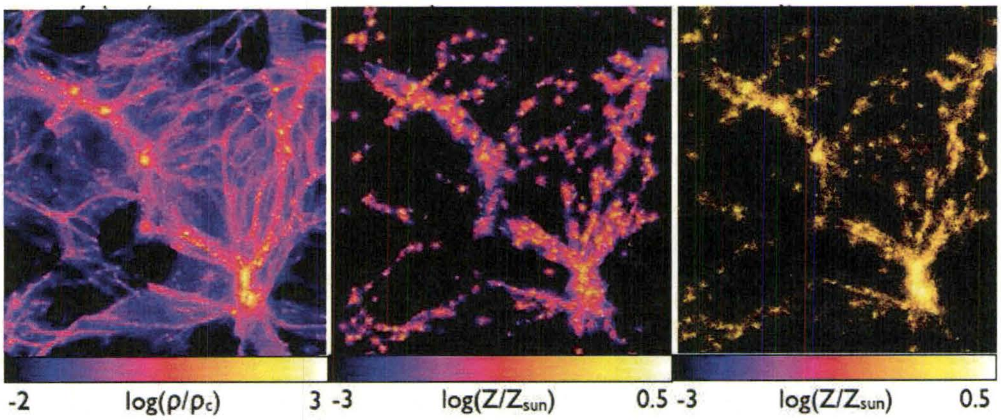

Figure 4.17 Snapshots of a slice of the simulation box (40 Mpc × 40 Mpc × 2 Mpc) at z = 0. The left and central panel are the density and metallicity distribution for the reference simulation "mcd_40_256" and the right panel is the metallicity distribution for the simulation without metal diffusion "nmd_40_256". The color bars indicate the logarithmic scale of the density in unit of cosmic mean density (for left panel) and the metallicity in unit of solar metallicity (for middle and right panel). We have adopted $Z_{\odot} = 0.0127$ for solar metallicity.

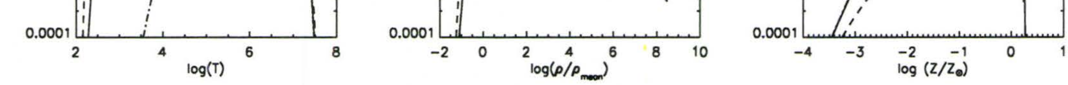

Figure 4.18 The probability density function (PDF) of the metal mass over: temperature (left panel); density(center panel); and metallicity (right panel) at z=0. *Solid lines*: the reference simulation; *Dashed lines*: the simulation without metal diffusion; *Dot-dashed lines*: the simulation without metal cooling.

Figure 4.18 shows the metal-mass-weighted probability density functions (PDF) over temperature, density and metallicity. Bimodal distributions are seen in the PDF of all three variables. As seen in the leftmost panel, metal cooling is efficient at WHIM temperatures and shifts a substantial amount of material from the WHIM to lower temperatures and the sharp peak of gas at 10^4K associated with primordial cooling is removed. Without diffusion, super-enriched gas is present which is able to cool to nearly 100 K. Without diffusion, enriched gas is also able to travel to extremely low densities as seen in the second panel.

The impact of metal diffusion is clear in the metallicity distribution (the rightmost panel in Figure 4.18). With metal diffusion, there is a large increase in material at low metallicites, $Z < 0.1\ Z_\odot$). Without diffusion the metals concentrate in a spike just above $0.1\ Z_\odot$ associated with the early distribution of metals from a star formation event. Turbulent mixing spreads the metals from the wind material to the surroundings so that substantially more gas contains metals at low levels. An increase in low metallicity gas was also achieved in Wiersma et al. (2009) using a local smoothing technique, but a physically motivated diffusion model results in the metals being substantially redistributed in space as seen in the second panel of the figure.

4.4 The Density-Metallicity $\rho - Z$ Relationship and the Effect of Metal Diffusion

Since metals are produced in stars in the densest environments in galaxies and ejected through galactic winds to the low-density IGM with finite speed, it is expected that there should be a positive relation between gas metallicity and density. Observationally, this density-metallicity relation can be inferred from certain metal tracers in QSO absorption spectra. For example, Schaye et al. (2003) used pixel statistics of the C IV line and found the carbon abundance follows a log-linear relation with density:$[C/H] = -3.47 + 0.08(z-3) + 0.65(log\delta - 0.5)$ (δ is the overdensity) at z = 1.8-4.1. It was found that comparing to the observed $\rho - Z$ relationship with the ones extracted from simulations can give non-trivial constraints on models of galactic winds (Oppenheimer & Davé, 2006; Choi & Nagamine, 2010), although large uncertainties remain because the ionization states of the metal tracers sensitively depend on how gas is distributed in the density-temperature phase space and on the uncertain shape of the ionizing UV background (Schaye et al., 2003; Oppenheimer & Davé, 2006).

Figure 4.19 shows the density-metallicity relationship from our simulation and the effect of metal diffusion. At z = 2, the reference run (solid line) produces a positive, near-linear relation between the density and metallicity in logarithmic space for $0.5 \lesssim \rho/\rho_{mean} \lesssim 3$. At the low density end the metallicity drops quickly, and at high density the metallicity curve flattens. The simulation without metal diffusion increases the under-dense gas metallicity by about a factor of 3 while it decreases it for halo gas (with overdensities $\gtrsim 100$). Overall, no diffusion results in a shallower slope. This implies that when there is no metal diffusion, more metals propagate to the low density IGM, because metals locked in gas particles were carried entirely as the gas particles were ejected into the IGM. The simulation gives a metallicity slightly higher than observations from Schaye et al. (2003), but mostly within or close to the $+1\sigma$ scatter line. This is much smaller in all density ranges than the

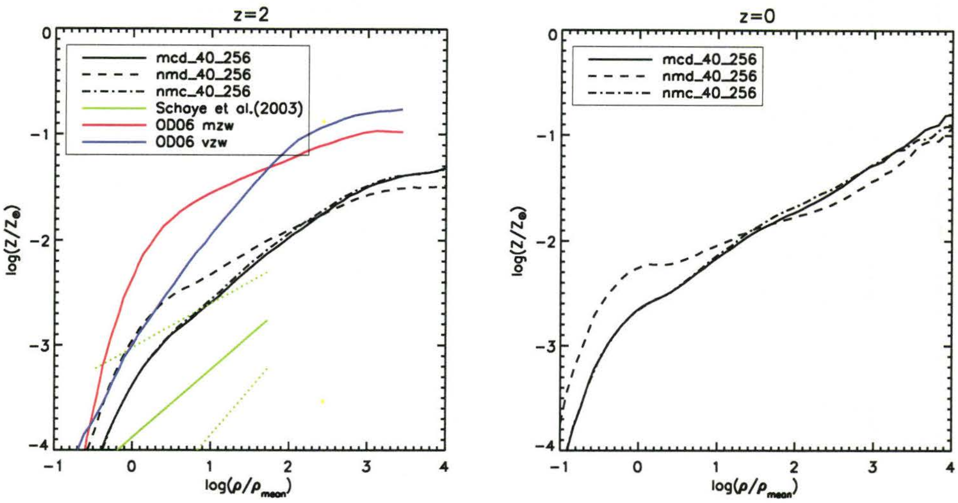

Figure 4.19 Metallicity-density relationship at z = 2 (left panel) and z = 0 (right panel) for simulations "mcd_40_256" , "nmd_40_256" and "nmc_40_256". The effect of metal diffusion is shown in the excess at the low over density range and the decrease of metallicity in the halo gas. The left panel also shows the observational result from Schaye et al. (2003) (green solid line with green dotted lines indicating 1σ scatter) and results from simulations by Oppenheimer & Davé (2006) who use explicit galactic winds. Blue line indicates their "vzw" wind model and red line indicates their "mzw" model.

metallicity from Oppenheimer & Davé (2006), indicating that their explicit wind model may enrich the IGM too efficiently. The uncertainties mentioned above (in deriving metallicity from certain metal absorbers) remain as possible causes for the discrepancy between observations and simulations. We defer detailed comparison of specific elements with observations to future work.

At z = 0, the metallicity of all gas increases mildly. The increment is most significant at low density regions, making the log-linear relation extend to lower density ($\log(\rho/\rho_{mean}) \sim 0$). It indicates that from redshift 2 to 0, metals propagate further into the low density IGM as the wind material travels. On the other hand, in the high density region ($\rho/\rho_{mean} > 1000$) the slope increases compared to z = 2, implying that metals within galaxies accumulate

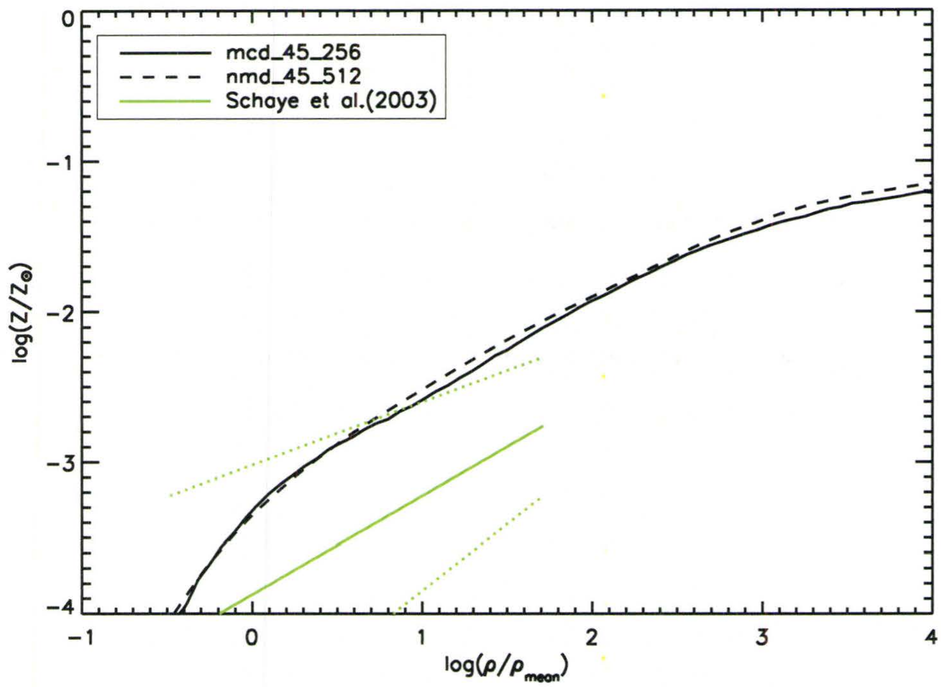

Figure 4.20 Metallicity-density relationship at z = 2 for simulations "mcd_45_256" (solid line) and "nmd_45_512" (dashed line). The observational result from Schaye et al. (2003) (green solid line with green dotted lines indicating 1σ scatter) is also shown in the same figure.

through time, and winds are not as efficient there. Metal diffusion affects the relationship at z = 0 similarly as it does at z = 2. Overall, at z = 0, the shape of the density-metallicity relation is similar to that of z = 2, and the metallicity is still slightly higher but close to observations.

Figure 4.20 shows the level of convergence in the density-metallicity relationship. At z = 2 the results from high and low resolution runs converge reasonably well. This is consistent with previous results described in Section 4.2.2, in which the metallicities of different gas phases evolve similarly for the high and low resolution runs. Because metallicity is a relative value, the more significant differences caused by resolution in absolute values (such as total gas mass and metal mass) can cancel out when metallicity is computed. The metallicity magnitude is again higher but is not far from the results by Schaye et al. (2003).

4.5 Summary

In this Chapter we described the major results from the simulations and discussed their implications. First we examined the global properties of the simulations box such as the SFH, the evolution of total neutral hydrogen $\Omega_{\rm HI}$ and the evolution of the mean flux decrement of the Lyα Forest $< D_{Ly\alpha} >$. The simulations produced a star formation history (SFH) broadly consistent with observations down to redshift z $\sim$ 0.5, and a steady cosmic total neutral hydrogen fraction ($\Omega_{\rm HI}$) that compares relatively well with observations. This demonstrates that, unlike most explicit wind models, adiabatic feedback is able to suppresses the global star formation rate (SFR) while not disrupting the gas accretion onto galaxies. At $z < 0.5$, the simulations suffer the"overcooling" problem and produce too many stars. The overproduction of stars comes from large halos ($\gtrsim 10^{12}\rm M_{\odot}$). It is likely that in these objects stellar feedback is not sufficient to suppress the cooling of gas and other forms of feedback such as the feedback from AGN are necessary. The resolution effect is most prominent in halos less massive than $10^{10}\rm M_{\odot}$, because the moderate resolution runs do not resolve these halos. In this mass range, with increasing resolution, both $\Omega_{\rm HI}$ and the SFR increase significantly which makes the results compare better with observations at $z \gtrsim 3$. For resolved halos ($> 10^{10}\rm M_{\odot}$), the evolution of $\Omega_{\rm HI}$ converges well, but the SFR is slightly too high. In brief, we conclude that with increased resolution we approach a more realistic $\Omega_{\rm HI}$, but the star formation model should be adjusted accordingly so as not overproduce stars. The evolution of $< D_{Ly\alpha} >$ in our simulations is consistent with observations to z $\sim$ 3-4, if the magnitude of the UV background is lowered with respect to the Haardt & Madau (2005) rates in CLOUDY. Resolution does not impact on the $< D_{Ly\alpha} >$ evolution since the Lyα Forest traces the diffuse, low density IGM which are fully resolved even in the lower resolution runs.

Second, we investigate the evolution of mass and metals in stars and different gas phases. As the universe evolves, there is a rapid increase in the amount of warm-hot intergalactic medium (WHIM) and a decrease in the cooler diffuse IGM. The metal content of the Universe evolves with initial metals largely residing in the IGM and later metal production in star forming gas, which is ultimately being locked in stars at the present day. These trends reflect the more effective wind escape at high redshift. IGM metals primarily reside in the WHIM, in contrast to the results of Oppenheimer & Davé (2006) and Davé & Oppenheimer (2007), who found that metals largely reside in the diffuse, cool IGM, as the wind gas starts cool with kinetic feedback and less likely to be heated up when the wind material is decoupled from the ISM. Our result is however in agreement with Wiersma et al. (2009) who also used kinetic feedback but with local energy injection and hydrodynamically non-decoupled wind models. The metallicity evolution of the gas in galaxies compares well with observations of Damped Lyman α (DLA) systems and sub-DLA systems from Prochaska et al. (2003), but the metallicity of the diffuse, cool IGM at z $\sim$ 2.5 is less than the observations by Schaye et al. (2003) and Aguirre et al. (2008), suggesting that either higher resolution or additional feedback for enriching the diffuse IGM is probably necessary. At z = 0, the stellar metallicity is less than observed (Gallazzi et al., 2008), although the total stellar metal density is consistent with the Gallazzi et al. (2008) value. This implies that the metal yield in our model is probably too small. With increased resolution, the basic trend of metal fraction evolution and enrichment efficiency in different gas phases remains unchanged. However, the high resolution run has a larger metal fraction in the cool, diffuse IGM, because it resolves the small halos better at higher redshift, and winds ejected from small halos are generally cooler.

Third, we investigated the effect of metal cooling and diffusion on the global properties of simulations and the distributions of metals in different gas phases. For metal diffusion, we further studied its effect in the density-temperature phase diagram at z =0 and the distribution of baryons as function of the galaxy mass. Metals enhance the cooling of the WHIM, allowing the gas to cool and join galactic disks. Metals also enable cooling below 10^4K. Metal cooling decreases the mass and metal fractions of the WHIM while increasing the metals in stars, halos and SF gas, and increasing the SFR by 20% and $\Omega_{\rm HI}$ by 17% at z =0. These differences are smaller than the ones found in Choi & Nagamine (2009) and Schaye et al. (2010). The former used a metal cooling rate without UV radiation and thus may overestimate the cooling rate at the IGM temperature. The latter has UV dependent metal cooling but higher overall metal yields. With realistic diffusion included, metals mix between winds and surrounding gas before they leave the galaxies, decreasing the metal content in the WHIM and diffuse IGM but increasing it in the galactic halo and star forming gas. It prevents enriched, hot winds from creating highly-enriched low density regions, and makes the density-metallicity relation smoother so it follows a nearly log-linear relation in the density range $log(\rho/\rho_{mean}) = 0 - 4$. The results imply that metal diffusion and metal cooling are essential to model the IGM enrichment and must be included in simulations.

Bibliography

Aguirre, A., Schaye, J., Hernquist, L., Kay, S., Springel, V., & Theuns, T. 2005, ApJL, 620, L13

Aguirre, A., & Schaye, J. 2007, EAS Publications Series, 24, 165

Aguirre, A., Dow-Hygelund, C., Schaye, J., & Theuns, T. 2008, ApJ, 689, 851

Bernardi, M., et al. 2003, AJ, 125, 32

Cen, R., Ostriker, J. P., Prochaska, J. X., & Wolfe, A. M. 2003, ApJ, 598, 741

Cen, R., & Ostriker, J. P. 2006, ApJ, 650, 560

Choi, J.-H., & Nagamine, K. 2009, MNRAS, 393, 1595

Choi, J.-H., & Nagamine, K. 2010, arXiv:1001.3525

Croft, R. A. C., Weinberg, D. H., Katz, N., & Hernquist, L. 1998, ApJ, 495, 44

Dalla Vecchia, C., & Schaye, J. 2008, MNRAS, 387, 1431

Davé, R., & Oppenheimer, B. D. 2007, MNRAS, 374, 427

Faucher-Giguère, C.-A., Lidz, A., Hernquist, L., & Zaldarriaga, M. 2008, ApJ, 688, 85

Finoguenov, A., Burkert, A., Boumlhringer, H. 2003, ApJ, 594, 136

Gallazzi, A., Brinchmann, J., Charlot, S., & White, S. D. M. 2008, MNRAS, 383, 1439

Halliday, C., et al. 2008, A&A, 479, 417

Hopkins, A. M. 2004, ApJ, 615, 209

Hui, L., & Gnedin, N. Y. 1997, MNRAS, 292, 27

Kirkman, D., Tytler, D., Lubin, D., & Charlton, J. 2007, MNRAS, 376, 1227

Kennicutt, R. C., Jr. 1998, ApJ, 498, 541

Lah, P., et al. 2007, MNRAS, 376, 1357

McCarthy, I. G., et al. 2010, MNRAS, 740

Murray, N., Quataert, E., & Thompson, T. A. 2005, ApJ, 618, 569

Nagamine, K., Springel, V., & Hernquist, L. 2004, MNRAS, 348, 421

Oppenheimer, B. D., & Davé, R. 2006, MNRAS, 373, 1265

Pontzen, A., et al. 2008, MNRAS, 390, 1349

Prochaska, J. X., Gawiser, E., Wolfe, A. M., Castro, S., & Djorgovski, S. G. 2003, ApJL, 595, L9

Prochaska, J. X., Herbert-Fort, S., & Wolfe, A. M. 2005, ApJ, 635, 123

Prochaska, J. X., & Wolfe, A. M. 2009, ApJ, 696, 1543

Rao, S. M., Turnshek, D. A., & Nestor, D. B. 2006, ApJ, 636, 610

Rauch, M. 1998, ARA&A, 36, 267

Rees, M. J., & Ostriker, J. P. 1977, MNRAS, 179, 541

Rybicki, G. B., & Lightman, A. P. *Radiative Processes in Astrophysics*, 1985, Jone Wiley & Sons, Inc.

Quinn, T., Katz, N., & Efstathiou, G. 1996, MNRAS, 278, L49

Schaye, J., Aguirre, A., Kim, T.-S., Theuns, T., Rauch, M., & Sargent, W. L. W. 2003, ApJ, 596, 768

Schaye, J., et al. 2010, MNRAS, 402, 1536

Springel, V., & Hernquist, L. 2003, MNRAS, 339, 312

Steidel, C. C., Erb, D. K., Shapley, A. E., Pettini, M., Reddy, N., Bogosavljević, M., Rudie, G. C., & Rakic, O. 2010, ApJ, 717, 289

Stinson, G., Seth, A., Katz, N., Wadsley, J., Governato, F., & Quinn, T. 2006, MNRAS, 373, 1074

Wiersma, R. P. C., Schaye, J., & Smith, B. D. 2009, MNRAS, 393, 99

Wiersma, R. P. C., Schaye, J., Theuns, T., Dalla Vecchia, C., & Tornatore, L. 2009, MNRAS, 399, 574

Wilkins, S. M., Trentham, N., & Hopkins, A. M. 2008, MNRAS, 385, 687

Wolfe, A. M., Gawiser, E., & Prochaska, J. X. 2005, ARA&A, 43, 861

Zwaan, M. A., Meyer, M. J., Staveley-Smith, L., & Webster, R. L. 2005, MNRAS, 359, L30

Chapter 5

Characterizing Wind Properties

The primary difference between the simulations presented in this work and earlier enrichment studies is the mechanism for galactic wind generation. Earlier simulations explicitly added velocity to gas in regions where stars form. Here feedback only added thermal energy and prevented gas cooling according to a recipe developed using simulations of isolated Milky Way-like disks and dwarf galaxies. We have shown in the previous Chapter that adiabatic feedback can regulate star formation down to $z > 0.5$ and cause substantial mass loss from galaxies to enrich the IGM. However, since winds are produced dynamically as a result of feedback instead of via a wind recipe, it is helpful to characterize the wind generation mechanisms. In this Chapter, we examine mass loss as a function of halo mass for our baseline simulations. The purpose is to understand how the adiabatic feedback generates winds that enrich the IGM. As discussed in the previous chapter, our approach allows scope for more vigorous feedback. Additional feedback models such as explicit superwinds and subgrid AGN models may be included in future enrichment studies.

5.1 Properties of Baryons within and outside of Halos with Different Masses

We identified halos using a friends-of-friends (FOF) group finder with linking length $\epsilon = \frac{1}{5}$ of the inter-particle separation ($\sim$ 30 kpc for the reference run) to find material inside regions of overdensity $\frac{\delta\rho}{\rho} \gtrsim 125$. We compared the baryon fraction (M_{bary}/M_{tot}) of material inside the halos (black solid line) as a function of total halo mass at z = 0 with the cosmic mean (Ω_b/Ω_m, dotted line) in Figure 5.1. The baryon content is low for low mass halos ($< 10^{10} M_{\odot}$). It increases quickly with mass in the intermediate range, and stays near the cosmic mean beyond $\sim 2 \times 10^{11} M_{\odot}$. Halos of mass less than $2 \times 10^{11} M_{\odot}$ contain less than the cosmic mean in baryons, indicating that gas was either prevented from accreting onto those halos, or was ejected/stripped from them. Using a lower resolution (2×128^3 particles) run (not plotted here), we ruled out that the decrease below $\sim 10^{11} M_{\odot}$ is a resolution effect. Possible mechanisms that cause the mass loss include: 1. Background UV radiation heats the gas and prevents it from accreting onto dwarf galaxies; 2. Tidal stripping during merger events; 3. Winds generated from the stellar feedback mechanism.

We investigated where the "lost" baryons are at the current epoch by pairing each gas particle with its dark matter (DM) partner at the same location in the initial conditions. We identified the gas particles that remain in the IGM (i.e. do not belong to any groups) even though their partner dark matter particle has accreted onto a halo at z=0. When plotting any properties of this gas as a function of halo mass, we are referring to the mass of halos to which the DM partner of the gas belongs. Note that this method only considers the difference between the initial condition and the snapshot at z = 0, so it does not differentiate re-accretion of gas after ejection. Hence the result here is used as a qualitative indication of the fate of the "lost" gas. A more precise description would require tracking the dynamical history of the gas particles. Furthermore, because halos evolve and generally increase their mass towards low redshift, as more gas accretes onto them or merger events take place, the halo masses plotted here (which are measured at z =0) may be higher than the mass when the winds were ejected. We will address this issue in Section 5.2. According to its temperature, this gas was categorized as WHIM (10^5K < T < 10^7K) or cooler, diffuse gas (T < 10^5K). Figure 5.2 shows the WHIM fraction (black line with error bars). For comparison, the gas inside halos was also categorized in the same way as warm-hot halo gas and cool halo gas, and the warm-hot gas fraction is shown in the same figure (red line with error bars). Despite the large error bars, the curves show that gas within or escaped from smaller halos tends to be cooler than that associated with larger halos. For gas within halos, this is expected because larger halos have larger gravitational potentials and higher virial temperatures. For gas escaped from halos as winds, it indicates that our winds do interact with the halo gas as they leave. This is probably because the winds are not hydrodynamically decoupled in our model.

We investigated the role of stellar feedback and winds in the efficient mass loss by tracing the density history of the "lost" gas up to z = 5 to identify winds. If its highest overdensity, $\rho(z)_{max}/\rho_{mean}$, was larger than 100, and its current density is less than half of the maximum ($\rho(z = 0) < 0.5\ \rho(z)_{max}$),

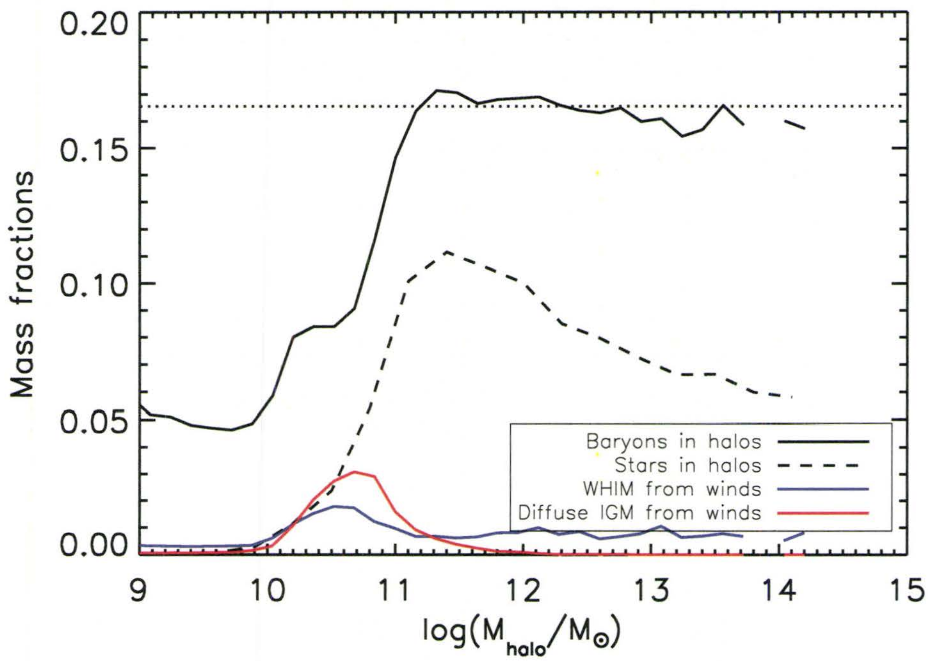

Figure 5.1 Distribution of baryon and stellar mass fractions of halos and wind fraction escaped from halos, as a function of total halo mass in the reference run (z=0). *Black solid line:* baryon fraction (includes gas and stars) in halos. *Dotted line*: the cosmic mean value. *Dashed line*: stellar mass fraction. To indicate how halos of different mass lose gas and the role of stellar feedback and winds, we identify the lost gas by pairing each gas particle with its dark matter neighbour in the initial condition, and finding the ones who have their DM partners within halos but are themselves in the IGM. When plotting this gas as a function of halo mass, we mean the mass of halos that its pairing dark matter particle belongs to. The gas found in this method is further split to the WHIM phase (10^5 K < T < 10^7K) and the cooler IGM phase (T < 10^5K). Among this gas, winds were identified by tracing the density history of the gas using $\rho(z)_{max}/\rho_{mean} > 100$ and $\rho(z=0) < 0.5\ \rho(z)_{max}$. *Blue solid line*: mass fraction of the halo baryons that escaped as wind and are currently in the WHIM. *Red solid line*: mass fraction of the halo baryons that escaped as wind and are currently in the diffuse IGM.

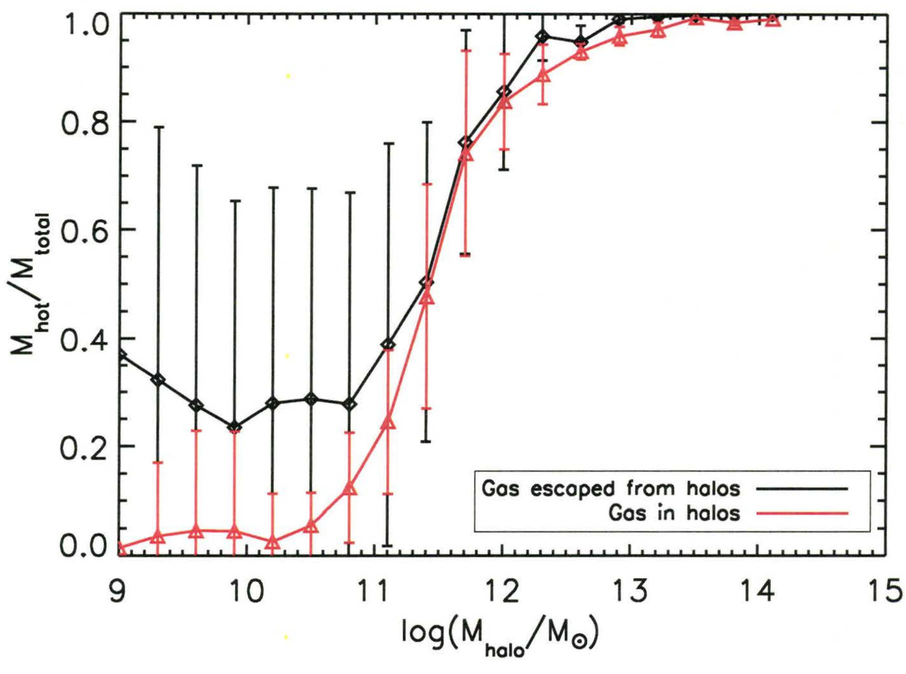

Figure 5.2 For the gas that is currently within or outside of a certain halo, the mass fraction of this gas that is in the warm-hot phase (10^5 K < T < 10^7K), as a function of the halo mass. *Black curve with error bars*: mass fraction of the gas outside of halos (identified by the partner DM particles) that is in the warm-hot phase (i.e. WHIM). *Red curve with error bars*: mass fraction of halo gas that is in the warm-hot phase.

then the gas is considered ejected as wind material. Since the gas density was measured only when snapshots were generated every $\Delta z = 0.25$, it is possible that some wind gas was omitted. However, we verified this density method in the non-diffusion simulation, where winds can be identified by the metallicities of the particles. Our density method successfully detects the same material identified by metals. The blue and red lines in Figure 5.1 indicate fractions of gas that was expelled from halos as winds, and is currently in the WHIM and cool IGM phase, respectively. We also plotted the stellar mass fractions in the same figure (dashed line).

Our results show that baryon loss due to winds is most efficient in intermediate mass ranges, 10^{10} to $10^{11}M_{\odot}$. This is also the range where the stellar fraction increases rapidly, which reflects the correlation between star formation and wind generation. Below $10^{10}M_{\odot}$, both the baryon fraction and stellar mass fraction of the halos are very low. We traced the accretion history of the "lost" baryons and found most of the gas has never accreted onto any objects. Considering the star formation rate does not converge well, especially in this mass range, higher resolution is probably necessary to further investigate these objects. However, it is likely that heating due to the background UV radiation prevents gas accreting onto such halos, since UV heating can bring gas temperatures to $10^4K - 10^5K$, comparable to the virial temperature of dwarf galaxies with mass $\lesssim 10^{10}M_{sun}$. Wind fractions start to decrease when M $> 10^{10.5}\mathrm{M}_{\odot}$. This may be caused by: 1. A decrease of wind escape efficiency with increasing halo gravitational potentials; and/or 2. A decrease of star formation efficiency as halo mass increases, as indicated in the decline of stellar fraction in Figure 5.1. The latter is probably due to the increase in cooling time, as the virial temperature of the halo increases and the cooling rate decreases beyond 10^6 K (ref. Figure 3.5). For halos with mass $\gg 10^{12}\mathrm{M}_{\odot}$, virialized gas can have a longer cooling time than the Hubble time and hence fuel supplies for SF activities can be greatly reduced (Rees & Ostriker, 1977). It is worth noting that the stellar fraction from our simulation is larger than observations (e.g., Guo et al., 2009) so there is an "overcooling" problem, in which gas in simulations tends to cool too rapidly and form more stars compared to observations. It was suggested that feedback from Active Galactic Nuclei (AGN) may alleviate this problem (e.g. McCarthy et al., 2009) especially for galaxy groups. However, an investigation of AGN feedback is beyond the scope of this work, and we use the stellar fraction curve only to indicate SF activities in different mass halos.

The colored lines in Figure 5.1 show that the wind material can be in WHIM or cooler IGM phases. Galaxies of all masses larger than $10^{10}\mathrm{M}_{\odot}$ generate winds in the form of WHIM, while only galaxies that are in the range $10^{10} - 10^{12} M_{\odot}$ have cool wind gas. We tracked the temperature history for this cool wind gas and found that about 60 % of it had $T > 10^5 K$ when it was generated and has subsequently cooled.

Figure 5.3 shows the metallicity distribution for the baryons within halos, WHIM and diffuse gas as functions of halo mass. The metallicity for all gas is low for halos with mass $\lesssim 10^{10}\mathrm{M}_{\odot}$. For the diffuse IGM and the WHIM, this is probably because this gas has never accreted onto galaxies and experienced star formation. For the gas in halos, the metallicity is still low due to low star formation. In the intermediate mass range, the metallicity of the gas in halos increases significantly, because the baryon content of halos increases and the galaxies undergo multiple star formation events and accumulate metals. Consequently, winds are enhanced, increasing the metallicities in the diffuse and WHIM gas outside those halos. The metallicity of baryons in halos saturates above $\sim 10^{11}\mathrm{M}_{\odot}$, reflecting the decline of SF activity with increasing halo mass. The metallicities of the escaped material (in both the WHIM and cooler IGM phase) decreases, possibly due to the inefficiency of winds leaving more massive objects and the decline of star formation. Note that the amount of diffuse gas is very small in massive objects beyond $10^{12}\mathrm{M}_{\odot}$ so the metallicities have large uncertainties.

The dashed lines in Figure 5.3 show the metallicities of different gas phases for the non-diffusion run. The effects of metal diffusion are seen in two aspects. First, metal diffusion contaminates the gas that is prevented from accreting due to UV or stripped by tidal forces, as indicated in the increase of the metallicity of the gas formerly associated with low mass halos when metal diffusion is on. Second, metal diffusion allows winds to lose metals along the wind trajectory, therefore significantly decreasing the metallicity in winds, while increasing it in halo gas. This is reflected in the metallicity decrease of the gas outside halos (both the WHIM and the diffuse gas) at masses larger than $10^{10}M_{\odot}$, and the increase in the metallicity of the baryons within halos. Without diffusion almost all metals in the unbound gas are locked in wind material (98% of all metals in the WHIM and 99% of all metals in the diffuse IGM). In the full model, including metal diffusion, the numbers decrease to 58% and 80%, respectively.

5.2 Wind Tracing - When and Where does the Enrichment Happen?

We described in the previous section how haloes with different masses lose their gas and the possible mechanisms for mass loss. Figures 5.1 and 5.3 indicate that winds at $z = 0$ mostly came from halos that are currently in the intermediate mass range, 10^{10} to 10^{11} $M_{\odot}$. Comparing the stellar mass fraction in these halos, we found that the wind generation in this mass range is closely related to star formation activity. However, the method does not capture the mass of the halo when the wind was ejected and the time (redshift) of such enrichment events. In this section we attempt to answer this question by tracing the wind particles back to high redshift. We will also investigate the

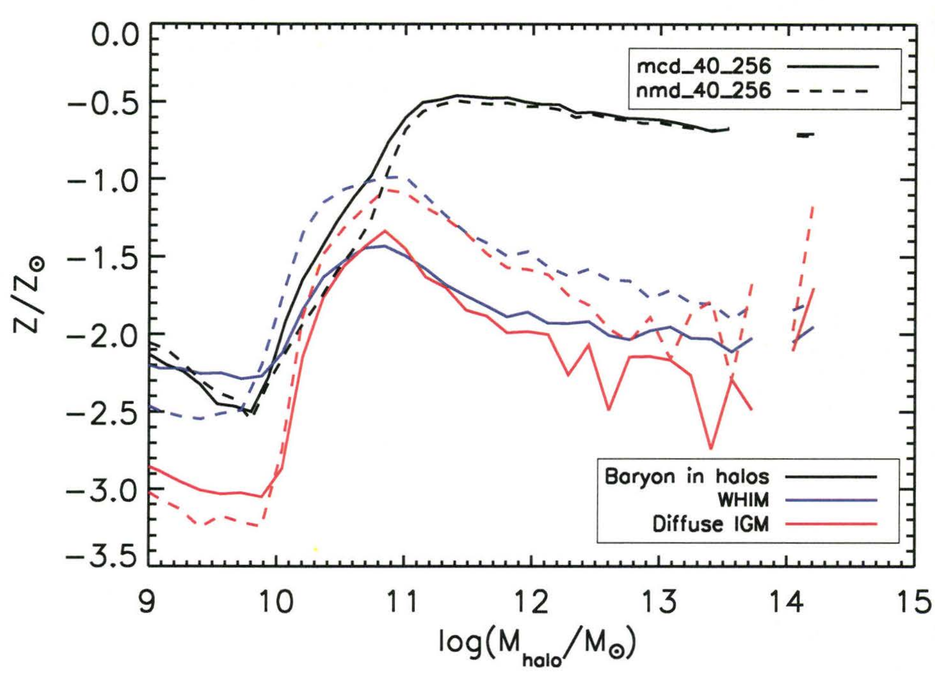

Figure 5.3 The distribution of metallicities of baryons within halos and different phases of gas escaped from halos (described in the caption of Figure 5.1) as a function of total group mass at z = 0. The solar metallicity used in this plot is $Z_{\odot} = 0.0127$.

relation between current wind properties (e.g. density and temperature) and their origin.

To find out where the current (z=0) winds come from, we identified all the gas particles that do not belong to any FOF group. These particles were then tracked back in outputs at successively higher redshift (i.e. z = 0.25, 0.5... etc.). For each particle i, if it was found in a halo at a certain redshift in the history, then the halo mass M^i_{halo} and the redshift z^i_{eject} were recorded. Because of our limited time resolution in outputs, the actual time of ejection is between z^i_{eject} and $z^i_{eject} - 0.25$. If not, then the particle is searched in the next output (with z = z+ 0.25). The process is repeated until z =

5. If the particle had never been associated with any halo from z = 0 to z =5, then the gas was ejected as wind at z > 5, or the material never accreted onto any object. We can roughly differentiate the two from the metallicity of the gas, but because metal diffusion spreads wind metals to galactic halos, the method is not exact (on the other hand, for the simulation without metal diffusion, it can identify all the enriched wind at z >5). For all gas that was within a halo but is currently in the IGM, we further use the density criterion $\rho_{z=0} < 0.5\rho_{max}$ (comoving density). If the criterion is satisfied then the gas particle is considered to be enriched wind material. Again we verify this method using the no diffusion ("nmd_40_256") run and found the above method can fully detect the enriched winds.

Now that we have obtained M^i_{Halo} and z^i_{eject}, we first investigate what type of halos generate the enriched wind at z = 0 and its dependence on redshift. For each redshift range $(z, z - \Delta z)$, the mass of metals produced in this redshift range *and still in the IGM at z=0* is computed by simply adding the metal mass of the particles that have $z^i_{eject} = z$. Similarly, using M^i_{Halo}, the metal mass in each redshift bin from halos of mass ranges $10^9 - 10^{10}$M$_\odot$, $10^{10} - 10^{11}$M$_\odot$, $10^{11} - 10^{12}$M$_\odot$ and $> 10^{12}$ M$_\odot$ is calculated. Figure 5.4 shows the amount of metals ejected from halos of different masses in each redshift bin normalized by the total amount of metals ejected from all halos since z = 5. For all halo masses, the evolution of metal mass with redshift indicates that most wind material existing today were ejected recently. At all redshifts, the metal mass is dominated by halos in the range of $10^{10} - 10^{11}$M$_\odot$ (about 50% to 70%), which is also demonstrated in Section 5.1 using a different method (the halo mass in section 5.1 is computed at z = 0, and here it is computed at the time where the wind is generated). At high redshift ($z \gtrsim 3$) small

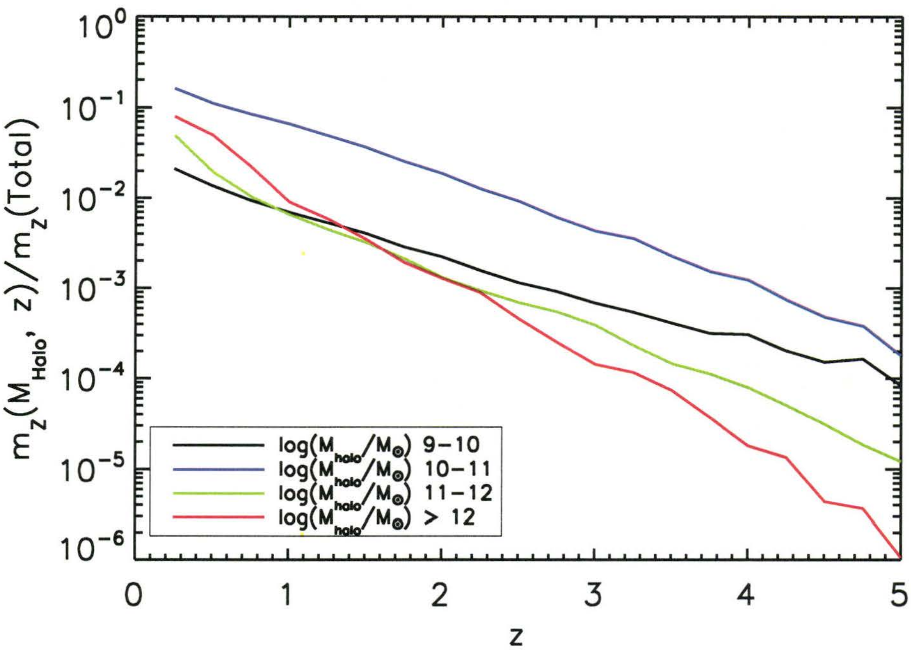

Figure 5.4 Plot showing the origin of enriched winds at z = 0. Each wind particle at z = 0 is tracked back until redshift 5. The last redshift when the particle was associated with a halo, z_{eject}, and the mass of the halo *at that redshift*, M_{Halo} are recorded (see text for details). This plot shows the mass of metals ejected from halos in each mass range at each redshift, $m_Z(M_{halo}, z)$, normalized by the total metal mass (i.e., summed over all halos and all redshifts). The curves with different colors indicate different mass range as described in the legends. The curves add up to one at each bin.

galaxy progenitors of mass $10^9 - 10^{10}\mathrm{M}_\odot$ do produce a substantial fraction of metals, as they dominate the halo population. This is not reflected in Figure 5.1 in the previous section, because: 1. the absolute amount of wind mass produced by these objects at this redshift is very small, almost negligible, compared to the amount of baryons that have not accreted onto halos; 2. the halos with $10^9 - 10^{10}\mathrm{M}_\odot$ at high redshift may grow and become $> 10^{10}\mathrm{M}_\odot$ at z =0. Towards lower redshift, the contribution from larger halos becomes important. Although with increasing halo mass the SF activity in individual

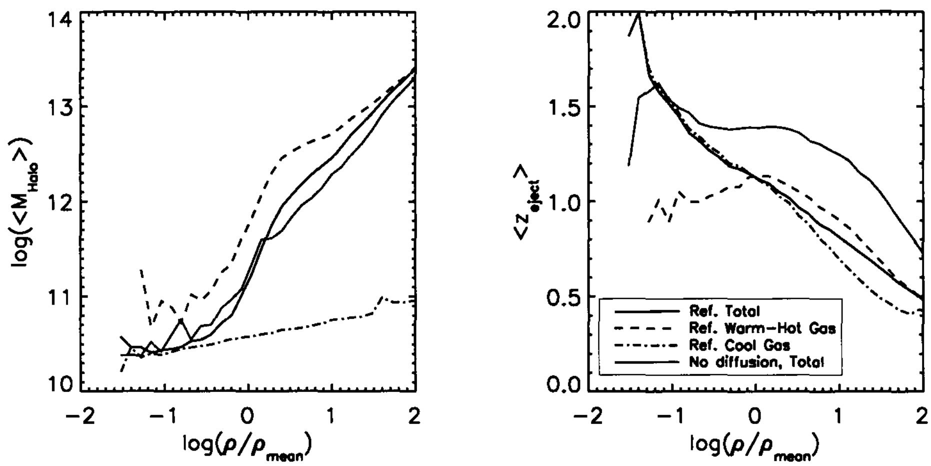

Figure 5.5 *Left panel*: the metal mass weighted mean halo mass $< M_{Halo} >$ (halos with which the wind particle is last associated) as a function of the overdensity of the wind material at z = 0. *Right panel*: the metal mass weighted ejection redshift $< z_{eject} >$ as a function of the overdensity of the winds at z = 0. The winds are also split into warm-hot ($10^5 K \leq T < 10^7$K) and cool ($T < 10^5 K$) phases according to their temperature at z = 0, and the quantities $< M_{Halo} >$ and $< z_{eject} >$ are plotted for each phase (dashed line and dot-dashed line indicate warm-hot phase and cool phase, respectively). The blue curves indicates the results from the simulation without metal diffusion.

halos may decrease (as we see in Figure 5.1), the fraction of metals contributed by stars presently in large halos still increases toward lower redshift, because the population of large objects grows with time. It is interesting to compare this figure with Figure 4.3. At low redshift, the star formation rate in halos larger than 10^{12}M$_\odot$ is much higher than in halos of mass $10^{10} - 10^{11}$M$_\odot$, but the latter produces more winds. It reflects the fact that the mass loading factor of our pressure generated wind varies with halo mass.

We now examine if there is any relationship between current properties of the wind materials, and when/where the winds originated. We bin the wind material according to its overdensity. In each density bin, we calculate the metal mass weighted mean halo mass $< M_{Halo} >$ by

$$< M_{Halo} >= \frac{\sum_i M_{Halo}^i m_i Z_i}{\sum_i m_i Z_i} \tag{5.1}$$

where m_i, Z_i and M_{Halo}^i is the mass, metallicity and the mass of halo with which the particle is last associated. The sum is over all particles in the density bin. Similarly, the metal mass weighted wind ejection redshift is

$$< z_{eject} >= \frac{\sum_i z_{eject}^i m_i Z_i}{\sum_i m_i Z_i} \tag{5.2}$$

where z_{eject}^i is the redshift when the particle i was ejected as wind. The black solid lines in Figure 5.5 show $< M_{Halo} >$ and $< z_{eject} >$ as a function of the overdensity of the wind material at z = 0. There is a clear positive correlation between density and M_{Halo}, and a negative correlation between density and $< z_{eject} >$. In other words, metals currently in the higher density IGM were ejected more recently from larger mass objects. On the other hand, metals in the low density IGM are the ones ejected in earlier epochs from low mass halos. Considering that halo masses are lower at higher redshift, and that metals are generated in densest regions in galaxies and carried by winds to low density IGM, the correlation in the figure reflect the fact that it takes certain time for wind to reach the low density IGM, that is, the enrichment does not happen instantaneously. And because the correlation is strong, we can expect that the enrichment timescale is quite long. This is consistent with Aguirre et al. (2001) who found that wind travel time affects enrichment results, and with the more recent Wiersma et al. (2010), who used simulations with kinetic feedback and explicit winds.

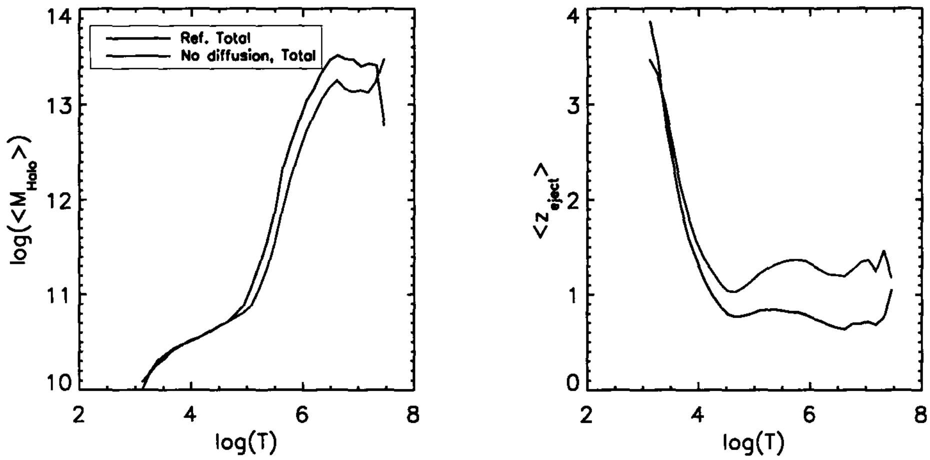

Figure 5.6 The metal mass weighted mean halo mass $< M_{Halo} >$ (left panel) and the metal mass weighted ejection redshift $< z_{eject} >$ (right panel) as a function of temperature of the winds at z = 0. The blue curves indicates results from the simulation without metal diffusion.

The enriched winds are then divided into warm-hot ($10^5 K \leq T < 10^7$K) and cool ($T < 10^5 K$) phases according to their temperature at z = 0. We repeat the calculation of $< M_{Halo} >$ and $< z_{eject} >$ above, and plot the result in the same figure. It is found that warm-hot winds generally originated from higher mass halos, although the range of $< M_{Halo} >$ is quite large, varying from $\sim 10^{11}$ to $> 10^{13}$M$_\odot$. In contrast, the origin of cool winds is mostly confined to less massive halos ($< M_{Halo} >$ between 10^{10} to 10^{11} M$_\odot$). Smaller halos have shallower gravitational potentials and lower virial temperatures and gas can easily escape from these halos without being heated to a very high temperature. This is consistent with the results shown in Figure 5.2. As to $< z_{eject} >$, because the warm-hot winds are generated in larger halos which are more populated at lower z, the average ejection redshift for warm-hot gas is lowered for the underdense gas $\rho/\rho_{mean} < 0$.

The enriched wind particles are also binned according to their temperature, and the metal mass weighted mean halo mass and metal mass weighted ejection redshift are computed in each temperature bin according to Equation 5.1 and Equation 5.2. The results are plotted in Figure 5.6. As expected, there is a strong correlation between wind temperature today (z=0) and the mass of halos that generated this wind. Wind particles that are still hot ($\gtrsim 10^5$K) at z = 0 generally originated in larger objects at lower redshift. It is interesting to note that below $\sim 10^4$K, the mean ejection redshift increases sharply with decreasing temperature, i.e. wind temperature is a strong indicator of how old the wind is. Above 10^4 K, all winds are relatively recent. This is likely related to the gas cooling rates. As shown in Figure 3.5, with metal cooling, the radiative cooling rate is higher in the range of $10^4 - 10^7$K than below 10^4 K for gas with the same density. Therefore winds that are still hot today need to be ejected relatively recently, otherwise they would have been cooled to $< 10^4$K (although it does not rule out cases in which hot winds were generated at high redshift and enter the low density IGM, where the cooling time is long). In contrast, for the winds below 10^4K the cooling time is much longer, thus the wind temperature reflects its age.

We also track the enriched winds for the simulation with no metal diffusion using the method described above. The blue curve in Figure 5.5 and Figure 5.6 shows $< M_{Halo} >$ and $< z_{eject} >$ as a function of density and temperature for the no diffusion run. It appears that metal diffusion does not significantly affect $< M_{Halo} >$ and the general trend of decreasing $< z_{eject} >$ with increasing density remains (at least for winds with overdensity above 0.1). However, with metal diffusion $< z_{eject} >$ is generally higher. This is related to how $< z_{eject} >$ is computed. Without metal diffusion, outflow particles do not lose metals when they travel into the IGM. Thus winds generated at earlier time have higher metallicity (Z_i) than in the case when metal diffusion is on, and have more weight in calculating the metal mass weighted ejection redshift (cf. Equation 5.2). The right panel of Figure 5.6 shows that without metal diffusion, the average ejection redshift for gas beyond 10^4K increases. This can also be explained by the fact that winds generated at earlier epochs does not lose their metals and therefore have more weight in $< z_{eject} >$.

In summary, in this section we tracked the history of the wind materials at z =0. It was found that: 1. halos with intermediate mass $10^{10} - 10^{11}\mathrm{M}_\odot$ dominate the wind generation at all redshift, but towards lower redshift the contributions from larger halos become important; 2. Metals in the cool, low density IGM today mostly originated from small halos at higher redshift, and metals in denser regions were generated more recently by higher mass halos. In future work, we will characterize in detail the behavior of winds generated by our feedback and the effects of metal and thermal diffusion using high resolution zoomed-in galaxy simulations.

5.3 Characterizing the Mass Loading Factor of Winds

Observations of local star burst galaxies (Veilleux et al., 2005, and references therein) have found correlations between the star formation rate ($dM_\star/dt$) and mass loss rate in winds (dM_w/dt): $dM_w/dt = \eta dM_\star/dt$, where η is the mass loading factor and its value varies from 0.01 to ~ 10. This relation is often built in to explicit wind models in which η, together with the initial wind velocity v_w, are input parameters. In most implementations of explicit wind models (e.g. Springel & Hernquist, 2003; Dalla Vecchia & Schaye, 2008; Wiersma et al., 2009) a constant η is used. Other implementation such as the momentum driven wind model used in Oppenheimer & Davé (2006) and the variable velocity wind model in Choi & Nagamine (2010), adopt values of η that are a function of the velocity dispersion of the galaxies that generate winds. In our simulations, winds are generated by the pressure force of the ISM and thus there are no free wind parameters. In this section we compute the effective mass loading factor from our simulations (as an outcome of our feedback model) at different redshifts and compare it with the mass loading factor in explicit wind models. We define the effective mass loading factor at each redshift interval $(z, z + \Delta z)$ $(\Delta z = 0.25)$ by: $\eta_{eff} = \Delta M_{outflow}/\Delta M_{\star}$. Here $\Delta M_{outflow}$ and ΔM_{star} are the mass of gas outflow ejected and the mass of stars formed in the redshift interval, respectively.

It is difficult to capture what gas is part of an outflow at a certain redshift without tracing the evolution of all particles in the simulation. Winds generated at certain time may re-accrete back onto galaxies at a later timestep. By tracking a small sample of wind particles, we found that the percentage of re-accretion winds in our simulation is substantial. Thus if we track all the existing wind particles at z=0 back in history (as in the previous section), we will miss most of wind from early epochs because they could have already re-accreted back onto galaxies. In this section, we use two different criteria to approximately identify outflows generated in each redshift interval. Although neither of the two can detect outflows precisely, the result is indicative and serves as a first step towards a detailed characterization of our wind model.

1. Group identifier: If a particle i belongs to an FOF group at redshift z

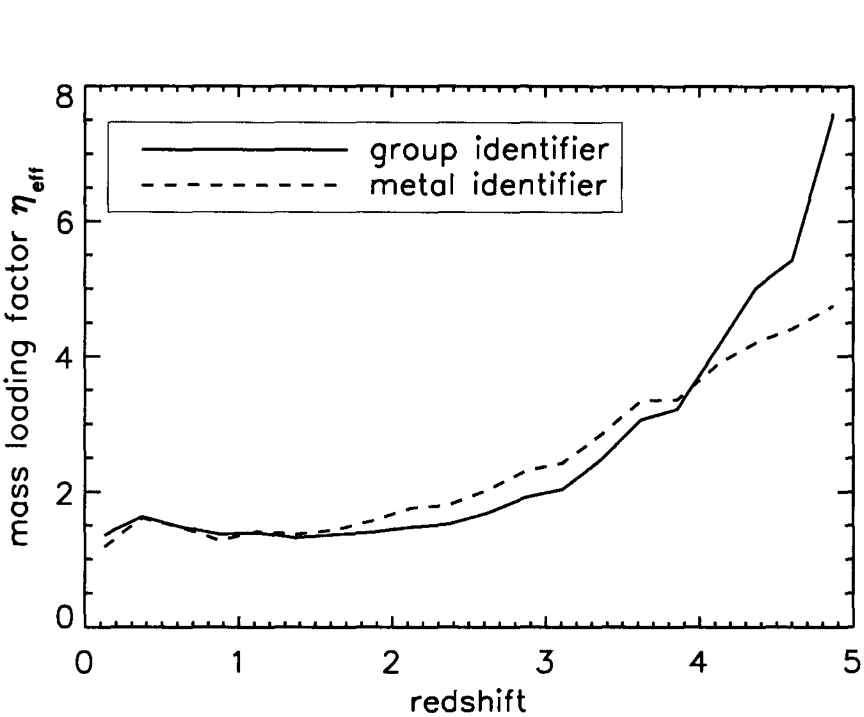

Figure 5.7 The effective mass loading factor as a function of redshift calculated from the non-diffusion simulation "nmd_40_256". The mass loading factor here is an outcome of our feedback model, not a free parameter as in explicit wind models. The solid and dashed lines indicate different ways to identify outflows, one use the group information of the gas particle (solid line), the other use the metallicity increments (dashed line). See text for detailed description.

but does not belong to any at $z - 0.25$, then it is an outflow particle.

2. Metallicity identifier: If the metallicity of particle i at $z - 0.25$ is higher than at z, and $\rho_i(z - 0.25) \leq 0.5\rho_i(z)$, then this particle is a part of an outflow.

We use the non-diffusion simulation "nmd_40_256" to avoid the complexity of using the metal identifier when metal diffusion is turned on. Both criteria are quite strict. In the group identifier, particles need to be ejected out of the halo in the time interval of Δz. Depending on the velocity of winds, the redshift and the mass of the halos, we may have omitted winds that cannot leave the group in Δz. The second, metal identifier, captures only the newly enriched winds, so any ISM gas that is entrained in the hot wind outflows is not taken into account. However, at the resolution of current cosmological-scale simulations, neither the ISM nor the entrainment is well modeled. In our feedback model, gas that receives SN energy is the same as that which receives metals, the possibility of cold, heavy gas particles being ejected along with hot flows is probably small. Note that the group identifier does allow entrainment of unenriched gas. Figure 5.7 shows that the group and metal identifier give similar η_{eff} at $z \lesssim 4$, but at higher redshift the group identifier gives a larger η_{eff}, which is probably due to entrainment of unenriched gas. The effective mass loading factor η_{eff} varies from ~ 1 to 8 as a function of redshift. These values are in a similar range as the ones used in explicit wind models, but smaller than the ones in the momentum driven winds model used in Oppenheimer & Davé (2006) (their Fig. 4). However, uncertainties still exist in whether our methods can fully capture the winds. Moreover, our wind identification methods only capture wind material that escaped from halos, whereas in explicit wind models, the mass loss rate dM_w/dt stands for all mass loss in winds when the winds were launched. Thus there is a factor of escape efficiency included in our effective mass loading factor, but not in the η in explicit wind models. And this can also cause a smaller η value from our results.

At higher redshift the mass loading is higher. Considering that at higher redshifts smaller objects dominate, this trend implies that the mass loading factor decreases with increasing halo mass. This result is consistent with the "energy driven wind" and "momentum driven wind" pictures, where

$\eta \propto 1/\sigma^2$ and $\eta \propto 1/\sigma$, respectively, with σ being the velocity dispersion of the galaxy (Aguirre & Schaye, 2007, and references therein). With the method of wind identification used here, we are unable to characterize what type of wind our simulation generates from the blast-wave supernova feedback model. The result may also depend on resolution. We will leave further characterization of η as well as the wind velocity v_w for future work, where we will track particles in highly resolved galaxy samples and comparing it with observations of local starburst galaxies. However, the results presented in this and the previous chapter show that it is possible to use a physically motivated feedback recipe - a model that is designed based on the physics of SN explosions - to generate galactic winds and metal enrichment that are generally consistent with observations and also with the results from other works who used various explicit wind models.

5.4 Summary

In this Chapter we characterized the properties of the winds in our simulations and their generation mechanisms. We first investigated which type of galaxies generate most winds. We found that winds are most efficient for halos in the intermediate mass range of $10^{10}\mathrm{M}_\odot$ to about $10^{11}\mathrm{M}_\odot$. Winds from intermediate mass halos dominate the metal ejection at all redshifts, though towards lower redshift the contribution from halos $> 10^{11}\mathrm{M}_\odot$ becomes important. Below $10^{10}\mathrm{M}_\odot$ gas is likely to be prevented from accreting and forming stars due to UV heating and remains as low-metallicity gas, although resolution could also be a possible factor. Above about 10^{11} $\mathrm{M}_\odot$, the mass fraction of wind gas in a given halo mass, m_{wind}/m_{halo}, decreases along with the stellar mass fraction.

This is probably because the wind escape efficiency decreases with increasing halo potential and because of the decline of star formation activities especially for massive halos.

We then examined the correlations between wind properties (density and temperature) at current epoch (z=0) and the origin of these winds. There is a positive correlation between the density of the wind and the average mass of the halo from which the wind was ejected, and a negative correlation between wind density and its ejection redshift. It indicates that metals in the low density IGM (far from the halos) were ejected in an earlier epoch from less massive halos, i.e. the wind speed affects the distribution of metal in the IGM.

Using a relatively simple method, we also attempted to quantify the mass-loading factor and investigate its variation with redshift. Although these results are preliminary, they are consistent with the parameters used in explicit wind models, and it seems that the mass loading factor is larger for smaller halos, as predicted by both energy-driven and momentum-driven wind ideas.

Bibliography

Aguirre, A., Hernquist, L., Schaye, J., Katz, N., Weinberg, D. H., & Gardner, J. 2001, ApJ, 561, 521

Aguirre, A., & Schaye, J. 2007, EAS Publications Series, 24, 165

Choi, J.-H., & Nagamine, K. 2010, arXiv:1001.3525

Dalla Vecchia, C., & Schaye, J. 2008, MNRAS, 387, 1431

Guo, Q., White, S., Li, C., & Boylan-Kolchin, M. 2009, arXiv:0909.4305

McCarthy, I. G., et al. 2009, arXiv:0911.2641

Oppenheimer, B. D., & Davé, R. 2006, MNRAS, 373, 1265

Rees, M. J., & Ostriker, J. P. 1977, MNRAS, 179, 541

Springel, V., & Hernquist, L. 2003, MNRAS, 339, 312

Veilleux, S., Cecil, G., & Bland-Hawthorn, J. 2005, ARA&A, 43, 769

Wiersma, R. P. C., Schaye, J., Theuns, T., Dalla Vecchia, C., & Tornatore, L. 2009, arXiv:0902.1535

Wiersma, R. P. C., Schaye, J., Dalla Vecchia, C., Booth, C. M., Theuns, T., & Aguirre, A. 2010, arXiv:1005.3921

Chapter 6

Summary and Future Work

We investigated the enrichment of the intergalactic medium with Smoothed Particle Hydrodynamics (SPH) cosmological simulations using an adiabatic stellar feedback model. In this model, galactic outflows are generated by the pressure forces in the interstellar medium (ISM) due to feedback energy. Gas cooling was turned off for the expansion time of the superbubbles (generated by co-existing supernova (SN) explosions) to allow feedback to act on resolved scales. The simulations incorporated a self-consistent metal cooling model with an ultraviolet (UV) ionizing background along with metal diffusion that models the turbulent mixing in the IGM and the ISM. Feedback from active galactic nuclei (AGN) was not included.

We used CLOUDY (Ferland et al., 1998) to compute the radiative cooling and heating under an evolving extragalactic background. It was found that photoionization due to the UV background significantly alters the metal cooling rates at all temperatures investigated, from 100 K to 10^9 K. Above 10^4 K it decreases the cooling rate and shifts the cooling peak to a higher temperature, while below 10^4 K the UV increases the metal cooling rates, mainly due to the increase in free electrons. We investigated the effect of non-equilibrium ionization on primordial species and found that it has a large impact on gas cooling when there is no UV radiation. With radiation the recombination timescale is short and the primordial gas is generally in ionization equilibrium. Although this work focused on IGM under UV radiation, we integrated the ionization equation for primordial species directly to capture any non-equilibrium at high redshift. The effect of cosmic rays on IGM cooling was also investigated and it was found that for the IGM under a UV background, the effect is small. For this reason cosmic rays are not included in our cooling model. In brief, by incorporating UV radiation into the metal cooling calculation, we have constructed a more realistic heating/cooling model that is suitable for the IGM compared to cooling models used in most prior works (e.g., Choi & Nagamine, 2009). Many uncertainties, such as stellar UV and cosmic rays still exist for modeling the ISM cooling, and subgrid models are probably necessary. An investigation of these topics is beyond the scope of the current work.

The simulations produced a star formation history (SFH) broadly consistent with observations down to redshift z $\sim$ 0.5, and a steady cosmic total neutral hydrogen fraction ($\Omega_{\rm HI}$) that compares relatively well with observations, although possible discrepancies in the observed $\Omega_{\rm HI}$ at z $\sim$ 2-3 allow for more vigorous mass-loss. This demonstrates that, unlike the superwind models, adiabatic feedback suppresses the global star formation rate (SFR) while maintaining a regular supply of H I. As expected from the hierarchical structure formation model, the halos that dominate the global SFR evolve from dwarf galaxies at high redshift ($z \sim 5-6$) to halos larger than the Milky Way at $z \sim 0$. A similar trend was also seen in the $\Omega_{\rm HI}$ evolution. The overproduction of stars at $z < 0.5$ comes from large halos, as in these objects stellar feedback is not sufficient to suppress the overcooling of gas and feedback from the AGN is probably necessary. The SFH from all halos below $10^{12}\mathrm{M}_{\odot}$ agrees with observations well to z = 0. With high resolution, the most prominent effect is seen in halos less than $10^{10}\mathrm{M}_{\odot}$, in which both Ω_{HI} and the SFR increase significantly, and makes the total SFH and Ω_{HI} at high redshifts agree better with observations. This is a resolution effect – the low resolution runs do not resolve halos less massive than $10^{10}\mathrm{M}_{\odot}$. For intermediate to high mass halos, the evolution of Ω_{HI} converges reasonably well. However, under the same star formation recipe (based on Katz et al. (1996) which is designed for relatively low resolution simulations), the high resolution run, being able to resolve density peaks better, produces a higher SFR. In general, we conclude that with increased resolution we approach a more realistic Ω_{HI}, but the star formation model should be adjusted accordingly so as not overproduce stars. In the IGM, the evolution of the mean flux decrement in the Ly-α forest in our simulations is consistent with observations to z $\sim$ 3-4, if the magnitude of the UV background is lowered with respect to the Haardt & Madau (2005) rates in CLOUDY which is still consistent with observational constraints.

As the universe evolves, there is a rapid increase in the amount of warm-hot intergalactic medium (WHIM) and a decrease in the cooler diffuse IGM. At z=0, the fraction of mass is in the WHIM ($\sim$ 40%) is consistent with previous simulations employing different methods (e.g., Cen & Ostriker, 2006; Oppenheimer & Davé, 2006). The metal content of the Universe evolves with initial metals largely residing in the IGM and later metal production in star forming gas, which is ultimately being locked in stars at the present day. These trends reflect the more effective wind escape at high redshift. IGM metals primarily reside in the WHIM, in contrast to the results of Oppenheimer & Davé (2006) and Davé & Oppenheimer (2007), who found that metals largely reside in the diffuse, cool IGM, as the wind gas starts cool with kinetic feedback and less likely to be heated up when the wind material is decoupled from the ISM. Our result is however in agreement with Wiersma et al. (2009) who also used kinetic feedback but with local energy injection and hydrodynamically non-decoupled wind models. The mean metallicities of stars, star forming gas, galactic halo gas and the cold diffuse IGM all increase with time, but those of the WHIM and the intercluster medium (ICM) remain mostly constant with a slight decreasing trend. The metallicity of the WHIM stays between 0.01 to 0.1 $Z_{\odot}$, similar to the value found by Aguirre et al. (2005), Davé & Oppenheimer (2007) as well as Wiersma et al. (2009). The metallicity of the ICM is similar to the WHIM, which is smaller than the observed value, 0.2-0.5 $Z_{\odot}$, possibly due to absent AGN feedback. The metallicity evolution of the gas in galaxies compares well with observations of Damped Lyman α (DLA) systems and sub-DLA systems from Prochaska et al. (2003), but the metallicity of the diffuse, cool IGM at z $\sim$ 2.5 is less than the observations by Schaye et al. (2003) and Aguirre et al. (2008), suggesting that additional mechanisms for enriching the diffuse IGM is probably necessary here. At z = 0, the stellar metallicity is less than observed (Gallazzi et al., 2008), although the total stellar metal density is consistent with the Gallazzi et al. (2008) value. This implies that the metal yield in our model is probably too small, which is also reflected in the result that our metallicities of all gas phases are smaller than that of Wiersma et al. (2009) who used more up-to-date yields. With increased resolution and higher overall SFR, the 512^3 simulation has a larger fraction of metals in stars. Because it resolves the small halos better at higher redshift, and because winds ejected from small halos are cooler, it has a larger metal fraction in the cool, diffuse IGM. This also causes the higher metallicity of the diffuse IGM and decreases the discrepancy between simulation and observation. However, the basic trend of metal fraction evolution and enrichment efficiency in different gas phases remains unchanged with resolution.

We investigated the effect of metal cooling and diffusion on the SFH, the evolution of $\Omega_{\rm HI}$ and the evolution of mass and metals in different phases. For metal diffusion, we further studied its effect in the density-temperature phase diagram at z =0 and the distribution of baryons as function of the galaxy mass. Metals enhance the cooling of the WHIM, allowing the gas to cool and join galactic disks. Metals also enable cooling below 10^4K. Metal cooling decreases the mass and metal fractions of the WHIM while increasing the metals in stars, halos and SF gas, and increasing the SFR by 20% and $\Omega_{\rm HI}$ by 17% at z =0. These differences are smaller than the ones found in Choi & Nagamine (2009) and Schaye et al. (2010). The former used a metal cooling rate without UV radiation and thus may overestimate the cooling rate at the IGM temperature. The latter has UV dependent metal cooling but higher overall metal yields. With realistic diffusion included, metals mix between winds and surrounding gas before they leave the galaxies, decreasing the metal content in the WHIM and diffuse IGM but increasing it in the galactic halo and star forming gas. It prevents enriched, hot winds from creating highly-enriched low density regions, and makes the density-metallicity relation smoother so it follows a nearly log-linear relation in the density range $log(\rho/\rho_{mean}) = 0 - 4$. A similar effect is also found in the density-metallicity relationship at z = 2. At z = 2, it is slightly higher than, but broadly consistent with, the observed relationship from Schaye et al. (2003). The results imply that metal diffusion and metal cooling are essential to model the IGM enrichment and must be included in simulations.

We characterized our galactic mass-loss and wind generation. For the current adiabatic feedback model, winds are most efficient for galaxies in the intermediate mass range of $10^{10}M_{\odot}$ to about $10^{11}M_{\odot}$. These winds dominate the metal ejection at all redshifts, though towards lower redshift the contribution from halos $> 10^{11}M_{\odot}$ becomes important. Below $10^{10}M_{\odot}$ gas is likely to be prevented from accreting due to UV heating and remains as low-metallicity gas (although resolution could also be a possible factor). Above about 10^{11} $M_{\odot}$, the mass fraction of wind gas in a given halo mass, m_{wind}/m_{halo}, decreases along with the stellar mass fraction. This is probably because the wind escape efficiency decreases with increasing halo potential and because of the decline of star formation activities especially for massive halos. Most winds were hot when generated, but the ones expelled from intermediate mass range galaxies, having temperatures $\sim 10^5 - 10^6$K, could cool through metal lines and become diffuse IGM rather than WHIM. For the current (z=0) existing enriched wind, there is a positive correlation between the density of the wind and the average mass of the halo from which the wind was ejected, and a negative correlation between wind density and its ejection redshift. It indicates that metals in the low density IGM (far from the halos) were ejected in an earlier epoch from less massive halos, i.e. the wind speed affects the distribution of metal in the IGM. This result is consistent with Wiersma et al. (2010) who used explicit wind models. Using a relatively simple method, we also attempted to quantify the mass-loading factor and investigate its variation with redshift. Although these results are preliminary, they are consistent with the parameters used in explicit wind models, and it seems that the mass loading factor is larger for smaller halos, as predicted by both energy-driven and momentum-driven wind ideas.

Based on the results presented here, further study of the IGM enrichment will follow two directions. First, this work used a physically motivated feedback mechanism (the blastwave model), not a phenomenological prescription, to generate galactic winds and enrich the IGM. The result shows that adiabatic feedback is able to reasonably regulate the SFH, the H I content in galaxies, and produce a enrichment history and a density-metallicity relationship that are broadly consistent with observations. It would be interesting to investigate in depth how winds are generated from galaxies of different mass, and how closely various feedback "recipes" represent the winds in nature. It would also be interesting to examine how metal cooling and turbulent mixing alter the metal distribution in gas near galaxies. We plan to study this in the future using highly resolved isolated galaxies (or galaxy groups) formed in a cosmological context. Although we can no longer obtain the statistics of metal absorption systems, the result can be compared with observations of metals on the immediate environment of galaxies. Advances in high-resolution spectrography and observing methods are making it possible to directly map the circumgalactic material (e.g., Steidel et al., 2010).

A second direction is to utilize cosmological simulations to generate metal absorption spectra at different redshifts (e.g., spectra of C IV at $z \sim$ 2-3 or O VI at $z = 0$) to explore the distribution of metal absorbers and how different factors such as gas temperature and UV radiation, affect the metal absorption lines. In particular, with the installation of the Cosmic Origins Spectrograph (COS, Shull, 2009) and its high sensitivity in the UV, our ability to probe the IGM at low redshift, and the relation between the IGM and galaxies has increased dramatically. A comparison of realistic spectra generated in simulations to the ones from next generation observations will shed new light on understanding the galaxy-IGM interactions and galaxy formation.

Bibliography

Aguirre, A., Schaye, J., Hernquist, L., Kay, S., Springel, V., & Theuns, T. 2005, ApJL, 620, L13

Aguirre, A., Dow-Hygelund, C., Schaye, J., & Theuns, T. 2008, ApJ, 689, 851

Cen, R., & Ostriker, J. P. 2006, ApJ, 650, 560

Choi, J.-H., & Nagamine, K. 2009, MNRAS, 393, 1595

Davé, R., & Oppenheimer, B. D. 2007, MNRAS, 374, 427

Ferland, G. J., Korista, K. T., Verner, D. A., Ferguson, J. W., Kingdon, J. B., & Verner, E. M. 1998, PASP, 110, 761

Gallazzi, A., Brinchmann, J., Charlot, S., & White, S. D. M. 2008, MNRAS, 383, 1439

Haardt F., Madau P. 2005, *unpublished*

Katz, N., Weinberg, D. H., & Hernquist, L. 1996, ApJS, 105, 19

Oppenheimer, B. D., & Davé, R. 2006, MNRAS, 373, 1265

Prochaska, J. X., Gawiser, E., Wolfe, A. M., Castro, S., & Djorgovski, S. G. 2003, ApJL, 595, L9

Schaye, J., Aguirre, A., Kim, T.-S., Theuns, T., Rauch, M., & Sargent, W. L. W. 2003, ApJ, 596, 768

Schaye, J., et al. 2010, MNRAS, 402, 1536

Shull, J. M. 2009, American Institute of Physics Conference Series, 1135, 301

Steidel, C. C., Erb, D. K., Shapley, A. E., Pettini, M., Reddy, N., Bogosavljević, M., Rudie, G. C., & Rakic, O. 2010, ApJ, 717, 289

Wiersma, R. P. C., Schaye, J., Theuns, T., Dalla Vecchia, C., & Tornatore, L. 2009, MNRAS, 399, 574

Wiersma, R. P. C., Schaye, J., Dalla Vecchia, C., Booth, C. M., Theuns, T., & Aguirre, A. 2010, arXiv:1005.3921